The Dissertation Committee for Martin Filipp Scales Certifies that this is the approved version of the following Dissertation:

Localization and Failure of Aluminum 6061-T6 Under Biaxial Loading

Committee:

Stelios Kyriakides, Supervisor

Desiderio Kovar

Kenneth Liechti

Mark Mear

Krishnaswamy Ravi-Chandar

Localization and Failure of Aluminum 6061-T6 Under Biaxial Loading

by

Martin Filipp Scales

Dissertation

Presented to the Faculty of the Graduate School of

The University of Texas at Austin

in Partial Fulfillment

of the Requirements

for the Degree of

Doctor of Philosophy

The University of Texas at Austin

May 2019

Acknowledgements

I must first express my thanks to my advisor, Dr. K, for supporting me throughout graduate school. His academic, professional, and personal guidance has shaped who I am today, and being a part of his research group has been a privilege.

My research and education was made possible thanks to the financial support of the Ford Motor Company, Sandia National Laboratories, the National Science Foundation GOALI grant CMMI-1663269, the Thrust 2000 – Richard W. Moncrief Endowed Graduate Fellowship in Engineering, and the Max L. Williams Endowed Graduate Fellowship in Mechanics of Solids, Structures, and Materials.

Thank you to the members of my dissertation committee for taking the time to review my research and offer your perspective. Every professor from whom I've taken a course has shaped me in some way, and I am grateful for their devotion to teaching. Special thanks to Dr. Kallivokas and Dr. Manuel in the CAEE Department for encouraging me to go to graduate school, and to Dr. Mear who was my EM 319 instructor back in Fall 2006. I probably wouldn't have come to EM for graduate school but for my great experience in that class.

My fellow graduate students and research colleagues over the years have helped me in many ways, and I am grateful for the friendships we've developed. Thanks to Amin Anvari, Stavros Gaitanaros, Andrew Gross, Ben Harrison, Dongjie Jiang, Karlos Kazinakis, John Mersche, Zack Wilson, and Chenglin Yang. Special thanks to Liang-Hai Lee, Nicolas Tardif, and Lin Yuan, who were all instrumental in getting me going in the lab; Nate Bechle for numerous DIC discussions and for introducing me to python; and Kelin Chen,

with whom I've had the pleasure of closely collaborating, and has amazed me countless times with his curiosity and ingenuity.

The ASE/EM Department staff has been fundamental to my research achievements. Special thanks to Pablo Cortez, Scott Messec, Joe Pokluda, and Steve Sanders. This wouldn't have been possible without their technical support, and this wouldn't have been as fun without their friendship.

Last, but most importantly, I want to acknowledge all the people in my personal life who helped get through the front door and across the finish line. In particular: Ms. Bartu at WRNNMC for her kindness and guidance; George Dunham, Craig Miller, and Gordon Keith at KTCK; and my friends from Flower Mound and college who pushed me academically. I've got the best family on Earth, and I never would have gotten here without their support and encouragement: Mom, Del, Uncle Paul, Carolyn, Zac, Marianne, Bud, Greg, and everyone else. And to my wife Lindsey: thanks for taking a chance on a grad student and moving down to Austin so that we could start our life together while I continued to work on this thing. Having you in my corner through the many challenges has meant the world to me, and your strength is inspiring.

Abstract

Localization and Failure of Aluminum 6061-T6 Under Biaxial Loading

Martin Filipp Scales, Ph.D.

The University of Texas at Austin, 2018

Supervisor: Stelios Kyriakides

The adoption of new materials for light-weighting purposes in the automotive industry has been hindered by these materials' limited ductility and more-complicated constitutive models. Establishing the onset of failure through experiment is challenging, and numerical predictions depend strongly on the adopted material model. With this in mind, a series of experiments was developed with the goal of providing directly-measurable strains and stresses at failure. Custom-designed Al 6061-T6 tubular specimens with a thin-walled test section are loaded in radial stress paths in the nominal axial-shear stress space. Stereo digital image correlation is used to monitor the specimen surface throughout the experiment. The stress and deformation within the test section are uniform until a load maximum is reached, beyond which deformation localizes into a circumferential band with width the order of the wall thickness. The series of experiments shows that the strain at failure monotonically increases as the triaxiality decreases, a result that is contrary to previously-reported results for this alloy. The strains at failure are also significantly larger than previously-reported values, with equivalent strains around 1.5 at low triaxialities. This experimental methodology provides a robust means of directly establishing failure strains that can be employed as failure criteria in numerical simulations.

In support of a separate effort to numerically reproduce the responses and localization in these tension-torsion experiments, a series of combined tension and internal pressure experiments on the same tube stock was conducted. In these experiments, the tubes are loaded in radial paths in the nominal axial-hoop stress space. The data obtained proved sufficient for calibrating the non-quadratic, 18-parameter, anisotropic constitutive model of Barlat and coworkers. With the calibrated constitutive model, a large-deformation material stress-strain curve was inversely extracted from the post-necking response in a uniaxial tension test. The pressure-tension experiments were then studied numerically through a finite element (FE) model that incorporated the calibrated constitutive model and hardening response. The analysis shows that properly-calibrated plasticity with an accurate stress-strain curve and suitable FE mesh is capable of reproducing the measured responses as well as the localized deformations that developed prior to burst.

Table of Contents

Chapter 1: Introduction

1.1: MOTIVATION

Ductile failure in metals and the localized deformations that typically develop prior to failure have played an important role in industrial applications throughout history. Manufacturing processes that involve forming, stamping, and in general large deformations have been hampered in part by our limited ability to accurately predict the onset of instability and failure. The problem has become especially acute in recent years. With aggressive government fuel economy standards set forth in US Environmental Protection Agency [2012], the automotive industry is striving to reduce vehicle weight and improve fuel economy by, among other methods, replacing traditionally steel components with lighter-weight alternatives. These alternative materials include composites, high-strength steels, and perhaps most prominently, aluminum alloys. Some manufacturers have reported weight savings as great as 40% (Saito et al. [2001]) by replacing traditionally steel components with aluminum.

The use of aluminum alloys in place of traditional steels is challenged by several factors:

- Aluminum is less stiff than steel, with a modulus of elasticity one-third that of steel.
- It follows a different, perhaps more complicated, plastic constitutive law.
- Most aluminum alloys are less ductile than traditional steel.

Figure 1.1 demonstrates how some of these challenges associated with aluminum alloys arise during axial crushing. Axial crushing of open-section members is an efficient means of energy absorption and is one technique incorporated into vehicle designs to protect passengers during impact. The thin-walled Al 6061-T6 tubular specimen was crushed quasi-statically. Initially it develops axisymmetric folds, but rather quickly switches to a

non-axisymmetric mode and develops local failures. In practice such ruptures inhibit further energy absorption and can cause total failure of components. Premature failure also complicates the prediction and analysis of this crushing process. To safely and efficiently incorporate aluminum into vehicles and other applications, a clear understanding of its constitutive behavior and failure characteristics is required, and the old trial and error processes through which manufacturing techniques were developed over time are no longer acceptable.

1.2: BACKGROUND

Failure in ductile metals is brought about by the growth and coalescence of voids. As the strain increases with deformation, voids form when the crystalline matrix debonds from second-phase particles. Voids may also preexist within the material, and can form along grain boundaries and other defects in the crystal. Voids grow as the deformation continues, eventually coalescing and leading to macroscopic failure. Failure due to void coalescence gives rise to the typical ductile failure surface, which features a landscape of ruptured voids.

This mechanism has been understood since at least the late 1940s from the experimental work of, for example, Tipper [1949], and Puttick [1959]. McClintock [1968] and shortly thereafter Rice and Tracey [1969] were the first to develop analytical models for cylindrical and spherical void growth within a continuum, and established the strong relationship between void growth and the hydrostatic stress. This porous plasticity approach was solidified in the seminal work of Gurson [1977], which developed a macroscopic plasticity model based on microscopic evolution of voids. Further work from Chu and Needleman [1980] and Tvergaard and Needleman [1984] considered void nucleation and coalescence (see also the review article of Tvergaard [1990]).

Experimentally, the notion that equivalent strain to failure decreases monotonically with increasing triaxiality has been well documented by, for example, Hancock and McKenzie [1976]), and perhaps most notably Johnson and Cook [1985]. Johnson and Cook published with this work their famous failure criterion, which has since been widely adopted and remains in use today. A challenge faced by experimentalists of that era was that numerical tools did not exist to study the evolution of stress and strain inside the localized deformations that develop in ductile materials. Non-uniform fields were often dealt with through empirical corrections (e.g., Bridgman [1944]). Numerical tools for studying such phenomena exist today, however, and together with improved experimental diagnostic techniques, have enabled new developments in the field in recent years.

One of the most cited recent works is that of Bao and Wierzbicki [2004], who performed a variety of tests on Al 2024-T351 stock designed to cover a wider range of triaxiality. They extracted the stress and strain fields at failure from finite element (FE) simulations whose nominal load-displacement responses matched those of the experiments. They reported a non-monotonic relationship between the failure strains and triaxiality, suggesting that J_3, the third-invariant of the stress deviator, also contributes to ductility. The same group, in Beese et al. [2010] reported similar results in Al 6061-T6 sheet through a variety of experimental methods combined with analysis.

These findings led to a surge in interest in the subject of ductile failure. A number of failure models that incorporate J_3 in addition to the triaxiality have been proposed recently (e.g., the micromechanical models of Barsoum and Faleskog [2007a], Nahshon and Hutchinson [2008], and the phenomenological models of Bai and Wierzbikci [2010] and Mohr and Marcadet [2015]). Experimentally, a great variety of methodologies have been proposed, such as those of Driemeier et al. [2008], Mohr and Henn [2007], Gao et al. [2010], Dunand and Mohr [2010, 2011], Ghahremaninezhad and Ravi-Chandar

[2012, 2013], Brünig et al. [2015, 2016], which all depend on numerical analysis to some degree.

Hybrid experimental/numerical, and in general all numerical studies of ductile failure are extremely challenging. Any simulation that involves localized deformations requires an accurate material stress-strain curve to large strains (e.g., Tardif et al. [2012], Ha et al. [2108]), as the onset of instabilities is highly sensitive to the tangent modulus. Unfortunately, the commonly-used extrapolations of the Voce [1948] and Swift [1952] fits are not always appropriate (Chen et al. [2018a]). In addition, plastic anisotropy introduced during the fabrication of materials (such as rolling and extrusion) must be incorporated into the constitutive model to accurately model the evolution of localization (Dunand and Mohr [2010], Tardif et al. [2012], Ghahremaninezhad and Ravi-Chandar [2012]). This problem becomes especially challenging for aluminum alloys, since their yield surface and anisotropy is not well-represented by the traditional quadratic yield functions of von Mises and Hill-1948 (Hill [1990], Karafillis and Boyce [1993], Barlat et al. [2005]).

With these significant challenges faced by numerical studies of ductile failure, experimentalists therefore have sought methods to minimize the need for FE analysis with novel specimen designs (Barsoum and Faleskog [2007b, 2013] Graham et al. [2012], Papasidero et al. [2014, 2015]). Yet these efforts do not employ a specimen with a test section in which the stress and strain are known to be uniform. In addition, the absence of such a test section can significantly constrain the development of localized deformations. Finally, in these constrained test sections without clear localization zones, it is challenging to determine the location where failure initiates.

1.3: OUTLINE

In light of the above considerations, dependable experimental data remains challenging to obtain, and in its absence, the development of failure criteria is further hindered. This dissertation presents the results of an effort to develop robust experimental programs that can provide reliable data on material failure. Particular emphasis is given to the development and evolution of localized deformations under low to medium triaxialities. In Chapter 2, an experimental setup for combined tension and torsion loading of thin-walled tubes is presented, with details on the analysis of the measurements. Chapter 3 presents the results of a first series of experiments on Al 6061-T6 tubes, and compares the results to several other known results for the same alloy. Chapter 4 summarizes the results of a second series of tension-torsion experiments that was conducted in support of a larger effort. Two well-known failure criteria are calibrated to the measurements and evaluated, and experiments involving non-proportional loading are presented in this chapter as well. In Chapter 5, a full series of combined tension and internal pressure experiments is presented. The measurements are used to establish the material anisotropy and extract the large-strain hardening response. The evolution of localization is further studied through numerical analysis. The main conclusions from the work are presented in Chapter 6, and some remarks are made regarding existing problems and future areas of study.

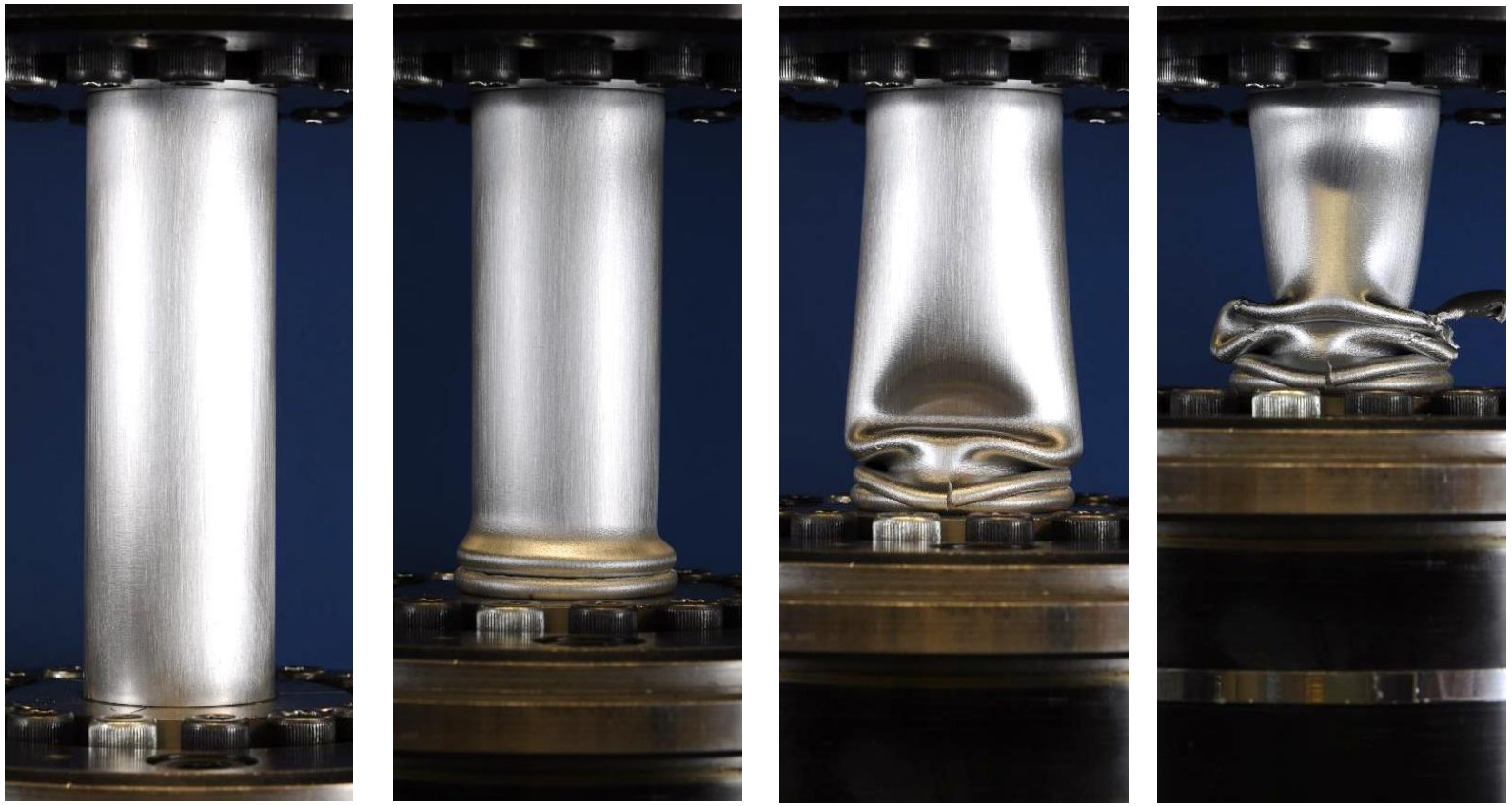

(a) (b) (c) (d)

Fig. 1.1: Quasi-static crushing of a thin-walled Al 6061-T6 tube. (a) Uniform compression. (b) Axisymmetric folding. (c) Non-axisymmetric folding and first failure. (d) Heavily deformed and featuring multiple failures.

Chapter 2: Experimental Setup for Combined Tension and Torsion of Al 6061-T6 Tubes

2.1: INTRODUCTION

As described in Chapter 1, the commonly used Johnson-Cook [1985] failure criterion is based on the long-held notion that failure is governed by stress triaxiality. Wierzbicki and coworkers were the first to point out that failure may also be influenced by the third invariant of the deviatoric stress tensor, J_3, finding in Bao and Wierzbicki [2004] and Beese et al. [2010] that the failure strain develops a local maximum near uniaxial tension (triaxiality 0.33) and local minimum near pure shear (triaxiality 0). In considering this rather unorthodox result, it is important to point out that the failure strains reported were extracted from global experimental responses using numerical analysis and assumed constitutive models.

More careful recent experiments have reported a nearly monotonic decrease of failure strain with triaxiality at lower values, thus challenging some of the claims in the work of Wierzbicki et al. (Faleskog and Barsoum [2013], Papasidero et al. [2015], Ha et al. [2018]). Ghahremaninezhad and Ravi-Chandar [2013] and Gross and Ravi-Chandar [2016]) have estimated failure strains in Al 6061-T6 that are significantly greater than those reported for the same alloy in Beese et al. [2010]. The seemingly conflicting messages that come from experiments is mainly caused by practical limitations of testing materials, especially in sheet form, under combined shear and axial loads. The problem is further confused when attempting to extract stresses and strains from finite element analysis of these large deformation experiments.

In an attempt to add some clarity to the problem, Haltom et al. [2013] (subsequently cited as HKR13) reported results from tension-torsion (TT) experiments on Al 6061-T6

tubes in which the state of stress and strain were obtained directly from the experiments. This was achieved by using a tubular specimen with a test section that is long and thin enough to permit a uniform plane stress state to develop to large deformations, and also allows the ensuing localization that precedes rupture to develop freely. These features distinguish this setup from other tension-torsion experiments such as those of Barsoum and Faleskog [2007b], Faleskog and Barsoum [2013], Papasidero et al. [2014, 2015]. In these works the test section is more constrained and develops a three-dimensional stress state. Gao [2010] and later Graham et al [2012] presented a thin-walled tension-torsion specimen that was designed to have uniform stress and strain through the wall thickness, but the relatively short test section likely constrained the development of localization.

HKR13 reported failure strains across triaxiality ranging from 0.03 to 0.45 which monotonically decreased with triaxiality, and had significantly larger values than previously reported for this material. Strains in that work were established by tracking the deformation of a grid that was electrochemically etched onto the specimen surface. Because the grid was monitored with a standard optical camera, out-of-plane deformations could not be measured, and accordingly the test program was limited to shear-dominant stress states where radial displacements are limited. Furthermore, the resolution of this measurement scheme was limited to the grid square size of ~1.5x the wall thickness.

The test setup presented in this chapter was designed to overcome the limitations of the HKR13 setup, namely by replacing the fine grid scheme used to monitor the deformation by 3D digital image correlation (DIC). DIC enables monitoring the evolution of deformation inside the narrow localization zone, and is capable of measuring 3D deformations. The hardware, specimen design, and test setup are presented here in detail.

The extraction of strains from within the localizing zones is also described, along with some details regarding the challenges of working with DIC in this particular application.

2.2: EXPERIMENTAL SETUP AND PROCEDURE

The test specimens used in the present experiments originate from commercially-available, seamless extruded Al 6061-T6 tubes with a 2 inch nominal outer diameter (OD). The test specimens are 9 inches long (229 mm) with a 0.62 inch (15.8 mm) test section machined at mid-length. The test section has a 0.40-inch long (10.2 mm) uniform section that is 0.038 inches thick (0.965 mm) and ends in 0.125 inch radii (3.2 mm). This geometry was designed to maintain nearly uniform plane stress in the test section and avoid torsional buckling. The OD of the tube outside the test section was machined to 1.9685 inches (50.0 mm), with the close tolerance of +0/-0.0015 inches. Such careful dimensions were required to ensure the specimens did not slip out of the gripping fixtures. The inner diameter (ID) was not machined, and even though carefully-aligned plugs were inserted into the tube ID when machining the OD, the specimens exhibit a small amount of eccentricity. A detailed specimen drawing will be presented in Chapters 2 and 3.

The test facility and hardware are illustrated in Fig. 2.1. Tests were conducted in a servo-hydraulic axial/torsional biaxial testing machine with capacities of 50 kip/ 22 in-kip (220 kN/2.5 kN-m). Carefully-machined plugs are inserted into the end-sections of the tube. The specimen is secured to the test system by ETP-TECHNO grips, which have an internal cavity filled with hydraulic fluid. By actuating a small external screw, the fluid is pressurized, which secures the grip to the housing and the tube to the grip. The great advantage of this gripping system is that it ensures excellent alignment and results in a very stiff test setup.

The majority of the experiments reported involve radial loadings in the nominal shear-axial stress ($\mathcal{T}$ - Σ) space so that

$$\Sigma = \alpha \mathcal{T} \quad \alpha = \text{constant} > 0. \tag{2.1}$$

This is achieved as follows: For shear dominant loadings, torsion is run under rotation control and axial load under load control. The two loads are coupled by using the torque as the command signal for the axial load resulting in a force appropriately proportional to the torque. For tension dominant loadings ($\alpha \geq 3.5$) the roles are reversed. Tension is run under displacement control and torque under load control with the axial force as the command signal, producing again the required stress ratio.

2.3: STRESSES

For the purposes of establishing the stress state, plane-stress conditions are assumed to exist in the thin-walled test section. Therefore the nominal axial and shear stress are calculated directly from the applied force (F) and torque (T) as follows:

$$\Sigma = \frac{F}{2\pi R_o t_o} \quad \text{and} \quad \mathcal{T} = \frac{T}{2\pi R_o^2 t_o} \tag{2.2}$$

where R_o and t_o are the initial mean radius and wall thickness of the test specimen. The Cauchy stresses (σ_{ij}) are then calculated via:

$$\sigma_{xx} = \Sigma / \lambda_3 \quad \text{and} \quad \tau_{\theta x} = \mathcal{T} / \lambda_3 \tag{2.3}$$

where $\lambda_3 = t/t_o$ (t is the current wall thickness) is calculated from the measured strains by invoking incompressibility (see below). We also assume for the purposes of establishing the full stress state that the specimen geometry sufficiently constrains radial contraction so that plane strain conditions prevail circumferentially. Therefore, the nominal and true hoop stresses are assumed to be proportional to the axial stresses:

$$\Sigma_\theta = \beta\Sigma, \quad \sigma_{\theta\theta} = \beta\sigma_{xx} \tag{2.4}$$

With the true stress state thus established, the principal stresses $\sigma_{1,2}$ are given by:

$$\sigma_{1,2} = \frac{\sigma(1+\beta)}{2} \pm \sqrt{\sigma^2\left(\frac{1-\beta}{2}\right)^2 + \tau^2}\ , \tag{2.5}$$

and the mean stress by:

$$\sigma_m = \sigma(1+\beta)/3\,. \tag{2.6}$$

For non-quadratic incompressible plasticity the yield function and equivalent stress are given by Hosford [1972]:

$$\Phi = (\sigma_1 - \sigma_2)^k + \sigma_1^k + \sigma_2^k = 2\sigma_e{}^k\,. \tag{2.7}$$

The proportionality factor β is then calculated from the flow rule together with the zero hoop-strain condition:

$$d\varepsilon_{\theta\theta} = \frac{\partial\Phi}{\partial\sigma_{\theta\theta}} = 0\,. \tag{2.8}$$

When k = 2, Eq. 2.7 gives the von Mises equivalent stress. In this case, β = 0.5, and the remaining pertinent stress measures are as follows:

- Mean stress: $\sigma_m = \sigma_{kk}/3 = \sigma/2$ (2.9)

- Equivalent stress: $\sigma_e = \sqrt{\frac{3}{2}s_{ij}s_{ij}} = \sqrt{\frac{3}{4}(\sigma^2 + 4\tau^2)}$ (2.10)

The third invariant of the deviatoric stress is:

$$J_3 = s_1 s_2 s_3 = (\sigma_1 - \sigma_m)(\sigma_2 - \sigma_m)(\sigma_3 - \sigma_m) \tag{2.11}$$

And some commonly-used J_3-type parameters include:

- Haigh-Westergaard variable θ: $\cos 3\theta = \left(\frac{27}{2}\frac{J_3}{\sigma_e^3}\right)$,

  and $\bar{\theta} = 1 - 6\theta/\pi$ (from Wierzbicki and co-workers). (2.12)

- Nahshon-Hutchinson [2008] parameter: $\omega = 1 - \cos^2(3\theta)$. (2.13)
- The Lode parameter: $\mu = \dfrac{2\sigma_2 - \sigma_1 - \sigma_3}{\sigma_1 - \sigma_3}$ (2.14)

2.4: DEFORMATION MEASUREMENTS VIA DIGITAL IMAGE CORRELATION

The deformations in the test section are established through the use of 3D DIC, an optical measurement technique that provides full-field, 3D displacements and surface strains. These measurements are enabled by spaying a fine speckle pattern of black paint on the test section over an undercoat of white paint as shown in Fig. 2.2. As mentioned previously, the test specimens are slightly eccentric, and were oriented such that the thinner side was monitored by the DIC cameras, as failure tended to occur in this region.

Our DIC system uses two 5 megapixel cameras equipped with 50 mm lenses and an aperture setting of about f/16. This aperture setting maximizes the depth of field, but also necessitated the use of additional lighting. The cameras were positioned approximately 12.2 inches (31 cm) away from the specimen surface, and positioned about 3.9 inches (9.8 cm) apart. This setup enabled monitoring deformation of about 1/3 of the circumference of the test section. During the test, images are initially acquired at 5 s intervals, and 2 s as the stress maxima are approached and beyond. An independent LabVIEW data acquisition system, which is run on a common time base as the DIC system, monitors the axial load and torque as well as the machine displacement and rotation. However, more accurate average elongation (δ) and rotation (ϕ) of the test section are evaluated from the position of the thick edges of the test section in the DIC images (see Fig. 2.2 and triangular markers in Fig. 3.4).

2.4.1: ARAMIS

The DIC images are analyzed using the ARAMIS v6.3 software at the completion of the test. The computed deformation depends on the *facet size* and *facet spacing*. A facet is an initially square zone of the monitored image whose deformation is tracked via the correlation process; facet spacing is the distance between the centers of adjacent (intersecting) facets. The facet size chosen for this analysis is 19x19 pixels (~0.3x0.3 mm) and the spacing is 6 pixels (~96 μm).

The image of the 3D surface is discretized into a finite number of points representing the centers of the facets. The number of points, which is dictated by the facet spacing, is specified by the user to balance resolution, accuracy, and computational expense. The facet spacing of 6 pixels, together with the camera positioning and resolution, results in 80 to 100 thousand discrete data points over the entire observable area of the specimen. The undeformed coordinates of these points are calculated in a fixed global coordinate system. The neighborhood of each of these discrete points is approximated by a plane tangent to the surface in which a 2D coordinate system is established. Then, the points that surround the point at which the local 2D coordinate system is centered are projected onto this tangent plane in the undeformed and deformed configurations forming a 3x3 point grid. The software then computes the 2D deformation gradient tensor $\boldsymbol{F}$ that maps points from their reference to their current configuration assuming a bi-linear interpolation of the displacement.

Some additional details particular to ARAMIS that are important to the post-processing of the data are:

- When the software cannot locate a facet in a particular stage, its corresponding point is lost and no deformation information is available for that point in that stage

only. If, however, the software is then able to locate the same facet in a subsequent stage, the point's displacement and strain information is once again available in this subsequent stage. The integrity of a point that drops in and out of the calculation is, in our experience, questionable.

- While the displacement of a point is calculated directly from the correlation process, the calculation of its deformation gradient tensor considers its displacement and the displacement of the eight points surrounding it. ARAMIS, however, requires only as few as four neighbors to be present to compute the strain at a point. It has been observed that data for points with missing neighbors is often error prone.

In experimental settings that are limited to uniform and moderate deformations, these issues are not of great significance. However, as will be detailed in Chapters 3 and 4, these tension-torsion experiments involve very large, highly-localized deformations, and it is the strain in these regions that we are interested in the most. As a result, establishing the strains in these zones and minimizing the influence of spurious data required significant effort.

2.5: ESTABLISHING STRAINS

Two methods for computing strains from the deformation gradient tensor $\boldsymbol{F}$ will be presented. The first method, referred to as the *Total Strain* method, was employed in Scales et al [2016]. The second method, referred to as the *Incremental* method, was more recently adopted for the calculations in Scales et al. [2019].

2.5.1: Total Strain

This method for calculating strains was adopted as it provides a direct measurement of the failure strain and is consistent with the results of HKR13. The total von Mises equivalent strain, computed from the principal logarithmic strains, serves as an ideal measure since it does not depend on the stress state or an assumed constitutive model. Polar decomposition of $\boldsymbol{F}$ gives the stretch tensor $\boldsymbol{U}=[\boldsymbol{F}^T\boldsymbol{F}]^{1/2}$. The in-plane principal stretches, λ_α, α = 1,2, are the eigenvalues of the stretch tensor, and the principal logarithmic strains are given by $e_\alpha = \ln(\lambda_\alpha)$. By invoking incompressibility and neglecting elastic deformations $\lambda_3 = (\lambda_1\lambda_2)^{-1}$ and $e_3 = -(e_1+e_2)$. Thus the equivalent plastic strain can be expressed as:

$$e_e^p = \left[\frac{4}{3}(e_1 + e_1e_2 + e_2)^2\right]^{1/2}. \tag{2.15}$$

The nominal axial and shear strain components are taken directly from the deformation gradient tensor:

$$\varepsilon_{xx} = F_{xx} - 1 \text{ and } \gamma_{\theta x} = \tan^{-1}\left(\frac{F_{\theta x}}{F_{xx}}\right). \tag{2.16}$$

Implementation

To establish the strains within the circumferential zone in which the deformation localized, each vertical column of points that crossed this zone was scanned and the maximum equivalent plastic strain in each column was recorded. To filter out potentially erroneous data points, the ratio of axial strain to shear strain was then calculated at each of these column maxima; only those whose ratio was within one-half of a standard deviation of the mean ratio were retained in that stage. This filtering scheme was employed in every stage individually, and did not take into account the results of preceding stages. In the presentation of results in Chapter 3, the mean strains of all profile maxima that pass the

filtering are designated as *DIC Mean*. Among those points, the one with the greatest equivalent plastic strain in the last stage prior to failure is designated as *DIC Max*.

2.5.2: Incremental Strains

The primary shortcoming of the *Total Strain* method is that it does not account for the large rotation of the material frame that occurs in some of these experiments. Faleskog and Barsoum [2013] showed that integration of the incremental measure of strain to be more accurate for shear dominant stress paths, and an ongoing effort to numerically reproduce these TT experiments required the calculation of the work-conjugate incremental strains (Chen et al. [2019]). Therefore, the following method for computing the equivalent strain and strain components is also implemented. The 2D incremental strain at a point is computed from:

$$d\boldsymbol{\varepsilon} = sym(d\boldsymbol{F}\boldsymbol{F}^{-1}) \tag{2.17}$$

where $d\boldsymbol{F}$ for stage n is approximated discretely by $d\boldsymbol{F} \approx (\boldsymbol{F}_n - \boldsymbol{F}_{n-1})$. Then the work-compatible equivalent plastic strain *increment* is computed using the equivalent stress of an adopted constitutive model according to

$$de_e^p\Big|_n = \frac{\sigma_{ij} d\varepsilon_{ij}}{\sigma_e} = \frac{\sigma_{xx} d\varepsilon_{xx} + \sigma_{\theta\theta} d\varepsilon_{\theta\theta} + 2\sigma_{x\theta} d\varepsilon_{x\theta}}{\sigma_e}, \tag{2.18}$$

where the elastic components of the strain increments are again neglected. Finally, this quantity is integrated from the reference to the current stage, N:

$$e_e^p = \int_n de_e^p\Big|_n \approx \sum_{n=1}^{N} de_e^p\Big|_n \quad . \tag{2.19}$$

The individual strain components can be integrated the same way. A significant difference in the two calculation methods is that, as seen in Eq. 2.18, the work-compatible equivalent plastic strain depends explicitly on the stress history and the adopted constitutive model. It

will be shown that the difference between the two methods is negligible for many of the experiments, but becomes increasingly noticeable as the stress state becomes more shear dominant.

Implementation

An attempt was first made to calculate strains incrementally using the same filtering scheme described above for the *Total* method, but difficulties arose. These issues were primarily related to the aforementioned behavior of the ARAMIS software. Specifically, it is unclear how one may go about computing an increment of strain at a point when that point does not exist in every stage. Furthermore, when calculating the strains incrementally, it was found that the old filtering method allowed some points to pass that exhibited erroneous behavior.

In light of these issues, a more-rigorous filtering scheme was developed and implemented:

- Only points that exist in every stage are considered.
- Point columns are scanned, and the location of the maximum equivalent strain in each column is identified.
- Column maxima within columns that are missing other points within two-thirds of the initial wall-thickness above and below the maximum are rejected.
- Column maxima that do not have all eight neighbors are rejected.

These criteria readily facilitate the calculation of strains incrementally. However these requirements alone do not necessarily eliminate all spurious data. To remove such points, a final filtering step is employed in which points whose strain “grows too quickly” are rejected from further consideration, as these are judged to most likely be erroneous. Of

the remaining column maxima, *DIC Mean* and *DIC Max* are defined in the same fashion as described above.

2.6: SUMMARY

A robust setup for combined tension and torsion experiments was developed, with the primary goals of permitting the stresses and strains in the test section to be calculated directly from experimental measurements. The test section was designed to enable localized deformations to develop freely, and for that deformation to be directly observable. The stresses are computed directly from the recorded force, torque, and specimen geometry. 3D DIC is used to monitor the deformation in the test section and provide a direct measurement of the strains. Its high resolution enables tracking the evolution of localization within the narrow localizing zone, but the technique also brings its own set of challenges, so filtering schemes appropriate to the problem were incorporated.

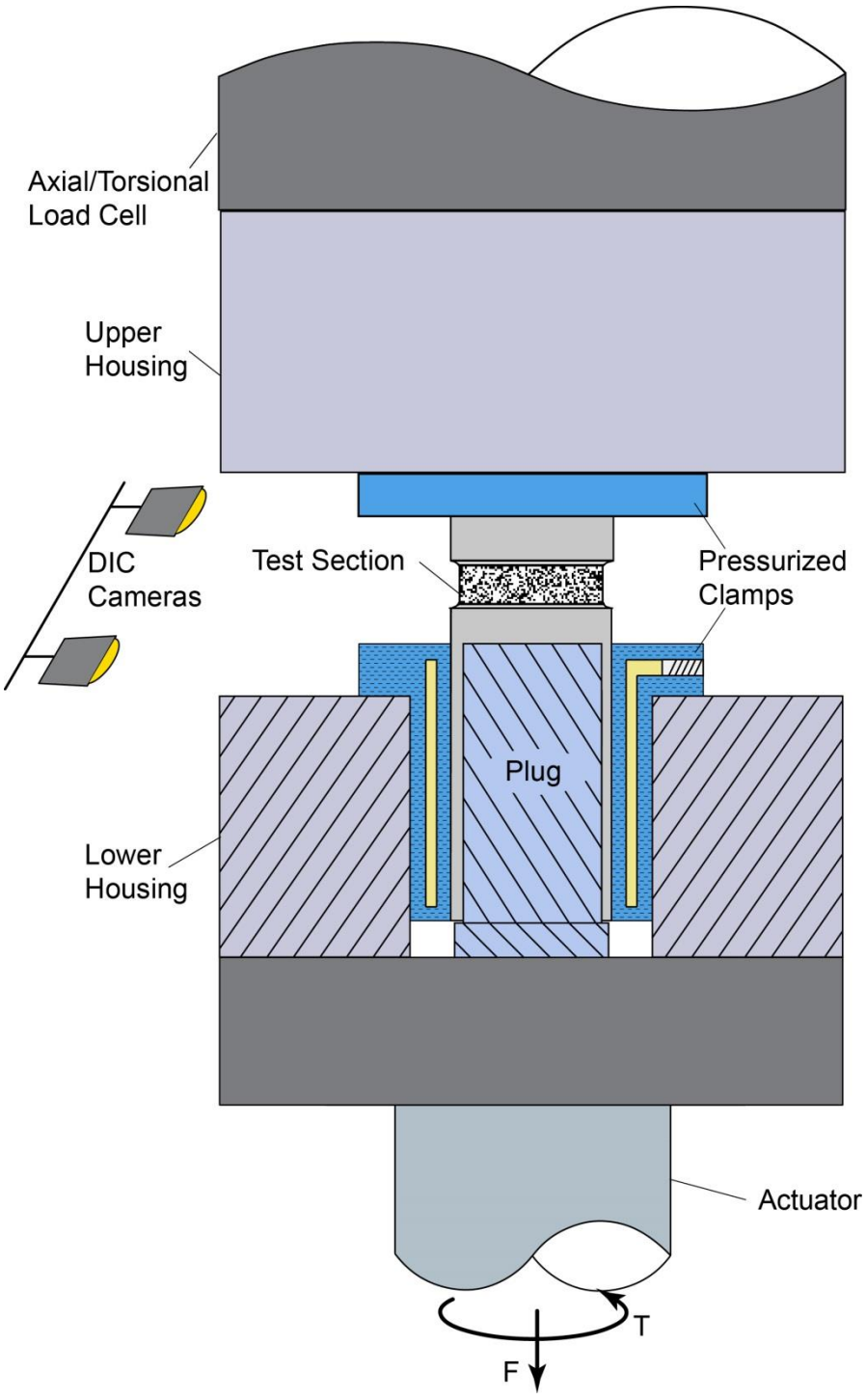

Fig. 2.1: Schematic of the tension-torsion experimental setup.

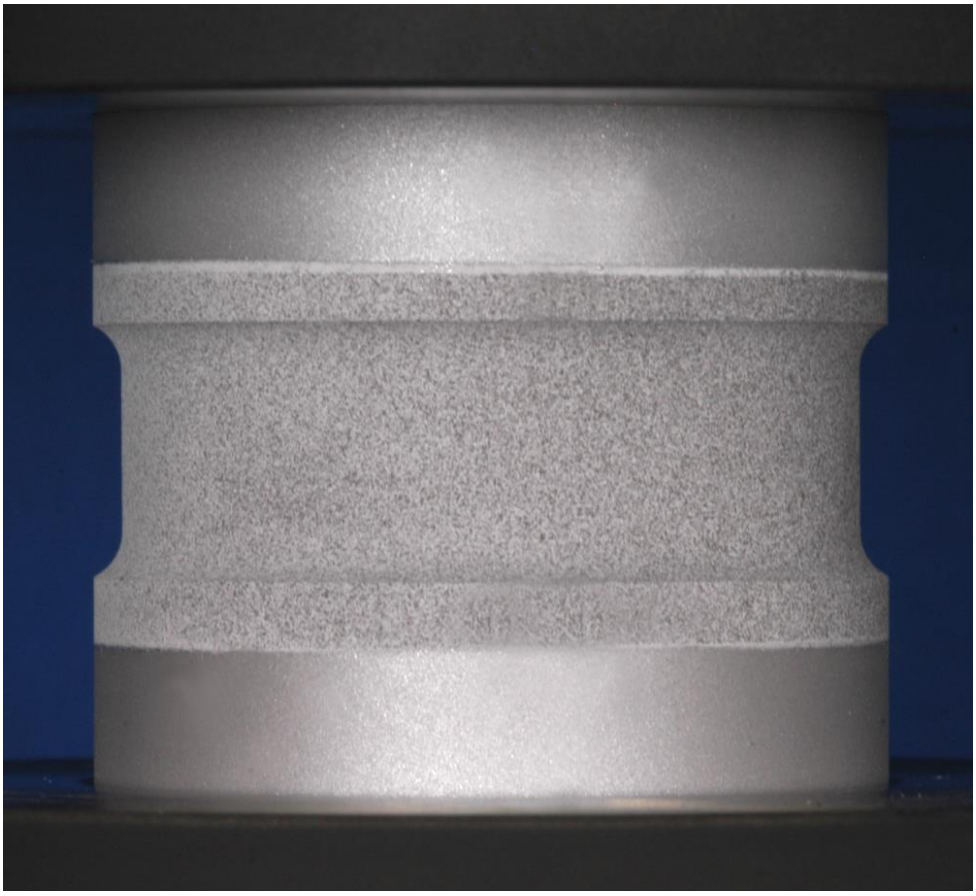

Fig. 2.2: A tension-torsion specimen with spray paint speckle pattern for DIC.

Chapter 3: Tension-Torsion Experiments - Set I[1]

This chapter presents the results from a first series of radial-path tension-torsion (TT) experiments covering triaxiality values from 0.07 to 0.58, following the test setup and procedure described in Chapter 2. The test specimens used in these experiments originated from extruded Al 6061-T6 tubes manufactured by Alcoa (see Haltom et al. [2013] for details regarding the microstructure of this particular tube stock). The stock tubes had a 2-inch nominal OD and wall thickness of 0.125 inches (51 mm/3.2 mm). Thus, to achieve the desired wall thickness in the test section of the specimens, the OD was machined to 1.826 inches (46.4 mm). Figure 3.1 presents a schematic of the machined tubes. The plugs inserted into the gripped region of the tubes had an OD of 1.750 inches (44.5 mm). Deformations were established via 3D Digital Image Correlation (DIC), and results for this series were computed using the *Total Strain* method as outlined in Section 2.5.1. Therefore, the influence of a chosen constitutive model is not considered.

3.1: Results for Exp. 17, $\alpha = 1.0$

The results from Exp. 2-17 with a stress ratio α = 1.0 are detailed to illustrate a typical experiment. The test section diameter (D_o), wall thickness (t_o), wall eccentricity (Ξ_o) and other parameters of the experiment are listed in Table 3.1. The experiment was run at a rotation rate of 8.7x10^{-5} rad/s resulting in a test section shear strain rate of $\dot{\gamma} \approx 2\times10^{-4}$/sec while deformation was uniform. Figure 3.2 shows the nominal axial-shear stress ($\Sigma - \mathcal{T}$) radial path followed in this experiment. The resultant shear stress-rotation ($\mathcal{T}$-ϕ) and axial stress-elongation ($\Sigma - \delta/L_g$) responses are respectively shown in

[1] Scales, M., Tardif, N., Kyriakides, S., (2016). Ductile failure of aluminum alloy tubes under combined torsion and tension. *Int. J. Solids Struct.* **97–98**, 116–128. (Prepared specimens, performed tests, analyzed data, and wrote the paper)

Fig. 3.3 (a) and (b), where L_g is the nominal length of the test section taken to be 0.62 inches (15.8 mm). The shear response traces the expected trajectory comprised of a linear elastic section followed by some hardening. At higher rotation, the stiffness of the response gradually decreases and a stress maximum develops at a rotation of about 7.3^o (indicated by ^). The maximum indicates that an instability is developing, but the rotation-controlled loading enables tracking of the descending part of the response. The shear stress initially drops gradually with rotation, and at a faster rate at higher values of ϕ. The precipitous drop in stress at rotation of 9.68^o is associated with rupture in part of the specimen. The corresponding axial stress-elongation response in Fig. 3.3 (b) follows a similar trajectory with the stress maximum occurring at approximately $0.035\delta/L_g$. An extended descending post-maximum response was again recorded with rupture occurring at 0.044 δ/L_g.

The maximum nominal stresses recorded ($\Sigma_{max} - \mathcal{T}_{max}$) are listed in Table 3.1. The nominal and Cauchy stresses at failure, ($\Sigma_f - \mathcal{T}_f$) and ($\sigma_f - \tau_f$) respectively, are listed in Table 3.2. The latter are used in Eqs. (2.9) and (2.10) to evaluate the mean and equivalent stress at failure also listed in Table 3.2.

The deformation of the test section was monitored by stereo DIC, which for this experiment resulted in the acquisition of 610 images. It is computed from each image on the part of the test section that contains the visible localization and eventual crack. Figure 3.4 shows the region of the speckled test section analyzed in this experiment. It has an angular span of approximately 60^o and covers the central third of the test section. It consists of approximately 10,000 discrete points arranged in a uniform grid in the undeformed configuration. The strain is evaluated at each point using its deformation gradient tensor as outlined in Section 2.5.1. We will use ten stations along the loading

history to demonstrate the evolution of deformation. These stations correspond to the numbered bullets marked on the two responses in Fig. 3.3.

Figure 3.5 shows six of the DIC images with color contours of the equivalent plastic strain, e_e^p, as defined in Eq. 2.15. The contours are generated from the points in the analyzed zone (note that each image has its own color scale). The zone shown has an angular span of 47° and a height of $3t_o$ ($X,Y \equiv$ undeformed Cartesian coordinates). In images 1 and 2, which both come well past the onset of plastic deformation but prior to the limit load, the deformation is uniform and grows from about 0.08 to 0.15. Just after the limit load in image 4, deformation is localizing across the central height. The strain here reaches about 0.25 while in its outer edges is of the order of 0.15. In image 6, further down the descending parts of the responses, the deformation has developed a more significant gradient with the strain reaching levels of the order of 0.32 in the center. The sharpening of the strain gradient across the zone continues in image 8, reaching a maximum value of about 0.45. Image 10 is the last one recorded before the specimen ruptured. Here the average maximum strain reaches a level of the order of 0.75 but with some points having even higher values. It is worth mentioning that the strain at the upper and lower edges of images 4 through 10 remains at about 0.15. These parts of the test section are outside the localization zone and, as a result, tend to unload elastically because of the overall drop in the loads.

A more quantitative demonstration of the localization that takes place comes from strain profiles taken across the test section. Figure 3.6 shows how the strain along a single column of points, spanning a height of about $4t_o$, evolves during the test. The profiles correspond to the ten stations marked on the responses in Fig. 3.3. We have chosen to show the column of points that passes through the point at which the maximum strain was

recorded in the last image before failure (located at $(X/R_o, Y/t_o)$ = (0.14, -0.18)). Profiles 1 and 2 correspond to loading stations that are before the stress maxima and consequently the strains recorded are essentially constant across this zone. Profiles 3 and 4 occur just after the load maxima and are seen to bend upwards to some degree, an indication that deformation is starting to localize in the central part of the height. Deformation concentrates in an increasingly narrower section in profiles 5 to 7 with the strain profiles developing a central crest that continues to grow, while on either side of its approximately $2t_o$ height the strain remains nearly unchanged. Interestingly, the strain at the crest of profile 8 is about 0.46, which is not very different from the mean value that was reported from the corresponding image in Fig. 3.5. In the last profile, 10, the strain gradient becomes even sharper, with the strain developing a sharp spike. The narrow concentration of strain challenges to some degree the resolution of our DIC but, at the same time, justifies our choice of facet size and spacing. The maximum strain recorded is 0.921 whereas the average of the maxima is 0.745.

Another effective demonstration of how this deformation evolves is to plot the equivalent plastic strain, e_e^p, against the specimen rotation ϕ. Figure 3.7 (a) shows this plot, and includes both the *DIC Mean* and *DIC Max* measurements (see Section 2.5.1). The locations of the stress maxima are identified by "LL", while the last point of each represents the onset of rupture (marked with x). The two measures of strain initially trace essentially the same trajectories, growing almost linearly with rotation. Deformation accelerates moderately as the stress maxima are approached reaching values of about 0.22. Beyond the stress maxima, the two strains experience essentially exponential growth. The two measures continue to follow each other quite well, separating at the end. For the last point the *DIC Mean* strain is 0.745 $(\overline{e}_f^p)$ and the *DIC Max* 0.921 (e_f^p), both listed in Table 3.2.

Recall that the images are acquired at 2-second intervals. The increase in the *DIC Max* strain between the last two images is of the order of 0.2. This demonstrates the very rapid growth of deformation just before rupture. The significance of this is underscored by the observations in (Ghahremaninezhad and Ravi-Chandar [2012, 2013], HKR13, Gross and Ravi-Chandar [2016]) that it is not until these last stages of life that voids form, grow, and coalesce, leading to rupture. The rapid growth also indicates that the reported "failure strain" must be a lower bound.

DIC also enables evaluating the deformations and failure strains in a manner similar to HKR13. Recall that those measurements were based on the deformation of two 0.031 x 0.031-inch (0.8 x 0.8 mm) grid squares etched on the specimen. In the way of replicating this, the DIC measured strains are averaged over a 0.0625 x 0.0625 inches (1.6 x 1.6 mm) square around each of the profile maxima. The mean of the averages across this entire region is evaluated and the resultant strain measure is designated as *DIC Macro*. The e_e^p calculated in this manner for the current experiment are plotted against ϕ in Fig. 3.7 (a). This strain trajectory follows the other two closely up to the location of the stress maxima. Once localization initiates, the *Macro* strains do not grow as fast due to the larger "gage area" over which they are calculated. The final strain value before failure is 0.495, which is significantly lower than the other two estimates. This value of "failure strain" compares with 0.631 for $\alpha = 1.0$ reported in HKR13.

It is also instructive to report the strain recorded outside the localization zone. For this purpose the average strain in a small zone in the test section, identified in Fig. 3.7 (b) as “Site B”, was tracked and its evolution with the rotation angle is included in Fig. 3.7 (a). The zone has an area $0.5t_o$ x $2.5t_o$ and is located a distance $2.5t_o$ below the site where the maximum strain was recorded—identified as “A” with a solid bullet. The strain follows

the other three measures up to a rotation of about 6^o just before the load maxima. Contrary to the strain measured inside the localizing band, the deformation in this zone stops growing at higher rotations and develops a plateau at 0.187.

As described in Chapter 2, the specimen test section was designed to have a region of nearly uniform stress that also allows localization to develop freely. These features allow direct measurement of both the stress and deformation throughout the test. Furthermore, the wall thickness of the test section was chosen thin enough to make the radial stress negligibly small but thick enough to prevent torsional buckling at large rotations. A drawback of this design is that some small amount of radial displacement could not be prevented. Figure 3.8 shows the radial displacement, w, across the test section at three stations during the loading history ($R = D/2$). Profiles 1 and 2 correspond to the numbered bullets on the responses in Fig. 3.3, and the third corresponds to the load maxima (LL). The thicker edges of the test section are hardly deformed while the center develops a hoop strain of about -1.5% at the limit load. In calculating the stresses in Section 2.3, the test section was assumed not to deform radially which lead to $\sigma_{\theta\theta} = \sigma_{xx}/2$ (for von Mises). The deformation in Fig. 3.8, although small, implies that the actual value of $\sigma_{\theta\theta}$ is somewhat smaller than assumed and varies along the width of the test section. This issue should be further investigated in the modeling of these experiments.

3.2: SUMMARY OF RESULTS

Fourteen tension-torsion radial stress path experiments were performed in this study for stress ratios $0.25 \leq \alpha \leq 4.0$ in which the deformations were monitored using DIC. An additional experiment was performed in which the tubular specimen was loaded in tension to failure. This test is designated as *plane strain* (PS), realizing that the test section

underwent some radial deformation. For most experiments the results are largely similar to those of Exp. 2-17 and thus will be presented here only in summary form. Notable differences that occurred in some experiments and related observations will be pointed out. The main problem parameters of each test are listed in Table 3.1 and the main stress and deformation variables at failure in Table 3.2. The elastic modulus and yield stress of each mother tube appear in Table 3.3.

Figure 3.9 shows the recorded nominal axial-shear stress histories ($\Sigma - \mathcal{T}$) for twelve of the experiments. Figures 3.10 (a) and (b) show respectively the shear stress-rotation ($\mathcal{T} - \phi$) and axial stress-displacement ($\Sigma - \delta/L_g$) responses of these experiments. The experiments for α = 0.5 and 1.0 were repeated and only one for each stress ratio is included in these figures. Figure 3.11 shows plots of the *DIC Mean* measure of the equivalent plastic strain as a function of the rotation angle. Marked on the responses in the three figures with a diamond symbol (◆) are the points corresponding to the nominal stress maxima. In all cases the specimen continued deforming well past the load maxima with the recorded nominal stresses dropping and the deformation localizing in the manner described in Section 3. In the case of the stress paths in Fig. 3.9, rupture is marked with a triangular symbol (▲) while in Figs. 3.10 and 3.11 failure corresponds to the last point plotted.

The shear stress-rotation responses in Fig. 3.10 (a) exhibit the expected trend, with the shear stress and rotation angle at failure increasing as α decreases. In all cases a maximum stress was achieved. The axial stress-elongation responses in Fig. 3.10 (b) exhibit the opposite trend with the stress and elongation increasing with α. The responses beyond the limit load for $\alpha > 2.0$ are somewhat disordered, which reinforces the fact that the instability is sensitive to local conditions and consequently can vary from specimen to

specimen. The nominal stresses at failure, (Σ_f , $\mathcal{T}_f$), are listed in Table 3.2 along with the corresponding Cauchy stresses, (σ_f , τ_f), evaluated in accordance with Eq. 2.3 using the DIC mean measure of λ_3. Also listed are the equivalent von Mises and mean stresses σ_{ef} and σ_{mf} respectively.

The *DIC Mean* e_e^p - ϕ trajectories in Fig. 3.11 exhibit a similar trend to that in Fig. 3.7 (a) for α = 1.0. The strain initially grows nearly linearly with rotation, but in all cases its growth accelerates very significantly beyond the point when the load maxima occurred. We are reminded that this rapid increase in deformation takes place inside the localizing zone whereas the deformation outside it remains essentially at the level of the load maxima. The ends of the trajectories, although representing smaller values than the maximum strain measured at failure, replicate the trend of the failure strain in that they decrease with α and triaxiality (see Fig. 3.12 (a)). The nature of the deformation in the case of α = 0.25 was somewhat different from the other experiments, and its trajectory is therefore not included in this figure.

The measured *DIC Max* strains at the onset of failure are plotted against the measured triaxiality σ_{mf}/σ_{ef} in Fig. 3.12 (a) (symbol ■). Included are the corresponding strains reported in HKR13 (symbol ●), as well as the statistical estimated based on the deformed grain size in areas adjacent to the failure zones (symbol ●). Values of $\bar{\theta}$ and ω defined in Eqs. 2.12 and 2.13 are listed in Table 3.2. Discussion of these results will follow.

3.2.1: Additional Observations

- In this case of α = 0.25, the specimen underwent larger rotation than the rest, with the stress remaining essentially constant for the second half of the response. A distinct load maximum was difficult to establish, and the possibility of torsional

buckling late in the response cannot be ruled out. The extent of shear deformation sustained by the test section is demonstrated in the last DIC image recorded before rupture shown in Fig. 3.13 (a). Deformation localized into a much wider zone than was observed for larger stress ratios. Figure 3.13 (b) shows its width to cover the entire test section (~$10t_o$) which is about five times larger than that observed in Fig. 3.6 for $\alpha = 1.0$. Because of the extent of the deformation this zone developed a rough surface akin to the so-called orange peel. Most of the rotation occurred over the central half of the test section and this region developed a distinct relief with long ridges and valleys aligned with the rotation of the material (see Fig. 3.13 (c)). In this experiment failure occurred outside of the region monitored by DIC and so the failure strain reported is clearly lower than the actual value. For this reason an upward pointing arrow is placed above the data point plotted in Fig. 3.12.

- A small specimen containing one of the ends of the crack that developed in the $\alpha = 0.25$ experiment was submitted to Professor Eric Maire of INSA Lyon for analysis along with a similar size specimen from undeformed material. The specimens were scanned in his X-ray tomography facilities for the purpose of establishing initial and post-failure porosity (e.g., see Buffiere *et al.* [2010]; Maire et al. [2008]). The scanning was performed at 2 μm voxel size. At this resolution essentially no voids were observed in the undeformed material, though it remains possible that smaller voids went undetected. A small amount of porosity of 0.03% was observed in the deformed material in the neighborhood of the crack that did not appear to have contributed directly to the failure. This observation is in concert with those in Gross and Ravi-Chandar [2016] from in-situ SEM low-triaxiality testing on the same material (see also Ghahremaninezhad and Ravi-Chandar

[2013], Morgeneyer et al. [2014], Buljac et al. [2016]). They report that "second phase particles and voids impart little influence on the deformation in the neighborhood of the failure zone." The limited effect of voids was also reported in HKR13 where void formation was found to be delayed until the near end of life and to be limited to the immediate neighborhood of failure (see also Ghahremaninezhad and Ravi-Chandar [2012]).

- The experiments for $\alpha \geq 3.5$ were run under axial displacement control with the torsion under load control. Despite this, these three specimens separated completely in two at rupture and so it could not be determined if failure initiated inside the zone monitored. Deformation localized in a narrow zone similar to those of lower α experiments. However, the location of localization moved away from the center of the test section closer to one of the edge fillets as illustrated in Fig. 3.14 (a) for $\alpha = 4.0$. The axial profile of localization from the last image recorded in this experiment plotted in Fig. 3.14 (b) has a width of about $2t_o$, but the strain at the crest is significantly smaller than those for $\alpha = 1.0$ and 0.25 in Figs. 3.6 and 3.13 respectively. These observations hold also for the PS experiment with one difference: in this case the failure meandered to some degree as it propagated around the circumference.
- The plot of failure strain vs. triaxiality in Fig. 3.12 (a) is quite enlightening: e^p_{ef} exhibits a monotonic decrease with σ_{mf}/σ_{ef}, starting at values of about 1.6 at the lower triaxialities and ending at about 0.4 for the highest value considered. In other words, the trend is similar to that displayed in the HKR13 results, but the new strain levels are uniformly significantly higher because of the higher resolution provided by DIC. In fact the new failure strains are either higher or very close to

the grain level measurements of HKR13 for the experiments with $\alpha \leq 1.0$ and approach them from below for higher α.

- Included in Fig. 3.12 (a) are the failure strains yielded by the fifteen current experiments when averaged over an area that corresponds to the gage length of the grid measurements of HKR13—*DIC Macro*. This measurement follows the same trend as the HKR13 results. This confirms the veracity of the grid measurement scheme used in HKR13, and supports the notion that the failure strain is strongly dependent on the resolution to which deformation can be measured in localization zones with high gradients.
- Figure 3.12 (b) compares the *DIC Max* measures of failure strain with the corresponding *DIC Mean* values. The mean measures of strain at failure trace the same monotonic decrease with triaxiality as the max values but they are somewhat lower. However, they are at much higher levels than the *DIC Macro* measurements. This indicates that a key to measurements of failure strain is a technique with sufficient resolution to capture the high gradients associated with localization zones with a width of the order of the wall thickness that develop across the specimen.

3.3: CONCLUSIONS

This Chapter presented the results of a series of experiments in which tubular specimens with the same test section design of HKR13 are loaded to failure under radial paths of shear and tension. The fine grid-based method of monitoring the deformation in the preceding work is now replaced with 3D DIC. The test sections deformed essentially uniformly deep into the plastic range allowing measurement of the stresses and strains directly from the experiments. The nominal shear stress-rotation and axial stress-

elongation responses eventually developed load maxima beyond which deformation localized in narrow circumferential zones. 3D DIC enabled monitoring the surface deformation in the localizing zones up to the onset of rupture. The widths of the localization zones were shown to be of the order of the wall thickness and developed significant strain gradients across them. The failure strains reported came from the last image recorded prior to rupture and each represents the largest value in the zone monitored by DIC (usually in the neighborhood of failure). Thus the value reported could be different than the actual failure strain if failure initiated in a region not monitored. The stresses at failure are based on plane stress assumptions, which of course are not exactly true inside the localization zone.

The DIC-measured failure strains exhibit a monotonically decreasing trend with triaxiality, similar to that of the results of HKR13, but have significantly higher values due to the higher resolution of the DIC system. The maximum measured failure strains range from about 1.5 at lower triaxialities to 0.40 at higher triaxialities. Interestingly these values are close to the statistical grain level measurements of HKR13 for $\alpha \leq 1.0$.

The failure strain is plotted once more vs. triaxiality in Fig. 3.15 together with the results of Beese et al. [2010] for this same alloy. Their failure envelope exhibits a local maximum in strain at the triaxiality corresponding to uniaxial tension and drops for lower and higher values. The drop for lower triaxialities is clearly contrary to the current measurements and to those of HKR13 in which a uniaxial state of stress corresponds to $\alpha \approx 1.5$. More generally, the failure strains predicted in Beese et al. [2010] are significantly lower than the experimental results. Although some of these disparities may be due to differences in material processing (i.e., tubes vs. sheets and rods), we attribute the differences mainly to the fact that our specimen design permits localization to develop free

of constraints, and to the higher accuracy resolution measurement method used. A similar non-monotonic relationship between failure strain and triaxiality reported in Bao and Wierzbicki [2004] for Al-2024-T351 was refuted by results from tension-torsion experiments on the same material in Papasidero et al. [2015]. This difference is also most probably due to the more robust experimental setup and higher resolution diagnostic methods used in the more recent study.

Included in Fig. 3.15 is a Johnson-Cook based failure locus for this material from Lesuer et al. [2001]. It exhibits the expected monotonic decrease of failure strain with triaxiality but significantly underestimates the present failure strains.

The results presented confirm once more that establishing the onset of failure experimentally is very challenging, and the results are strongly influenced by the experimental set-ups and diagnostic methods used. Because of the experimental complexities, any measurement of strain at failure, even when the most advanced methods available are used, must be considered as a lower bound estimate. Estimates of failure strains based on numerical modeling, although necessary for some loading regimes, must incorporate carefully extracted material stress-strain responses and suitably calibrated constitutive models for the predictions to be dependable. A priori assumptions of stress-strain behavior or yield functions can lead to significant deviations from actual behavior.

These results must also be looked at in light of the observation that this alloy deforms to rather large strains free of damage. Thus it is expected that numerical models of a test that incorporate properly calibrated plasticity models will reproduce the measured responses, including the observed localization, to significant strain levels. Furthermore, the sharp strain gradients observed in the localization zones must guide the local discretization.

Table 3.1: Main parameters for tension-torsion radial stress path experiments.

Exp. No.	Tube No.	α	D_o in (mm)	t_o in (mm)	Ξ_o %	Σ_{max} ksi (MPa)	$\mathcal{T}_{max}$ ksi (MPa)
2-31	DC16	0.25	1.824 (46.32)	0.0372 (0.98)	4.2	6.98 (48.1)	27.8 (191.7)
2-35	DC16	0.375	1.826 (46.37)	0.0381 (0.97)	2.8	10.2 (70.3)	27.0 (189.2)
2-20	DC16	0.5	1.826 (46.38)	0.0379 (0.97)	2.3	13.2 (91.0)	26.6 (183.4)
2-22	DC16	0.5	1.825 (46.37)	0.0379 (0.93)	2.4	13.9 (95.8)	26.6 (183.4)
2-24	DC16	0.75	1.826 (46.37)	0.0383 (0.96)	4.8	19.7 (135.8)	26.0 (179.3)
2-17	DC15	1.0	1.827 (46.40)	0.0382 (0.98)	2.3	24.6 (169.6)	24.5 (168.9)
2-27	DC16	1.0	1.826 (46.39)	0.0384 (0.96)	3.5	23.7 (163.4)	23.2 (160.0)
2-34	DC16	1.25	1.825 (46.35)	0.0377 (0.96)	3.7	29.3 (202.0)	23.3 (160.6)
2-32	DC16	1.5	1.826 (46.37)	0.0380 (0.97)	2.6	33.1 (228.2)	21.9 (151.0)
2-9	DC14	2.0	1.825 (46.34)	0.0378 (0.96)	1.4	38.6 (266.1)	19.0 (131.0)
2-8	DC14	2.5	1.826 (46.37)	0.0384 (0.98)	0.8	41.1 (238.4)	16.8 (115.8)
2-30	DC16	3.0	1.826 (46.38)	0.0383 (0.97)	9.8	43.8 (302.0)	14.6 (100.7)
2-16	DC15	3.5	1.826 (46.39)	0.0380 (0.96)	3.2	45.1 (311.0)	12.4 (85.5)
2-15	DC15	4.0	1.826 (46.39)	0.0385 (0.98)	0.6	45.7 (315.1)	11.5 (79.3)
2-18	DC15	PS	1.825 (46.34)	0.0366 (0.97)	5.6	50.1 (345.4)	--

$$\Sigma = \alpha \mathcal{T}, \quad \Xi_o = \frac{t_{max} - t_{min}}{t_{max} + t_{min}}$$

Table 3.2: Stress and deformation variables at failure

Exp. No.	α	Σ_f ksi (MPa)	$\mathcal{T}_f$ ksi (MPa)	σ_f ksi (MPa)	τ_f ksi (MPa)	σ_{ef} ksi (MPa)	σ_{mf} ksi (MPa)	$\sigma_{mf}/\ \sigma_{ef}$	$\bar{\theta}$	ω	$\bar{e}^p_{ef}$	e^p_{ef}
2-31	0.25	6.63 (45.7)	26.4 (182.0)	6.7 (46.3)	26.7 (184.3)	46.7 (321.7)	3.4 (23.2)	0.072	0.206	0.898	1.282*	1.497*
2-35	0.375	9.3 (64.1)	24.9 (171.8)	9.3 (64.1)	24.9 (171.7)	43.6 (300.6)	4.6 (31.7)	0.106	0.307	0.537	1.313	1.703
2-20	0.5	12.6 (86.9)	25.4 (175.1)	13.5 (93.0)	27.2 (187.2)	48.5 (334.1)	6.7 (46.5)	0.139	0.401	0.653	1.127	1.374
2-22	0.5	13.4 (92.4)	25.7 (177.2)	14.3 (98.6)	27.4 (189)	49.1 (338.3)	7.2 (49.3)	0.146	0.421	0.623	1.204	1.623
2-24	0.75	18.5 (127.6)	24.4 (168.2)	20.6 (142.3)	27.3 (188.2)	50.5 (348.5)	10.3 (71.2)	0.205	0.596	0.352	0.972	1.116
2-17	1.0	23.0 (158.6)	23.0 (158.6)	26.9 (185.2)	26.8 (184.6)	51.9 (357.7)	13.4 (92.6)	0.258	0.760	0.136	0.745	0.921
2-27	1.0	22.0 (151.7)	21.6 (148.9)	26.3 (181.6)	26.5 (182.5)	51.2 (353.1)	13.2 (90.8)	0.262	0.771	0.124	0.877	1.018
2-34	1.25	26.6 (183.4)	21.1 (145.5)	33.1 (228.2)	26.3 (181.3)	53.8 (370.6)	16.5 (113.7)	0.308	0.916	0.009	0.720	0.862
2-32	1.5	29.9 (206.1)	19.8 (136.5)	39.0 (268.9)	25.8 (177.9)	56.0 (389.1)	19.5 (134.4)	0.348	0.951	0.003	0.649	0.748

* Failure occurred outside of the DIC viewing area

Table 3.2 (cont'd): Stress and deformation variables at failure

Exp. No.	α	Σ_f ksi (MPa)	$\mathcal{T}_f$ ksi (MPa)	σ_f ksi (MPa)	τ_f ksi (MPa)	σ_{ef} ksi (MPa)	σ_{mf} ksi (MPa)	$\sigma_{mf}/\ \sigma_{ef}$	$\bar{\theta}$	ω	$\bar{e}^p_{ef}$	e^p_{ef}
2-9	2.0	33.1 (228.2)	16.3 (112.4)	47.5 (327.2)	23.4 (161.1)	57.7 (397.8)	23.7 (163.6)	0.411	0.730	0.169	0.618	0.725
2-8	2.5	35.9 (247.5)	14.7 (101.4)	51.0 (351.3)	20.8 (143.3)	57.0 (392.7)	25.5 (175.7)	0.447	0.598	0.349	0.571	0.687
2-30	3.0	39.6 (273.0)	13.2 (91.0)	55.2 (380.3)	18.4 (127)	57.5 (396.1)	27.6 (190.2)	0.480	0.463	0.558	0.474	0.663
2-16	3.5	38.5 (265.4)	10.6 (73.1)	55.5 (382.9)	15.2 (105.1)	54.9 (378.3)	27.8 (191.4)	0.506	0.355	0.720	0.465	0.553
2-15	4.0	38.1 (262.7)	9.5 (65.5)	54.4 (374.9)	13.6 (93.6)	52.6 (362.9)	27.2 (187.5)	0.517	0.306	0.786	0.481	0.584
2-18	PS	46.4 (319.9)	--	58.7 (404.9)	0.4 (3.0)	50.9 (350.7)	29.4 (202.5)	0.577	0.000	1.000	0.324	0.403

Table 3.3: Material properties in uniaxial tension

Tube No.	E Msi (GPA)	Σ_o ksi (MPa)
DC14	9.80 (67.6)	43.2 (298)
DC15	10.0 (69.0)	43.4 (299)
DC16	9.79 (67.5)	43.9 (303)

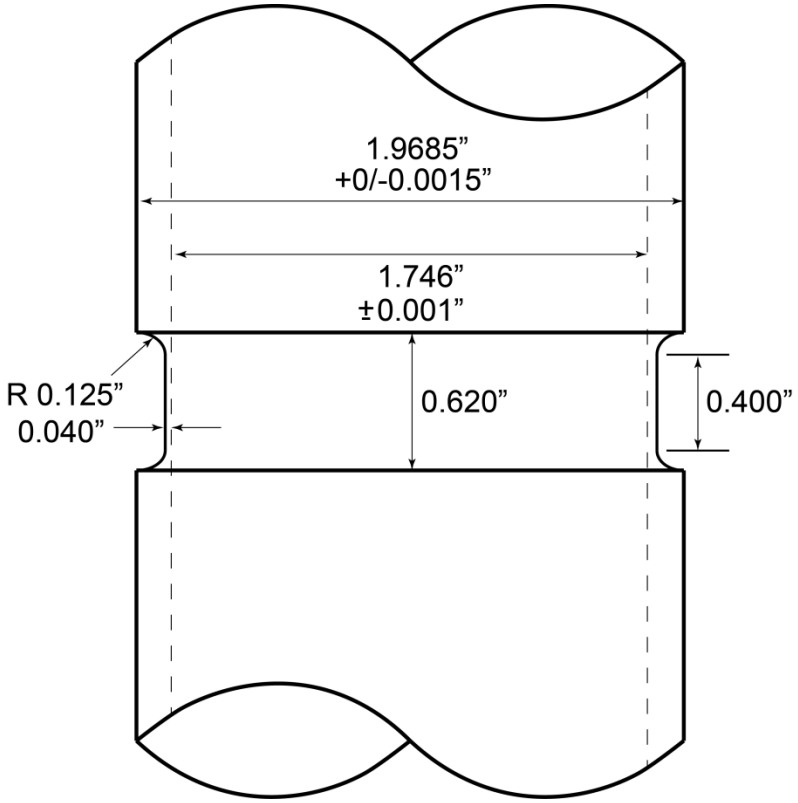

Fig. 3.1: Tension-torsion test specimen geometry (1 in = 25.4 mm).

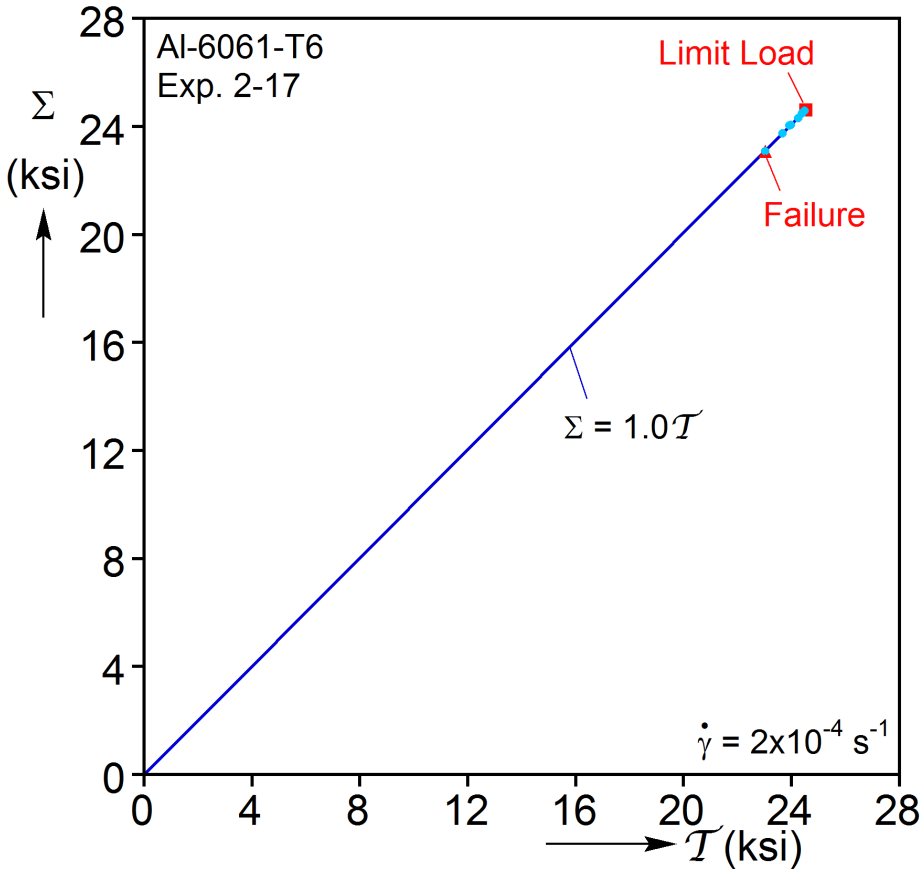

Fig. 3.2: Nominal stress loading path of experiment 2-17. In this case, $\alpha = 1.0$, so axial and shear stress are equal.

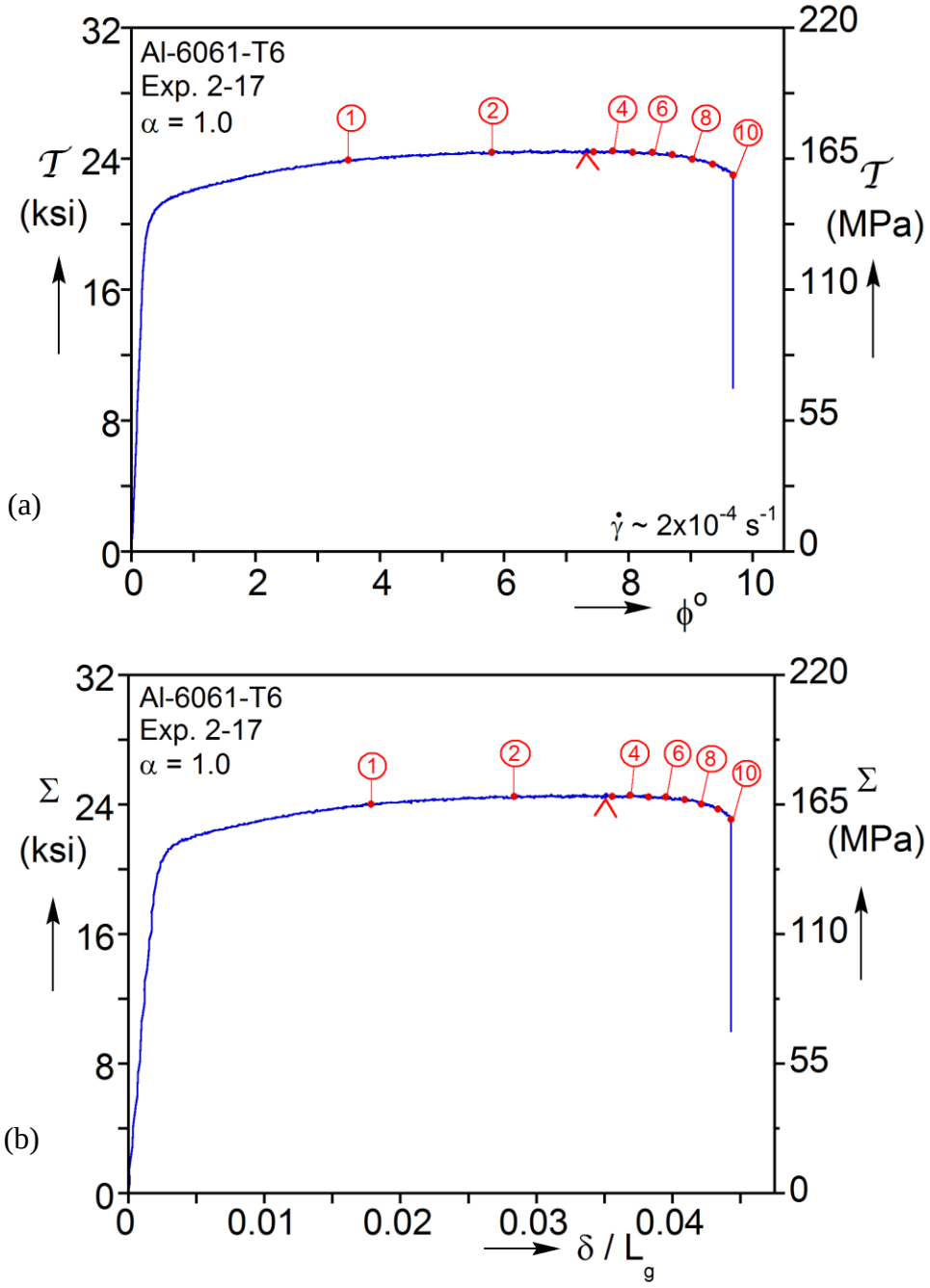

Fig. 3.3: (a) Nominal shear stress-rotation and (b) axial stress-elongation responses for $\alpha = 1.0$.

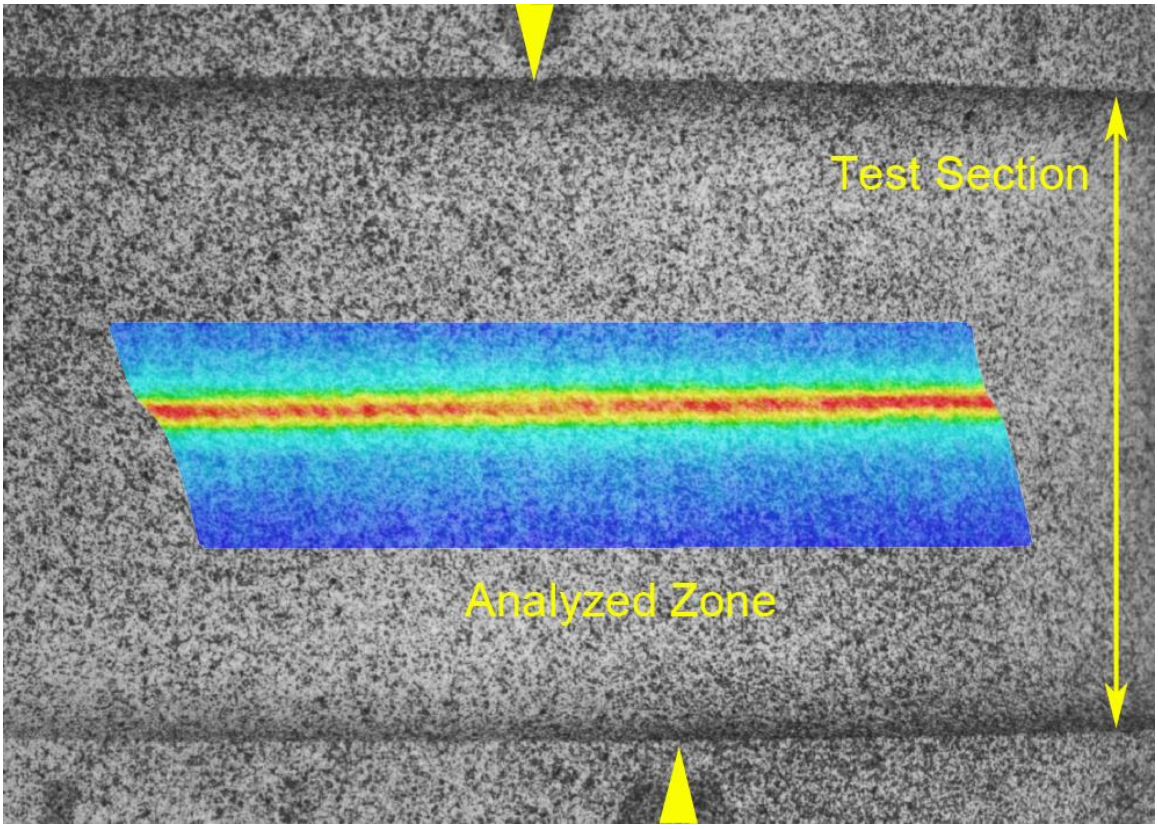

Fig. 3.4: DIC image of the test section taken shortly before failure with computed strains overlaid for $\alpha = 1.0$

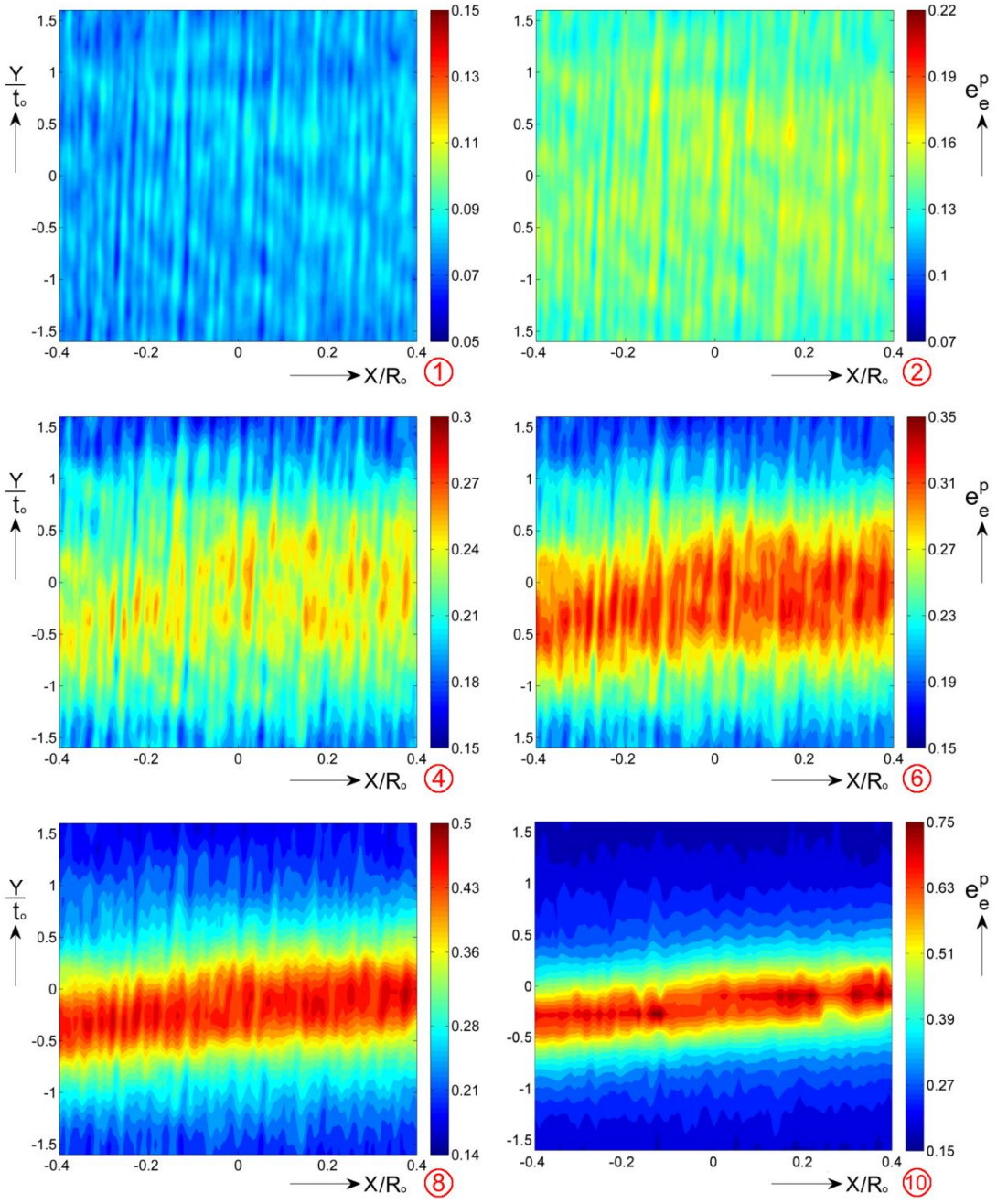

Fig. 3.5: Equivalent plastic strain contours of the analyzed zone for $\alpha = 1.0$. Numbers correspond to the stations marked in Fig. 3.3 (note that each contour has a different color scale

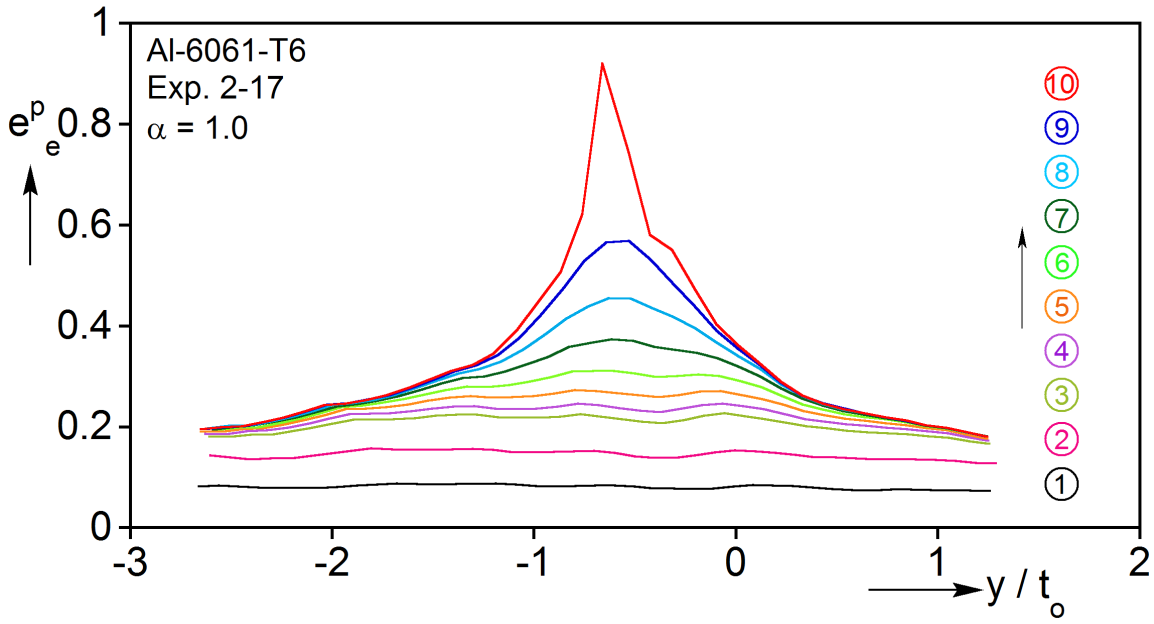

Fig. 3.6: Equivalent plastic strain across the localization zone at the location of maximum strain. Numbers correspond to the stations marked in Fig. 3.3.

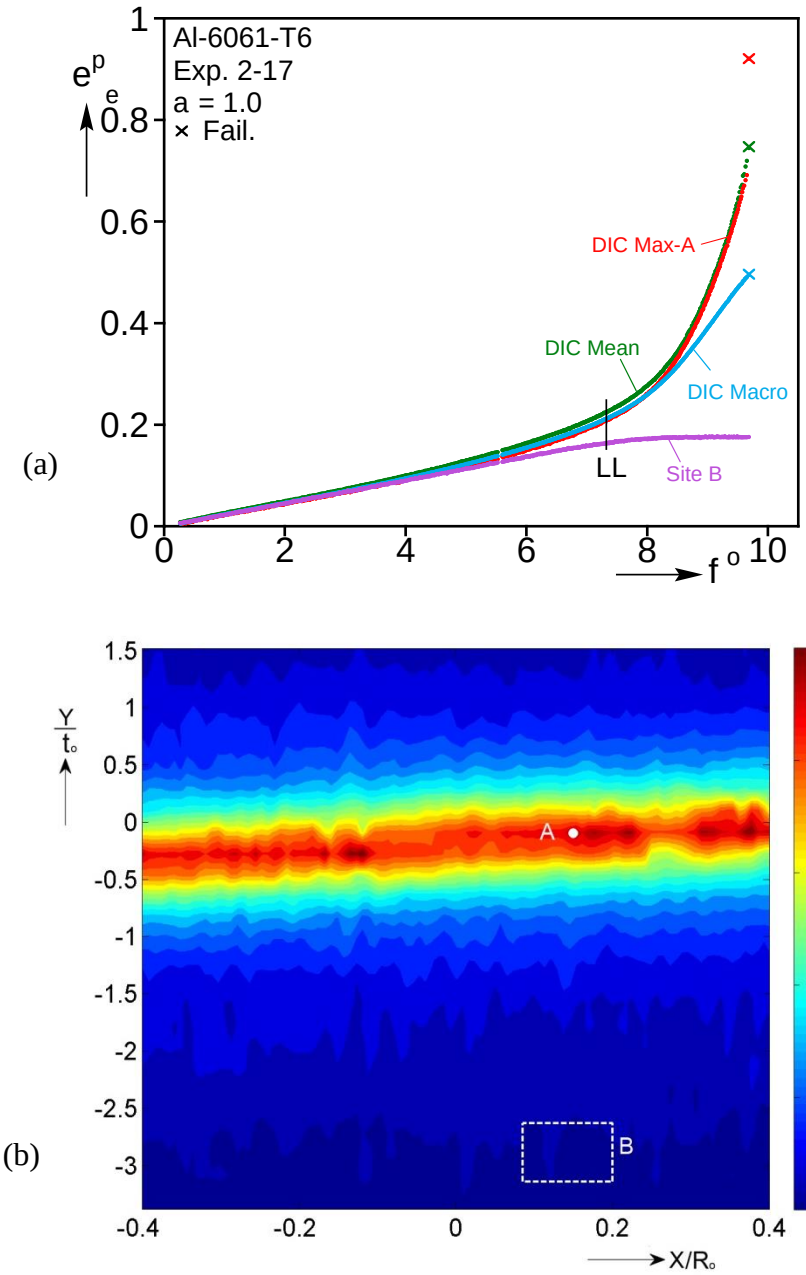

Fig. 3.7: (a) Equivalent plastic strain plotted against specimen rotation. DIC Max-A is the strain at the point of maximum strain in the final stage prior to failure, and corresponds to point A in (b). The strain at site B is averaged over all points within the box shown in (b).

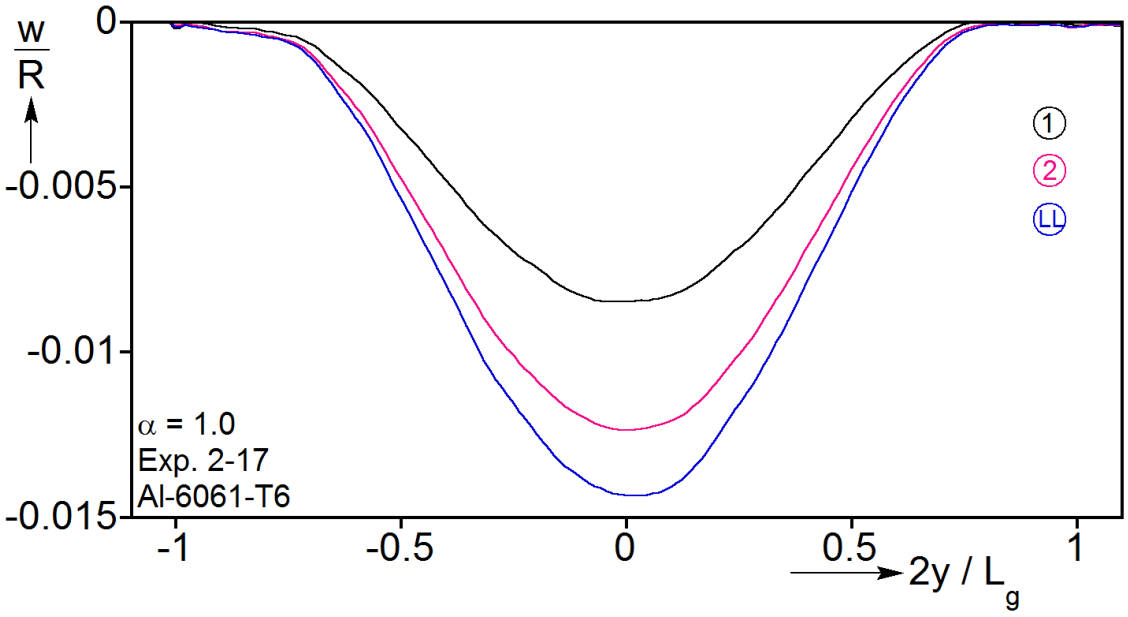

Fig. 3.8: Radial displacement across the specimen test section. Numbers correspond to the stations marked in Fig. 3.3.

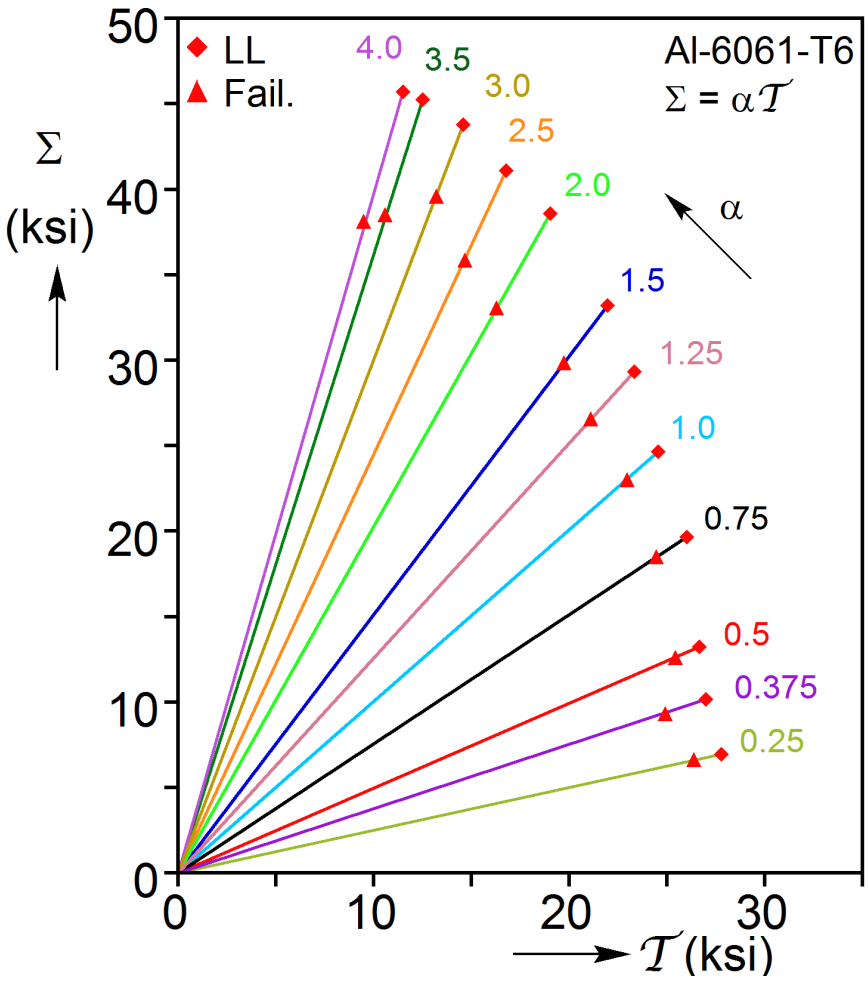

Fig. 3.9: Nominal shear-axial stress paths for the experiments performed. On each path the symbol ◆ represents the limit load, and ▲ the stresses at failure.

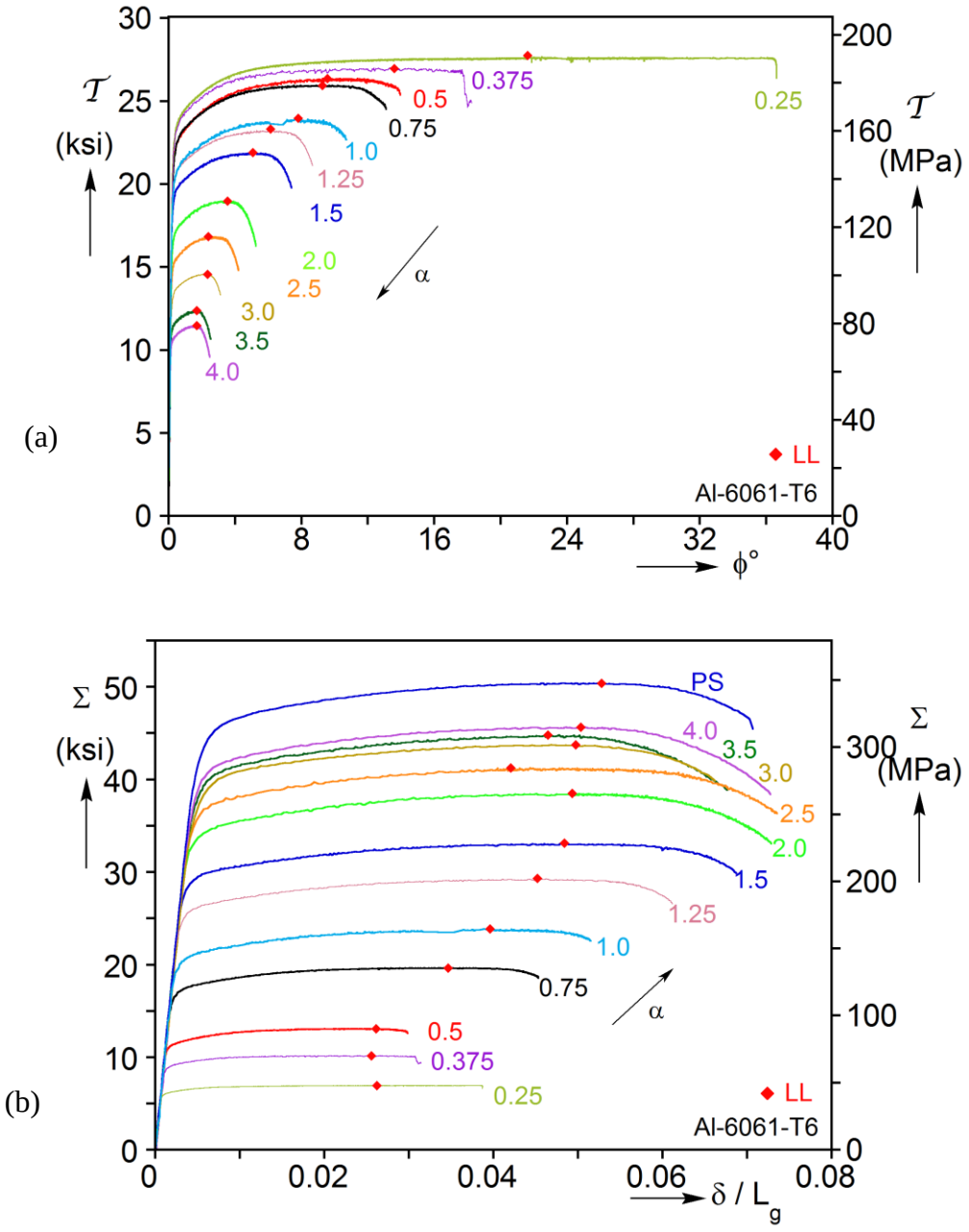

Fig. 3.10: (a) Nominal shear stress-rotation responses, and (b) axial stress-elongation responses for thirteen experiments performed.

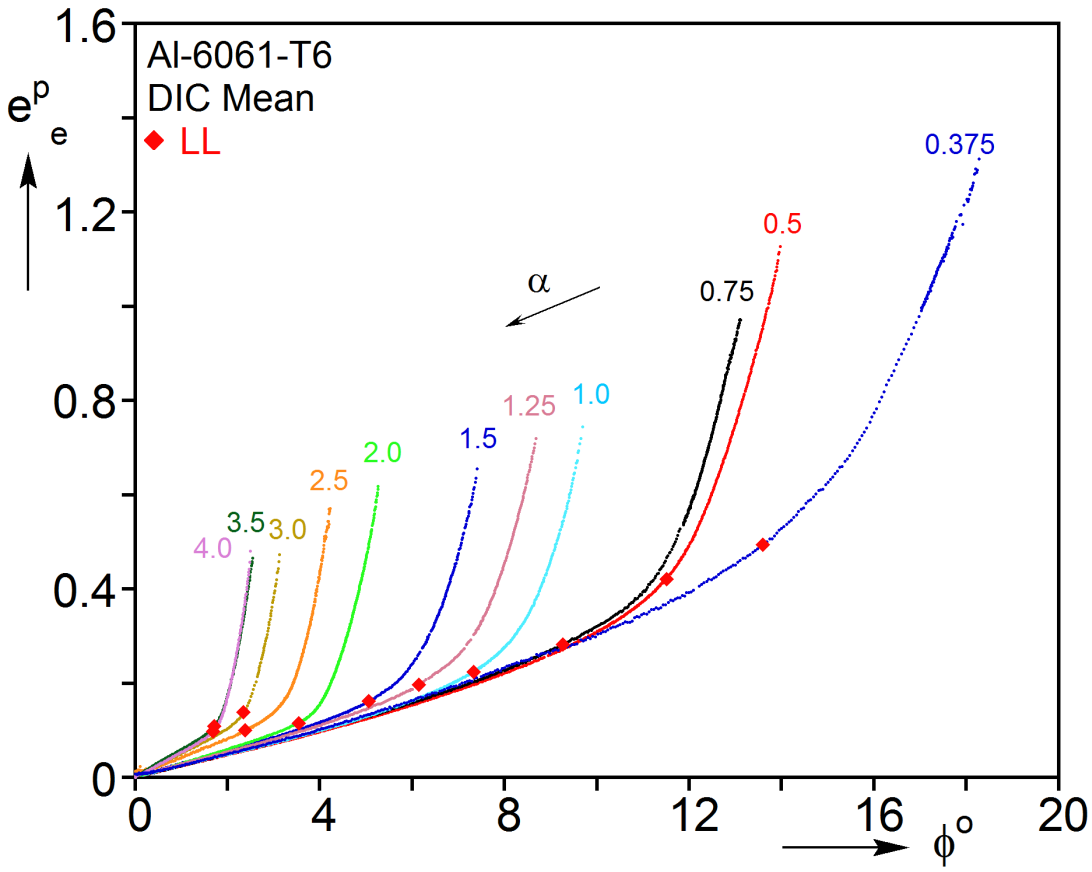

Fig. 3.11: Equivalent plastic strain vs. specimen rotation for eleven experiments.

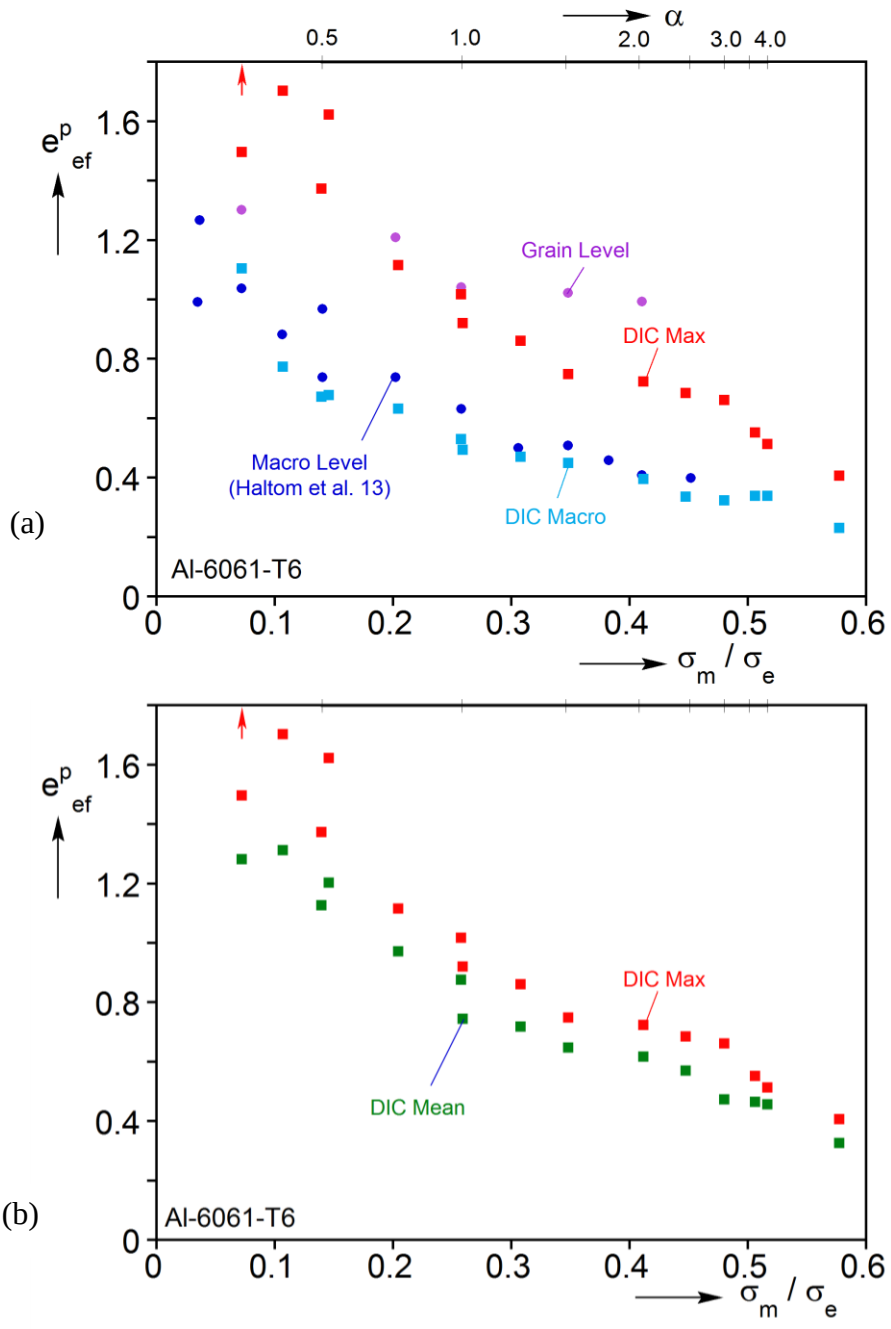

Fig. 3.12: (a) Measured equivalent plastic strain at failure vs. triaxiality (*DIC Max* and *DIC Macro*). The results of Haltom et al. [2013] are also included for comparison. (b) Comparison of Max and Mean failure strains recorded by DIC.

(a)

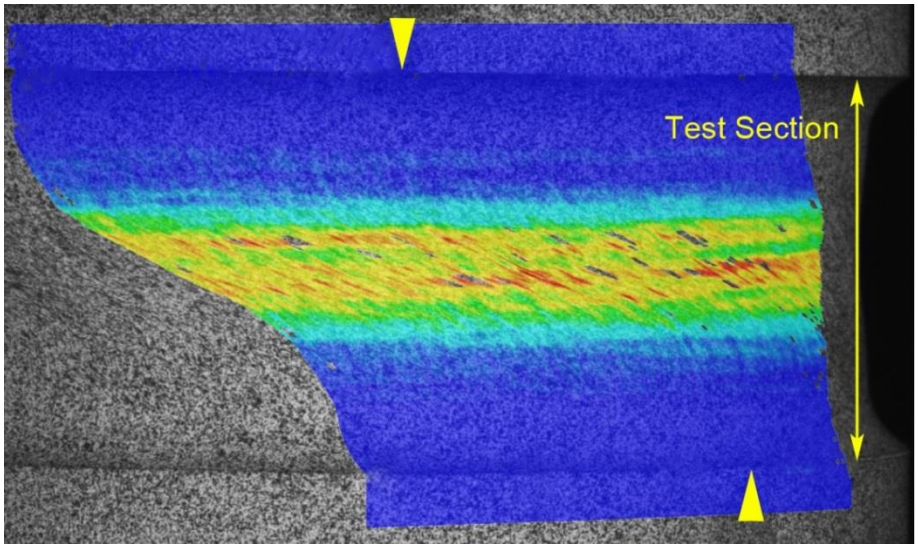

(b)

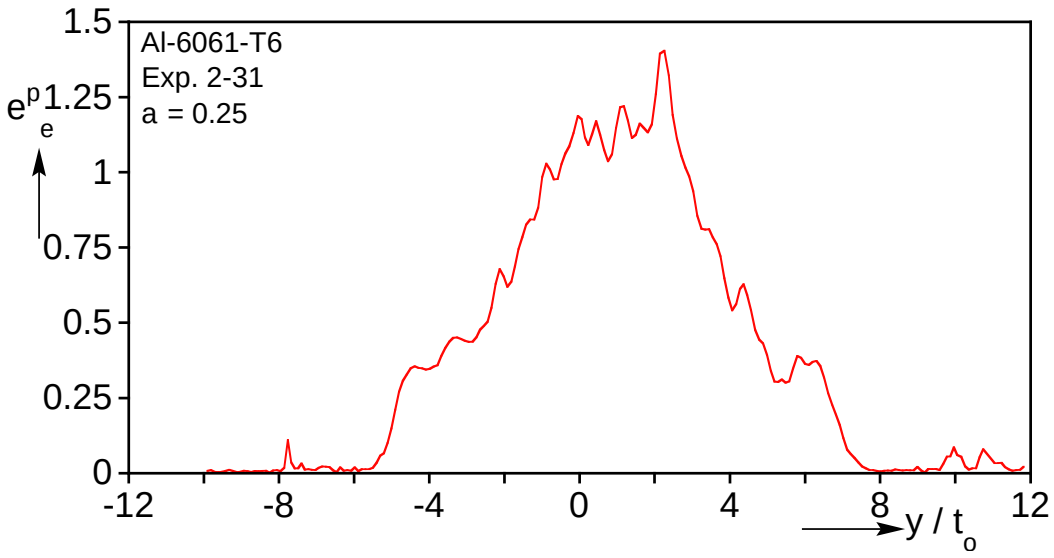

Fig. 3.13: Experiment 2-31, $\alpha = 0.25$: (a) DIC image and strain overlay just prior to failure. (b) Corresponding equivalent plastic strain profile passing through the maximum point. (Continues on next page)

(c)

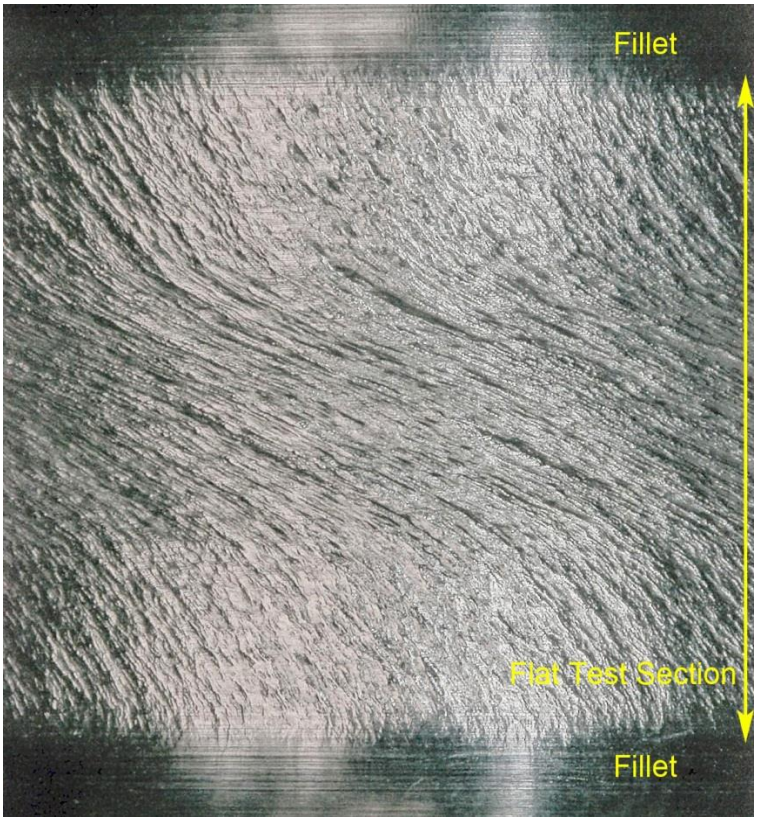

Fig. 3.13: (c) Image of the test section at the completion of the test exhibiting significant surface roughening.

(a)

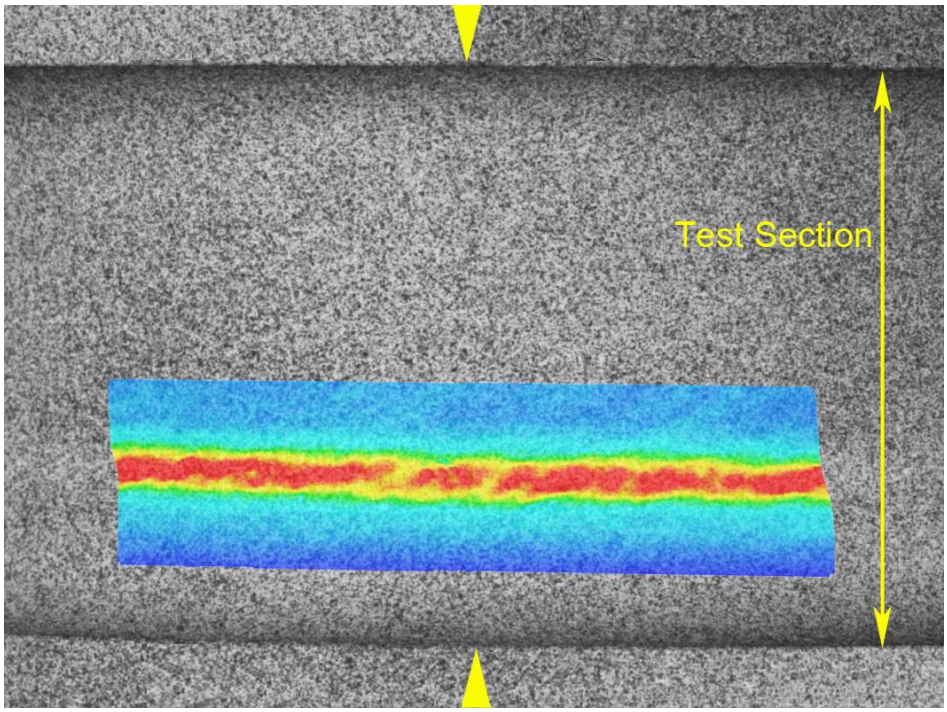

(b)

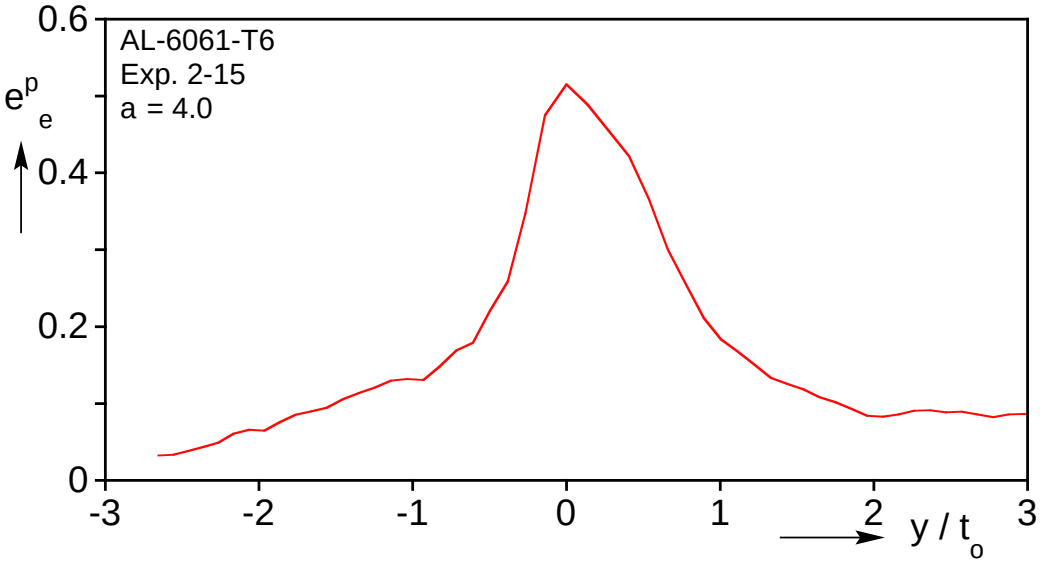

Fig. 3.14: Experiment 2-15, $\alpha = 4.0$. (a) DIC image and strain overlay just prior to failure. (b) Corresponding equivalent plastic strain profile passing through the maximum point.

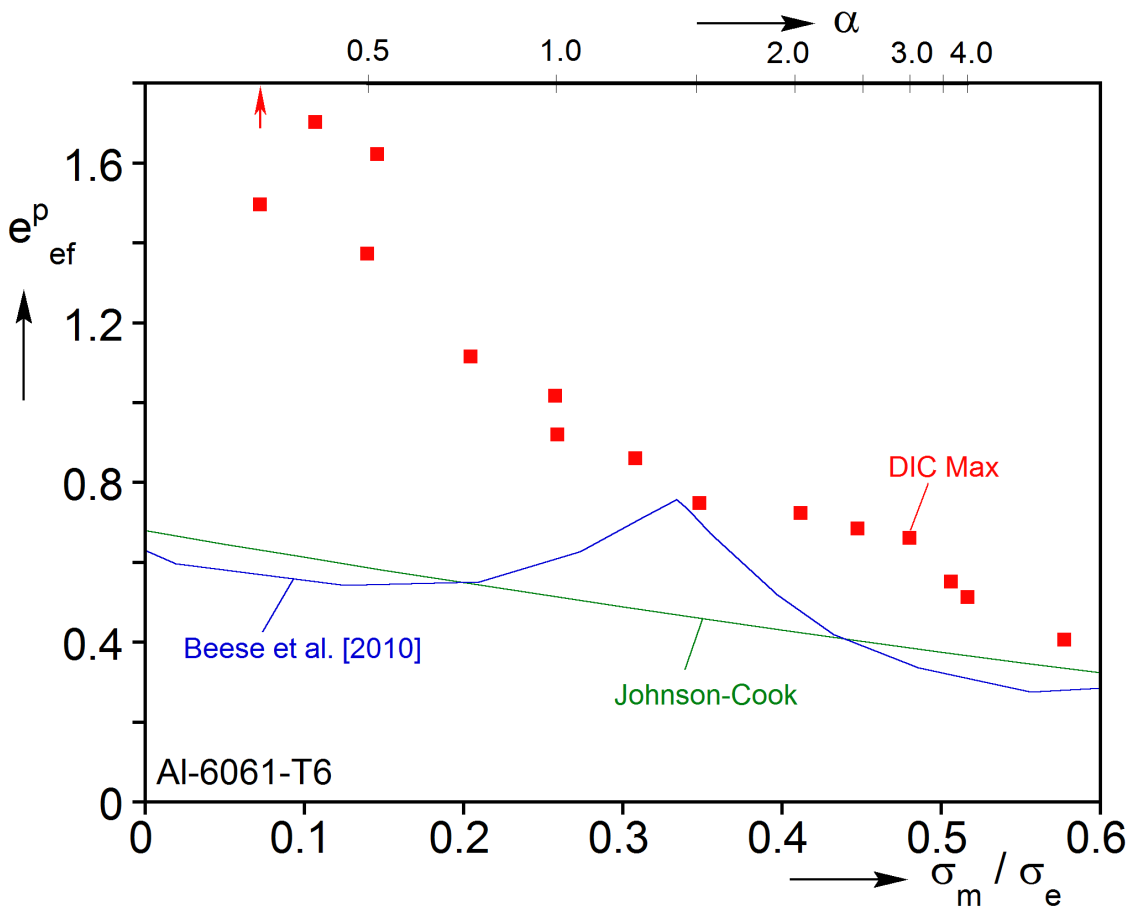

Fig. 3.15: Measured failure strain vs. triaxiality, along with grain-level values of Haltom et al. [2013] and predictions from Beese *et al.* [2010], and the Johnson and Cook model (Lesuer et al. [2001]).

Chapter 4: Tension-Torsion Experiments - Set II[2]

This chapter presents the results of a new set of combined tension and torsion (TT) experiments which employed different Al 6061-T6 tube stock. These experiments were conducted in support of a separate effort[3] to numerically simulate the TT experiments and reproduce the localized deformations[4]. As described in Chapter 3, microscopic and X-ray tomography evaluations of this alloy revealed that the highly deformed material remained essentially free of damage until very close to rupture. This numerical effort therefore seeks to establish how far plasticity alone can go in predicting the high strains that develop in the localized zone, and second demonstrate the effect of the yield function adopted on the results.

As part of this experimental series, the effect of load path on failure was studied through non-proportional "corner-path" experiments. Strains reported for this new series of experiments are calculated using the *Incremental* method described in Section 2.5.2, and different constitutive models are considered. Some prominent failure criteria are also calibrated to these experimental measurements.

The specimens in this set of experiments are machined from extruded Al 6061-T6 tubes manufactured by Kaiser Aluminum. Appendix A contains a discussion of the material microstructure. The tubes have a 2-inch nominal outer diameter (OD) and wall thickness of 0.188 inches (compared to 0.125 inches in the experiments of Chapter 3). The test specimens are nearly identical to those described in Chapter 3: a 0.4-inch long uniform test section with 0.0385-inch wall thickness. However the OD in the test section is reduced to 1.706 inches to account for the thicker-walled stock tube. Figure 4.1 shows a schematic of

[2] Scales, M., Chen, K., Kyriakides, S., (2019). Material response, localization, and failure of an aluminum alloy under combined shear and tension: Part I Experiments. *Int'l J. Plast*. [in press] (Performed experiments, post-processed data, and wrote the paper).
[3] National Science Foundation GOALI grant CMMI-1663269.
[4] Chen et al. [2019]

the new test specimens. Experiments are conducted with the same load frame and gripping hardware, and 3D DIC is again used to monitor deformations. The slight change in specimen geometry did not warrant any changes to the DIC camera setup.

4.1: SUMMARY OF RADIAL-PATH EXPERIMENTS

A set of seven radial path experiments with $0.5 \leq \alpha \leq 4.0$ were conducted on the new material. A pure tension experiment (plane strain tension ≡ PS) and pure torsion ($\alpha = 0$) were also performed. The tube geometries and key results are summarized in Tables 4.1 and 4.2.

Figure 4.2 (a) presents the nominal stress histories for this new series of experiments, and Fig. 4.2 (b) the strain histories (using von Mises equivalent stress). The nominal shear stress-rotation and axial stress-elongation responses are shown in Fig. 4.3, and *Mean* equivalent-strain vs. rotation is shown in Fig. 4.4. These results closely resemble those reported in Chapter 3: Every experiment reaches a limit load, and beyond this point the deformation localizes into a narrow zone with width the order of the wall thickness that spans the circumference of the tube. The new set of experiments bear another similarity with those previously reported in that for experiments for $\alpha < 3.0$ the specimen remained intact, whereas axial-stress dominant experiments separated into two pieces.

Also included in these figures is the response of a *pure-torsion* experiment ($\alpha = 0$), which was conducted for the purpose of extracting a material stress-strain curve. This simple shear experiment does not reach a load maximum or form a circumferential band of localized deformation like the others. The test is terminated after considerable rotation at the first signs of torsional buckling. It is important to recognize then that this experiment's e_e^p vs. ϕ response in Fig. 4.4 remains linear throughout and never turns sharply upwards because the material never localizes. This fact, coupled with the observation that most of

the deformation that the material undergoes prior to failure occurs after the onset of localization, also explains why its strain history in Fig. 4.2 (b) traces a much shorter path than the other experiments.

Figure 4.5 shows images of the failure surface for the $\alpha = 0.75$ experiment acquired in a scanning electron microscope. Even in this moderately shear-dominant stress state, the surface exhibits the usual dimples, indicative of the void growth and coalescence mechanisms typical of ductile failure. However, as reported in Ghahremaninezhed and Ravi-Chandar [2012, 2013] and Haltom et al. [2013], we expect that this effect was local to the failure surface and that the observed voids did not form until immediately prior to rupture. This conclusion is further supported by X-ray tomography performed on a similar specimen of the same alloy, which revealed very little porosity in the immediate vicinity of the failure zone (Section 3.2.1).

As described in Section 3.2.1, this tomography analysis used a voxel size of 2 μm, and voids smaller than this may have gone undetected. However Ghahremaninezhed and Ravi-Chandar [2012] reported second-phase particles in undeformed Al 6061-T6 sheet that ranged in size from 1 to 5 μm, and a sparse population of voids near failure of the same order. Furthermore, Shen et al. [2013], Morgeneyer et al. [2014], and Buljac et al. [2016] adopted a voxel size of 0.7 μm for their in-situ laminography analyses on Al 6061-T6 and Al 2198 sheet; these studies also reported minimal void growth until immediately prior to failure, and only in the immediately vicinity of the rupture. Finally, the ruptured voids present on the failure surface in Fig. 4.5 (b) range from 1 to 3 μm in diameter. In light of these other observations, we judge that the results of the X-ray tomography analysis are not compromised by the 2 μm voxel that was adopted.

4.2: CORNER-PATH EXPERIMENTS

Towards initiating an investigation into the path dependence of failure in the axial-shear stress space, two sets of experiments were conducted in which loading followed non-proportional corner paths. These corner-path experiments corresponded to radial path experiments with α = 1 and 2, and each set consisted of an experiment in which the specimen is preloaded in tension then loaded to failure in shear ($\Sigma \rightarrow \mathcal{T}$), and an experiment with a shear preload and then axial loading to failure ($\mathcal{T} \rightarrow \Sigma$). In $\Sigma \rightarrow \mathcal{T}$ experiments, the specimen is first loaded axially in displacement control up to the nominal axial stress at which failure occurred in the corresponding radial path experiment. When the specified load is reached, it is maintained by switching the controller into load control, and the specimen is subjected to torsional loading until failure with the machine in rotation control. In $\mathcal{T} \rightarrow \Sigma$ experiments, the opposite is done: The specimen is torqued up to the nominal shear stress at which the corresponding radial path experiment failed, from which point the material is loaded axially to failure while the torque is maintained. This corner-path loading is depicted in the stress-space responses of both sets of experiments as shown in Fig. 4.6.

The corner-path experiments exhibit much of the same behavior as the radial path experiments. As shown in the stress-elongation/rotation responses of Fig. 4.7 and 4.8, the deformation remains elastic during the preloading phase except in the $\mathcal{T} \rightarrow \Sigma$, $\alpha = 1$ experiment, which underwent a small amount of plastic deformation during shear loading. Following the change into the second mode of loading, the responses all exhibit a hardening phase and reach a limit load, which is followed by failure. Just like the radial-path experiments, the deformation in the corner paths localizes into a narrow circumferential band of width order t_o in which failure initiates.

The radial and corner-path experiments within each set fail at strikingly similar stress states (marked by ▲ in Fig. 4.6). Both $\mathcal{T} \rightarrow \Sigma$ experiments (plotted in orange) reach

markedly greater axial stresses at their limit loads (marked by ♦) than the corresponding radial path experiments, and the $\Sigma \rightarrow \mathcal{T}$ path for $\alpha = 2$ attained a greater maximum shear stress than its radial counterpart. However the $\Sigma \rightarrow \mathcal{T}$ path (plotted in blue) for $\alpha = 1$ reached a maximum shear stress that was nearly identical to that of the radial path experiment. These loads and other important experimental quantities are summarized in Table 4.1 and 4.2.

These differences in limit loads are in concert with the trends seen in the *Mean* axial-shear strain histories in Fig. 4.9. Since most of the deformation that the material accumulates prior to failure occurs after the limit load (see Fig. 4.4 and Fig. 4.2 (b)), the evolution of strain largely follows the stress state in the post-limit load regime. For example, the $\mathcal{T} \rightarrow \Sigma$, $\alpha = 1$ experiment reached an axial stress of 29.8 ksi (207.7 MPa) at the limit load, which is significantly greater than maximum axial stress of 23.1 ksi (161 MPa) reached under radial loading. Accordingly, its strain history is dominated by axial deformation compared to its counterparts. In contrast, the $\mathcal{T} \rightarrow \Sigma$ experiment reached essentially the same shear stress at the LL as its radial path counterpart, and accordingly their strain trajectories follow nearly the same path. The same relation between the limit loads and the trend in strain histories is seen for $\alpha = 2$. While these differences in strain history are noteworthy, they are actually quite mild when viewed in context with the full set of radial path experiments. All three of the $\alpha = 2$ experiments strain histories fall between those of the $\alpha = 1.5$ and $\alpha = 3.0$ radial paths. Similarly, all of the $\alpha = 1$ histories fall between those of $\alpha = 1.5$ and $\alpha = 0.75$.

4.3: CONSTITUTIVE MODELS

The integration of the strains requires the adoption of a constitutive model through Eq. 2.18. While the results presented so far have considered only von Mises plasticity

(≡ VM) by taking $k = 2$ in Eq. 2.7, two other constitutive models will be considered in the presentation of the failure strains. The first is Hosford's isotropic, non-quadratic yield function with $k = 8$ (≡ H8), which has been shown to be more appropriate for aluminum alloys (Logan and Hosford [1980]). The second is the non-quadratic, anisotropic constitutive model Yld2004-3D of Barlat et al. [2005]. The aforementioned parallel effort to simulate these TT experiments has used the data to calibrate this anisotropic constitutive model to this material (for details on the calibration see Chen et al. [2019]).

Adopting these different constitutive models changes several aspects of these experimental calculations: First, each introduces a different definition of σ_e, which from Eq. 2.18 affects the equivalent plastic strain increment de_e^p in a given stage. Second, from Eq. 2.8, the constant of proportionality β between the axial and hoop stress depends on the adopted constitutive model. For VM, β = 1/2 for all considered stress states. That is not the case for H8 and Yld04, however, in which β depends on α, the axial-to-shear stress ratio. The variation of β with α is shown in Fig. 4.10. Finally, the mean stress σ_m is directly affected by the difference in β, and in turn so is the equivalent stress (Eqs. 2.5-2.7)

4.4: DISCUSSION OF FAILURE STRAIN

The measured *Max* and *Mean* equivalent strains, e_{ef}^p and $\bar{e}_{ef}^p$, in the last image prior to failure in each experiment are plotted against the measured triaxiality, σ_{mf}/σ_{ef}, in Fig. 4.11 (a) using the von Mises measures of stress and strain. The numerical values are also listed in Table 4.2 together with the corresponding Lode parameters $\bar{\theta}_f$ and μ_f (see Eqs. 2.12 and 2.14). The two failure strain measures follow similar, monotonically decreasing trends as the triaxiality increases, with the *Max* values being consistently higher than the *Mean*. The maximum value of strain recorded was 1.596 at a triaxiality of 0.139 (α = 0.5), compared to 0.450 for the experiment with the highest triaxiality of 0.577 (plane-

strain tension experiment). Both the monotonic trends with triaxiality and the levels of the failure strains are in line with the values reported in Scales et al. [2016]. The trend does not exhibit a cusp in the vicinity of triaxiality of 0.33 reported in some investigations. The Lode parameter μ_f is plotted against the same triaxiality range in Fig. 4.11 (b). This parameter takes a value of 0 for simple shear, decreases down to -1 at triaxiality of about 0.33, and returns to 0 for plane strain tension. Included in the figure with solid bullets are the values of μ_f at failure in the experiments (see Table 4.2).

Figure 4.11 (a) also shows the *Mean* measures of failure strain for the $\mathcal{T}\rightarrow\Sigma$ and $\Sigma\rightarrow\mathcal{T}$ corner paths corresponding to the radial paths with $\alpha = 1.0$ and 2.0. The corner path failure strains are generally comparable to their radial path counterparts. This similarity can be attributed to the fact that most of strain to failure accumulated following the limit load, a time when the stress state is not changing substantially. The corresponding differences between the *Max* measures of failure strain in Table 4.2 are somewhat larger but this could be caused by the larger variation typically exhibited by the *Max* data.

In order to include the effect of the material frame rotation resulting from shear deformations, all strains reported here were integrated over the history of the test (see Section 2.5). By contrast, Haltom et al. [2013] and Scales et al. [2016], motivated by the desire to report strains free of the influence of a constitutive model, reported the total strains measured just before the onset of failure. To assess the influence of material frame rotation on the results, the reported *Max* and *Mean* failure strains are compared to the total measures in Fig. 4.12. As expected, the difference between the two measures is very small for the tension-dominant larger values of α, become noticeable for α of 1.0 and 0.75 while for the shear-dominant case of α = 0.5 the *Mean* and *Max* total measures are respectively 14.5% and 11% lower than the integrated measure.

The effect of the adopted constitutive model on the *Mean* measure of failure strain is demonstrated in Fig. 4.13 where it is plotted against the triaxiality, with both variables based on the VM, H8, and Yld04 models. Note that σ_e used in the denominator of triaxiality corresponds to each constitutive model's definition of equivalent stress. The difference between the three failure stains is small across the whole range of triaxiality. The effect on the value of the triaxiality is more noticeable as it results in a horizontal spread between the data points of each experiment. It is driven by the change in β, which alters the mean stress and equivalent stress. The horizontal shift is more significant for the larger values of triaxiality such as $\alpha = 4.16$, where σ_{mf}/σ_{ef} drops from 0.520 for VM to 0.452 for H8, with the Yld04 value in between the two. In summary, the constitutive model plays a negligible role on the equivalent strain values, and the shifts in triaxiality are modest. As a result, the large failure strains and their monotonic relationship with triaxiality are maintained for all three constitutive models considered.

4.4.1: Uncertainty and Error in Measurements

Calculation of the stresses was enabled via a plane-stress assumption through the wall thickness and a plane-strain assumption circumferentially. As discussed in Chapters 2, 3, and 6, these assumptions are likely not completely valid, and will be further addressed in future numerical studies of these experiments (Chen et al. [2019]). Aside from these two assumptions, the fact that the tubular test specimens are mildly eccentric (3-5%) means that the stress state was not truly uniform around the circumference of the tube. However, we judge that eccentricity's effect on the stress state is not significant since the localization still developed completely around the circumference of the tube.

The reported failure strains have their own sources of uncertainty even though they were established directly from the DIC measurements. We observe only approximately

one-third of the outer surface of the specimen. Though it is reasonable to assume that the strain does not vary significantly through the thin-walled test section, the measured surface strains may not represent exactly the strains elsewhere through the thickness. Local geometric features and imperfections, which are known to influence the development of localization, may also disrupt the local strain field. Finally, our measurements show that the strain grows quite rapidly immediately prior to failure, yet we acquire DIC images every two seconds in our experiments. As a result, our measurements may miss this period of rapid growth and underestimate the actual failure strain.

Figure 4.14 shows the *Mean* and *Max* failure strains, calculated using the *Incremental Method*. Included in the figure are error bars representing one standard deviation above and below the *Mean* value (recall from Chapter 2 that the *Mean* is computed as the average strain at failure for all column maxima). The standard deviations are consistent across all experiments, coming in at less than 0.07 in all cases except the shear-dominant $\alpha = 0.5$ experiment where it was 0.11. The consistency of deviation speaks to the care that was taken during setup of the DIC hardware and application of the speckle pattern. As seen in the figure, the reported *Max* value lies well outside the 1-σ band in most cases (it is typically about 2σ greater than the *Mean*). This difference between the *Max* and *Mean* values reinforces the fact that the deformations are highly localized, and that local geometric features can influence the local stress and strain state.

Finally, recall in the dataset reported in Chapter 3 that experiments were repeated for both $\alpha = 0.5$ and 1.0. The difference in measured *Mean* and *Max* failure strains in those two experiments is of the same order of the standard deviations measured here. Thus we conclude that natural variability from specimen to specimen is as significant as any of the aforementioned sources of uncertainty and error in our measurements.

4.4.2: Calibration of Common Failure Criteria to the Measured Failure Strains

(a) Johnson-Cook

The failure criterion of Johnson and Cook [1985] is perhaps the most well-known in existence. In a quasi-static, room-temperature setting, the equivalent plastic strain at failure depends only upon the stress triaxiality:

$$e_e^p = D_1 + D_2 \exp[D_3 \frac{\sigma_{mf}}{\sigma_{ef}}] \tag{4.1}$$

This model is easily fit to our data via least squares minimization. The model optimized to our *Mean* failure strains using the von Mises equivalent stress is shown in Fig. 4.15, and the model parameters for this are shown in Table 4.3. The model follows the trend of our experimental data very well, though this is unsurprising: The exponential form of the Johnson-Cook model naturally fits well with the monotonic relationship between failure strain and triaxiality that we measured.

It should be noted that even though this model fit our data well, it gives suspect predictions for triaxialities beyond the range of our study. Johnson and Cook stated that their model is appropriate for $\sigma_m/\sigma_e < 1.5$, yet the parameters we have identified suggest a failure strain of just 1.4% at a triaxiality of 1.5. Such a low value seems unrealistic and highlights the dangers of using phenomenological models to extrapolate beyond experimental measurements.

(b) Hosford-Coulomb

A potential shortcoming of the Johnson-Cook failure model is its simplicity. Specifically, it relates failure strain only to the triaxiality. It is now widely accepted however that J_3, the third-invariant of the deviatoric stress tensor, also contributes to ductile failure. A number of failure models developed in the recent past attempt to incorporate the

effect of J_3. Some of these models take a micromechanical approach and attempt to connect macroscopic localization to microscopic void growth, such as the model of as Nahshon and Hutchinson [2008], who extended the Gurson model with a J_3-type parameter. Others on the other hand have developed phenomenological models.

One such model is the so-called Hosford-Coulomb (HC) failure model, which was first proposed in Mohr and Marcadet [2015]. This approach is an adaptation of the modified Mohr-Coulomb (MC) localization criterion (Bai and Wierzbicki [2008]), which predicts failure to occur when the shear and normal stresses on any given material plane reaches a critical value:

$$\max_n \{\tau + c_1\sigma_n\} = c_2 \tag{4.2}$$

This can be expressed in terms of the ordered principal stresses:

$$(\sigma_1 - \sigma_3) + c(\sigma_1 + \sigma_3) = \sigma_c \tag{4.3}$$

Note that (σ_1 -σ_3) is the Tresca equivalent stress. Mohr and Marcadet observed that this model struggled to accurately predict the onset of failure in shear-dominant stress states, and thus proposed replacing the Tresca equivalent stress with the Hosford equivalent stress:

$$\sigma_H + c(\sigma_1 + \sigma_3) = \sigma_c, \text{ where} \tag{4.4}$$

$$\sigma_H = \left\{\frac{1}{2}((\sigma_1 - \sigma_2)^a + (\sigma_2 - \sigma_3)^a + (\sigma_3 - \sigma_1)^a)\right\}^{1/a} \tag{4.5}$$

In this way, the model postulates that failure occurs when the equivalent stress and normal stresses reach a critical value, and the parameters $\{a, c, \sigma_c\}$ then are those which must be identified. This criterion can be equivalently posed as a function of Lode parameter and triaxiality. Finally, note that this model is a critical *stress* criterion, not a strain criterion. Given a material stress-strain relationship, the predicted failure stress can be mapped to a failure strain.

In our work, the equivalent plastic strain, triaxiality, and Lode parameter at failure are established directly from experimental measurements. The equivalent stress at failure is established from the measured equivalent plastic strain and the material stress-strain curves, which were extracted from the pure-torsion ($\alpha = 0$) experiment (Chen et al. [2019]). An error function is constructed that compares these failure stresses to those predicted by the model, and this error function is numerically minimized to obtain the parameters $\{a, c, \sigma_c\}$. The identified parameters are listed in Table 4.3, and the predicted failure locus for the model fitted to our VM data are shown in Fig. 4.15.

(c) Discussion

Both the Johnson-Cook and Hosford-Coulomb models follow our experimental measurements well. They both reproduce large strains at low triaxialities, moderate strains near plane-strain tension, and they predict a monotonic relationship with triaxiality. One distinct difference between the two is the modest "bump" seen in the HC prediction around a triaxiality of 0.3. This feature is brought about by the HC model's inclusion of the Lode parameter, which as plotted in Fig 4.11 (b), undergoes a slope discontinuity at this triaxiality. Indeed, it is this very change in behavior that gives rise to the oft-reported local maximum in failure strain at this same triaxiality.

Ultimately, both models have three independent parameters, which provide sufficient flexibility for them to be calibrated to our data set. The JC model is somewhat constrained by the fact that it includes an explicit exponential form, but that is perfectly suited for our monotonic relationship. The HC model has greater flexibility due to its lack of such a functional form and inclusion of J_3 dependence. Given the flexibility of these models, it is expected that they are both capable of representing the failure locus for a variety of materials (e.g., Papasidero et al. [2015], Ha et al. [2018]). However, in all cases,

the great challenge still remains obtaining reliable experimental data to which they can be calibrated.

4.5: SUMMARY AND CONCLUSIONS

A new set of combined tension and torsion experiments on a different Al 6061-T6 tube stock was conducted in support of a separate effort to calibrate an anisotropic constitutive model and numerically simulate these experiments (Chen et al. [2019]). The setup and diagnostic methods are identical to those reported in Scales et al. [2016] and presented here in Chapter 2. Radial path experiments covering a range of triaxiality from 0.139 to 0.577 showed essentially the same behavior as those reported in Chapter 3 both qualitatively and quantitatively. Large localized deformations develop following a stress maximum, and the strain in these zones grows rapidly as the material approaches failure. Once again, the measured failure strains decrease monotonically as triaxiality increases.

The strains in this work were computed incrementally from the instantaneous strain rate tensor and integrated so as to account for the material frame rotation in the test section. This procedure is different to the previous work in which strains were computed in total directly from the stretch tensor. It was shown in this Chapter that the difference in calculated failure strains for the two methods is negligible for triaxialities above 0.26 ($\alpha = 1$) when there is very little material frame rotation, while the two methods differ by 10 to 14% in the most shear-dominant stress states. This incremental method of calculation required the adoption of a constitutive model, yet for the three constitutive models considered here, the effect on the calculated failure strain was minor.

To directly compare the failure strains presented in Chapter 3 (≡ 2016) with those presented in this chapter (≡ 2018), the 2016 results were recalculated incrementally. The *Mean* failure strains from the two series of experiments are plotted together against

triaxiality in Fig. 4.16. The two data sets are substantially similar, which proves the robustness of this experimental setup and data analysis.

Two sets of non-proportional corner-path experiments corresponding to $\alpha = 1$ and $\alpha = 2$ were conducted. Each set consisted of an experiment in which the specimen was preloaded in tension then loaded to failure in shear ($\Sigma \rightarrow \mathcal{T}$), and an experiment with a shear preload and then axial loading to failure ($\mathcal{T} \rightarrow \Sigma$). The experiments reached a stress maximum during the second loading phase, and the values of these maxima typically exceed the corresponding level reached in the radial path experiment. Despite this, the stress states at failure for all three tests within a set were remarkably similar. Furthermore, the equivalent plastic strains at failure did not differ substantially. This suggests a relative insensitivity of the failure strain to the stress path, at least in the stress regime examined in this study.

Table 4.1: Nominal geometries and limit-load measurements.

Exp. No.	Tube No.	α	R_o in (mm)	t_o in (mm)	Ξ_o %	Σ_{max} ksi (MPa)	$\mathcal{T}_{max}$ ksi (MPa)	ε_{xxL}	$\varepsilon_{\theta xL}$
11	3	0	0.837 (21.3)	0.0461 (1.17)	3.9	0	26.8 (185)	0	0.157
4	1	0.49	0.833 (21.2)	0.0392 (1.00)	4.2	13.0 (89.7)	26.2 (181)	0.060	0.451
10	3	0.75	0.834 (21.2)	0.0392 (1.000)	5.4	19.1 (132)	25.3 (174)	0.079	0.360
2	1	1.0	0.834 (21.2)	0.0386 (0.098)	3.6	24.4 (168)	24.1 (166)	0.067	0.209
1	1	1.5	0.834 (21.2)	0.0394 (1.00)	5.1	31.9 (220)	21.4 (147)	0.058	0.100
3	1	1.99	0.834 (21.2)	0.0390 (0.99)	4.8	36.5 (252)	18.2 (126)	0.077	0.081
5	1	3.0	0.834 (21.2)	0.0387 (0.98)	3.1	41.6 (287)	13.5 (93.1)	0.075	0.041
7	1	4.16	0.833 (21.2)	0.0388 (0.99)	3.5	43.4 (300)	10.4 (71.7)	0.084	0.036
9	2	PS	0.833 (21.2)	0.0389 (0.99)	5.8	46.9 (323)	0	0.106	0

Table 4.1 (cont'd): Nominal geometries and limit-load measurements.

Exp. No.	Tube No.	α	R_o in (mm)	t_o in (mm)	Ξ_o %	Σ_{max} ksi (MPa)	$\mathcal{T}_{max}$ ksi (MPa)	ε_{xxL}	$\varepsilon_{\theta xL}$
14	3	2.0 $\Sigma \rightarrow \mathcal{T}$	0.834 (21.2)	0.0390 (0.99)	5.2	32.0 (221)	21.0 (145)	0.070	0.097
17	2	2.0 $\mathcal{T} \rightarrow \Sigma$	0.834 (21.2)	0.0388 (0.99)	3.0	39.9 (275)	16.0 (110)	0.096	0.070
12	3	1.0 $\Sigma \rightarrow \mathcal{T}$	0.833 (21.2)	0.0390 (0.99)	4.8	23.1 (159)	23.9 (165)	0.074	0.224
13	3	1.0 $\mathcal{T} \rightarrow \Sigma$	0.834 (21.2)	0.0389 (0.99)	4.2	29.8 (205)	22.8 (157)	0.060	0.167

$$\Sigma = \alpha \mathcal{T}, \quad \Xi_o = \frac{t_{max} - t_{min}}{t_{max} + t_{min}}$$

Table 4.2: Measurements at failure

Exp. No.	α	Σ_f ksi (MPa)	$\mathcal{T}_f$ ksi (MPa)	σ_{xxf} ksi (MPa)	$\sigma_{\theta xf}$ ksi (MPa)	σ_{mf} / σ_{ef}	$\overline{\theta_f}$	μ_f	$\overline{e}^p_{ef}$	e^p_{ef}
11*	0	0	29.4 (203)	0	29.7 (205)	0	0	0	-	-
4	0.49	12.3 (84.8)	24.9 (172)	13.6 (93.8)	27.4 (189)	0.139	0.401	-0.369	1.382	1.596
10	0.75	18.3 (126)	24.1 (166)	21.4 (147)	28.2 (194)	0.204	0.595	-0.558	1.000	1.149
2	1.0	23.1 (159)	22.8 (157)	28.6 (197)	28.2 (195)	0.261	0.768	-0.736	0.959	1.135
1	1.5	27.2 (187)	18.2 (126)	36.9 (254)	24.7 (170)	0.345	0.960	-0.952	0.777	0.876
3	1.99	32.0 (221)	16.0 (110)	42.5 (293)	21.2 (146)	0.409	0.740	-0.707	0.533	0.619
5	3.0	34.9 (241)	11.2 (77.2)	46.7 (322)	15.0 (104)	0.486	0.441	-0.408	0.385	0.503
7	4.16	39.8 (275)	9.6 (66.2)	53.2 (367)	12.8 (88.2)	0.520	0.290	-0.265	0.367	0.556
9	PS	45.0 (310)	0	57.6 (397)	0	0.577	0	0	0.315	0.450

Table 4.2 (cont'd): Measurements at failure

Exp. No.	α	Σ_f ksi (MPa)	$\mathcal{T}_f$ ksi (MPa)	σ_{xxf} ksi (MPa)	$\sigma_{\theta xf}$ ksi (MPa)	$\sigma_{mf}/\ \sigma_{ef}$	$\overline{\theta_f}$	μ_f	$\overline{e}^p_{ef}$	e^p_{ef}
14	2.0 $\Sigma\rightarrow\mathcal{T}$	32.1 (221)	16.9 (116)	44.4 (306)	23.4 (161)	0.397	0.780	-0.750	0.650	0.797
17	2.0 $\mathcal{T}\rightarrow\Sigma$	34.7 (239)	16.0 (110)	48.7 (336)	22.5 (155)	0.424	0.682	-0.646	0.493	0.593
12	1.0 $\Sigma\rightarrow\mathcal{T}$	23.1 (159)	21.7 (150)	28.5 (197)	26.9 (185)	0.270	0.798	-0.769	0.829	1.182
13	1.0 $\mathcal{T}\rightarrow\Sigma$	22.9 (158)	22.7 (157)	29.3 (202)	29.1 (200)	0.260	0.765	-0.733	0.824	0.948

* Under pure torque deformation did not localize and no failure was observed

Table 4.3: Identified parameters for the Johnson-Cook and Hosford-Coulomb Models

	D_1	D_2	D_3
JC	0.0	2.173	-3.366
	a	c	σ_c
HC	1.38	0.155	60.0

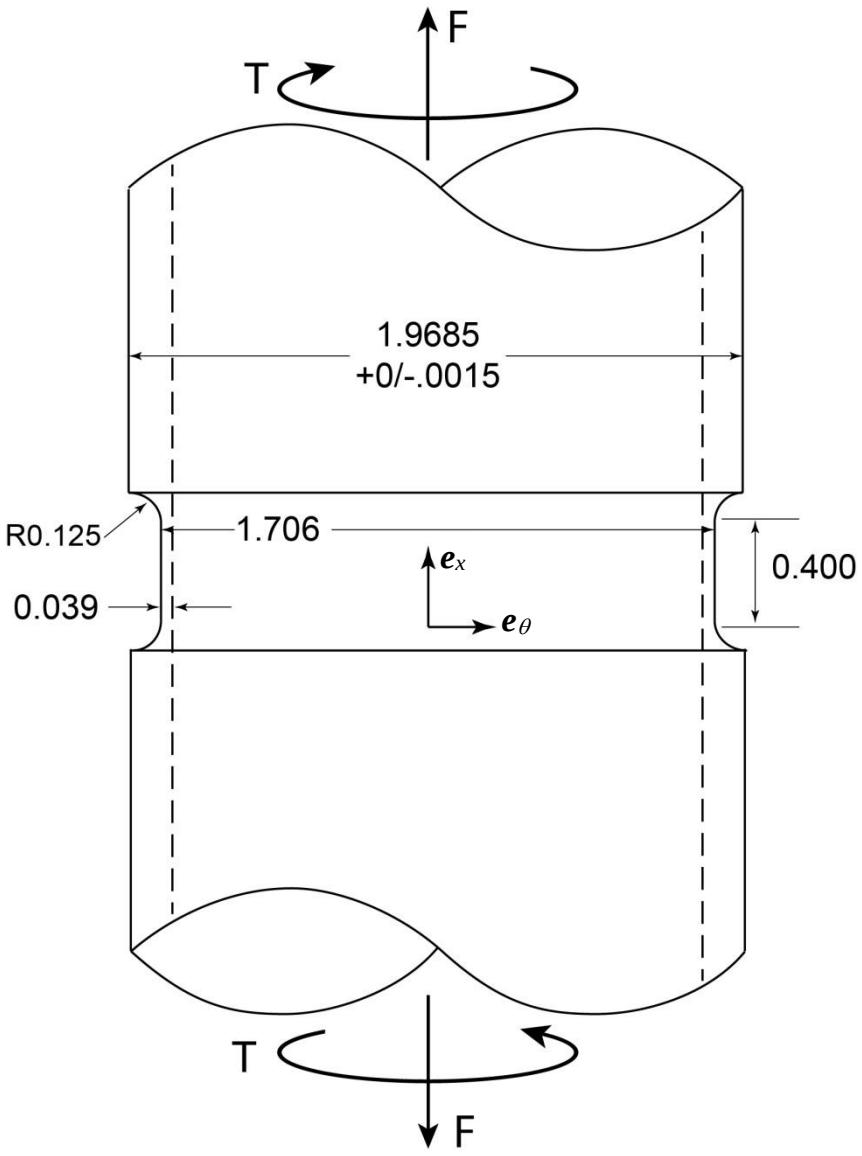

Fig. 4.1: Schematic of the machined tension-torsion specimen.

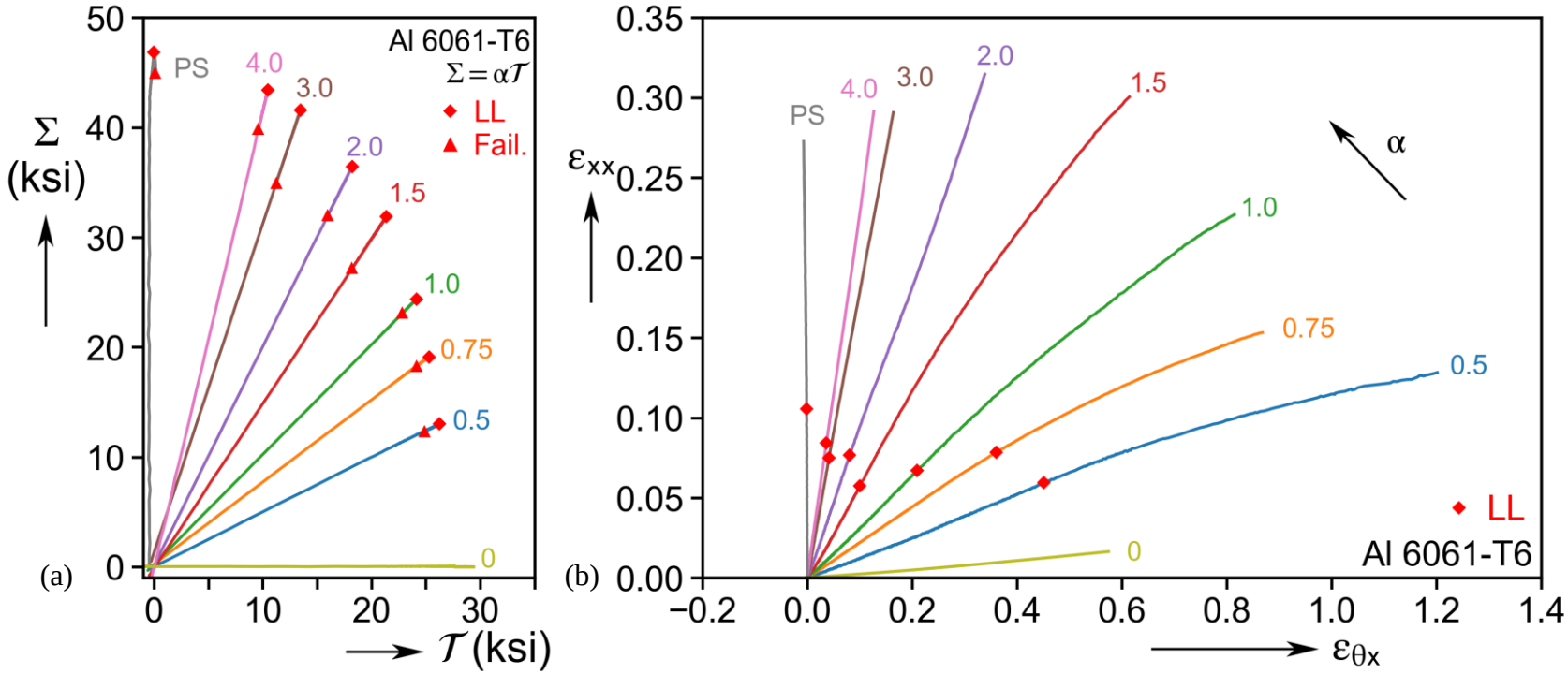

Fig. 4.2: (a) Nominal axial-shear stress histories for radial-path experiments. (b) Corresponding *Mean* strain histories. The limit load is marked by ◆, and the stresses at failure are marked by ▲ in (a).

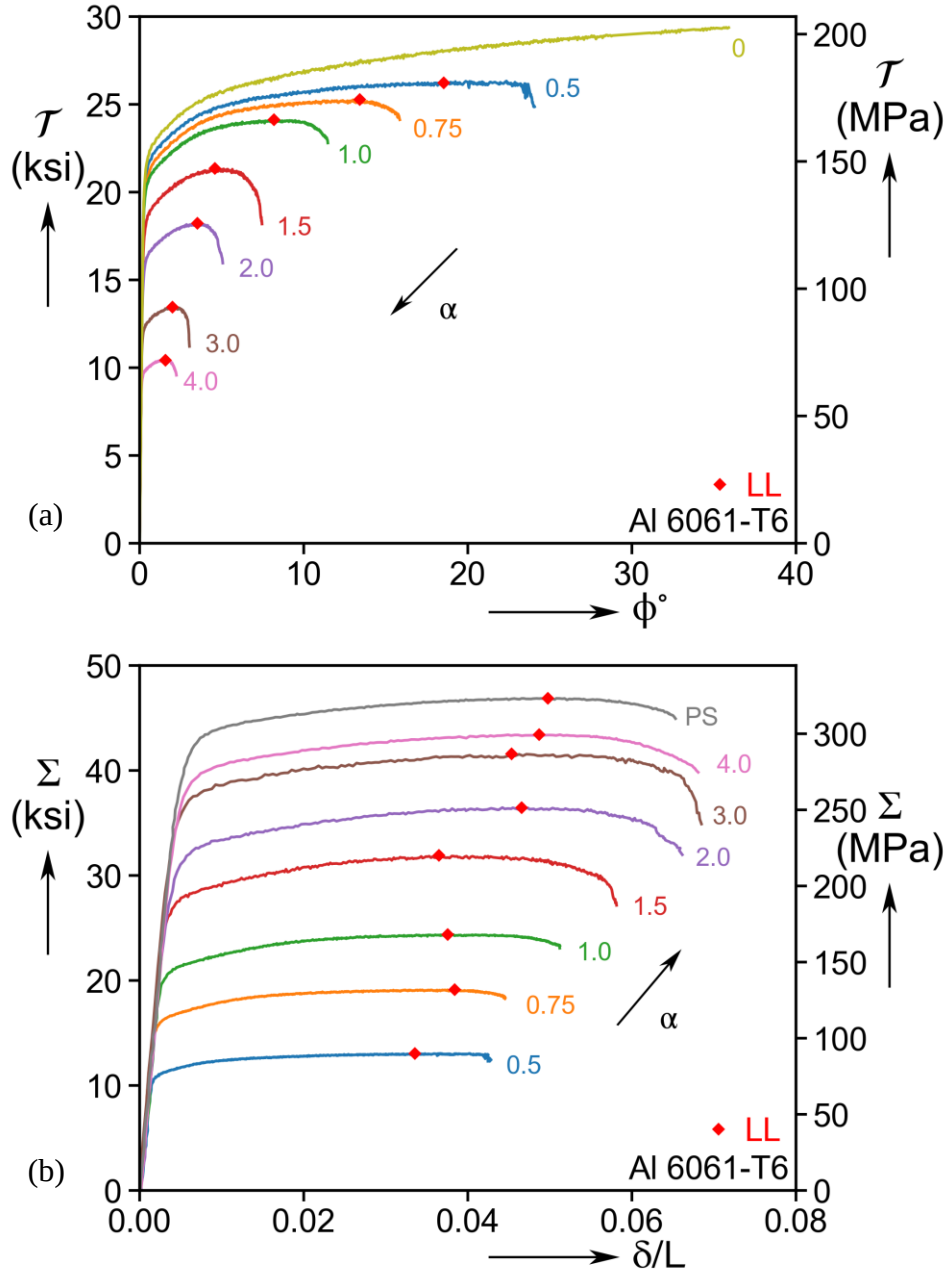

Fig. 4.3: (a) Nominal shear stress-rotation responses for radial-path experiments.
(b) Corresponding axial stress-normalized elongation responses.

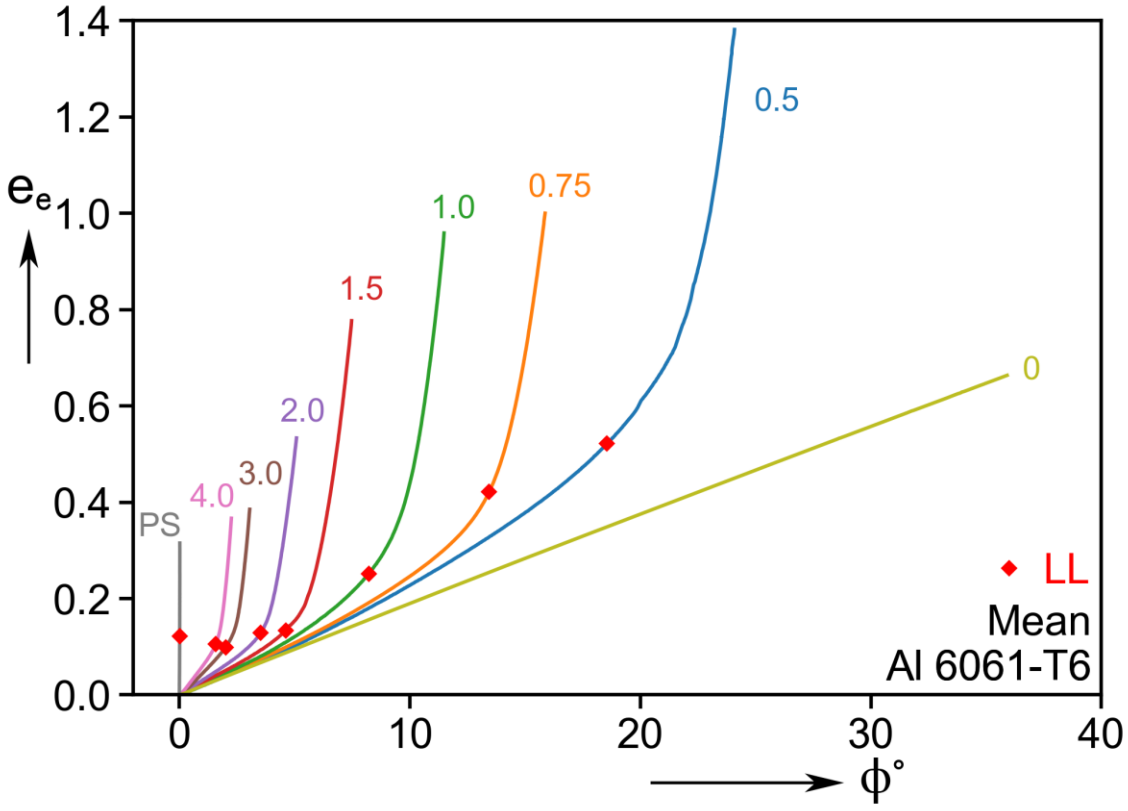

Fig. 4.4: *Mean* equivalent strain plotted against specimen rotation.

(a)

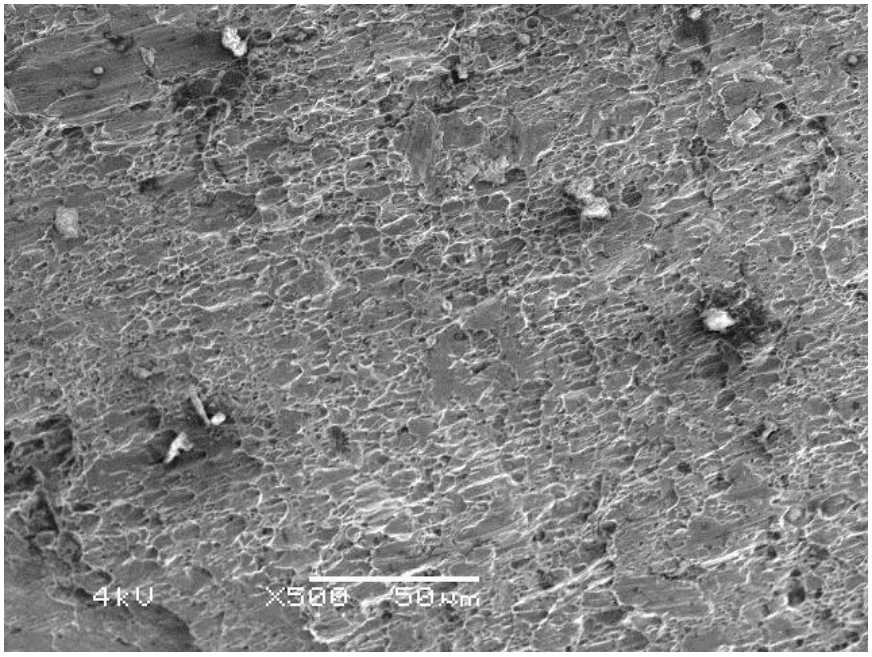

(b)

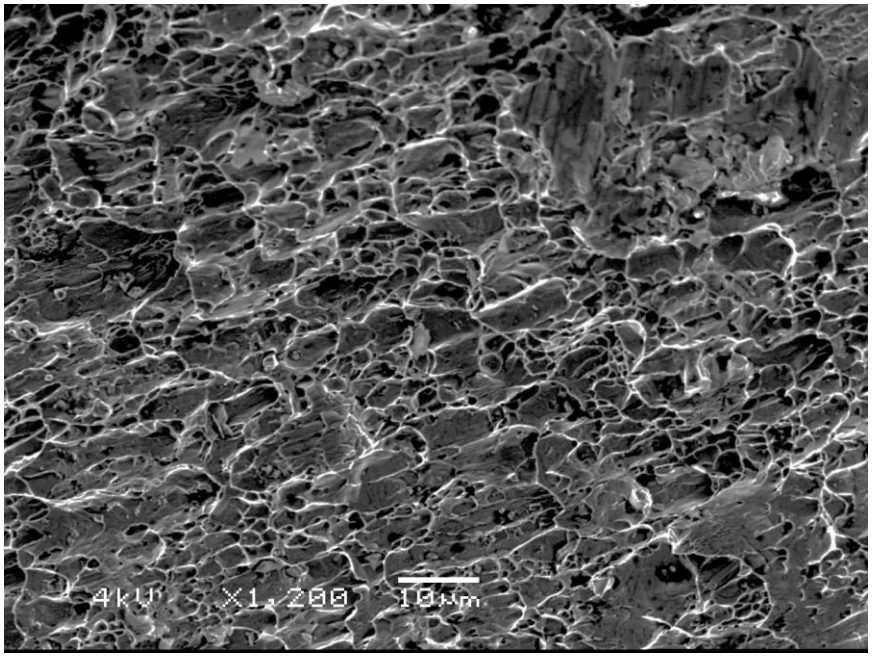

Fig. 4.5: Micrographs of the failure surface for Expt. 10 with α = 0.75 taken at 500x (a) and 1200x (b).

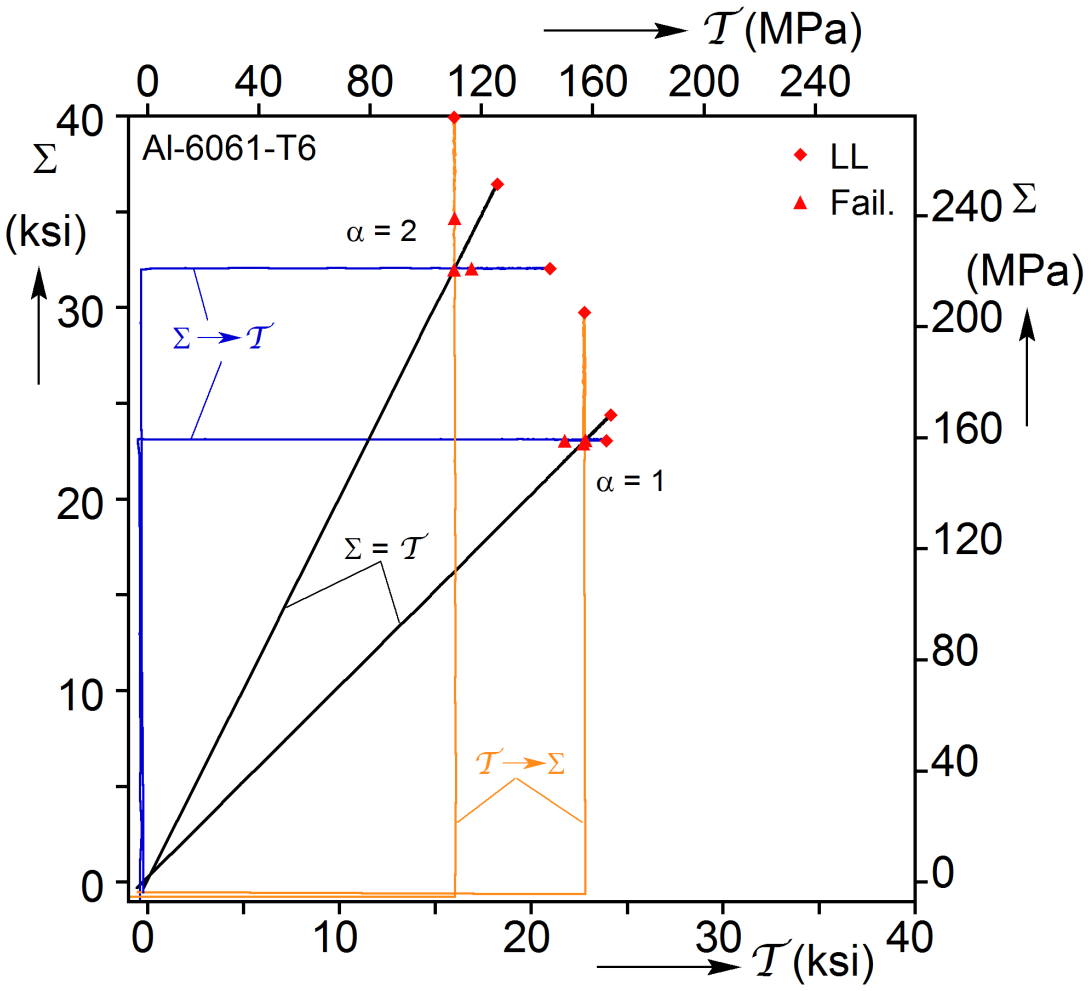

Fig. 4.6: Nominal axial-shear stress histories for the two sets of corner and corresponding radial-path experiments. The stress at the limit load and failure are marked by ◆ and ▲, respectively.

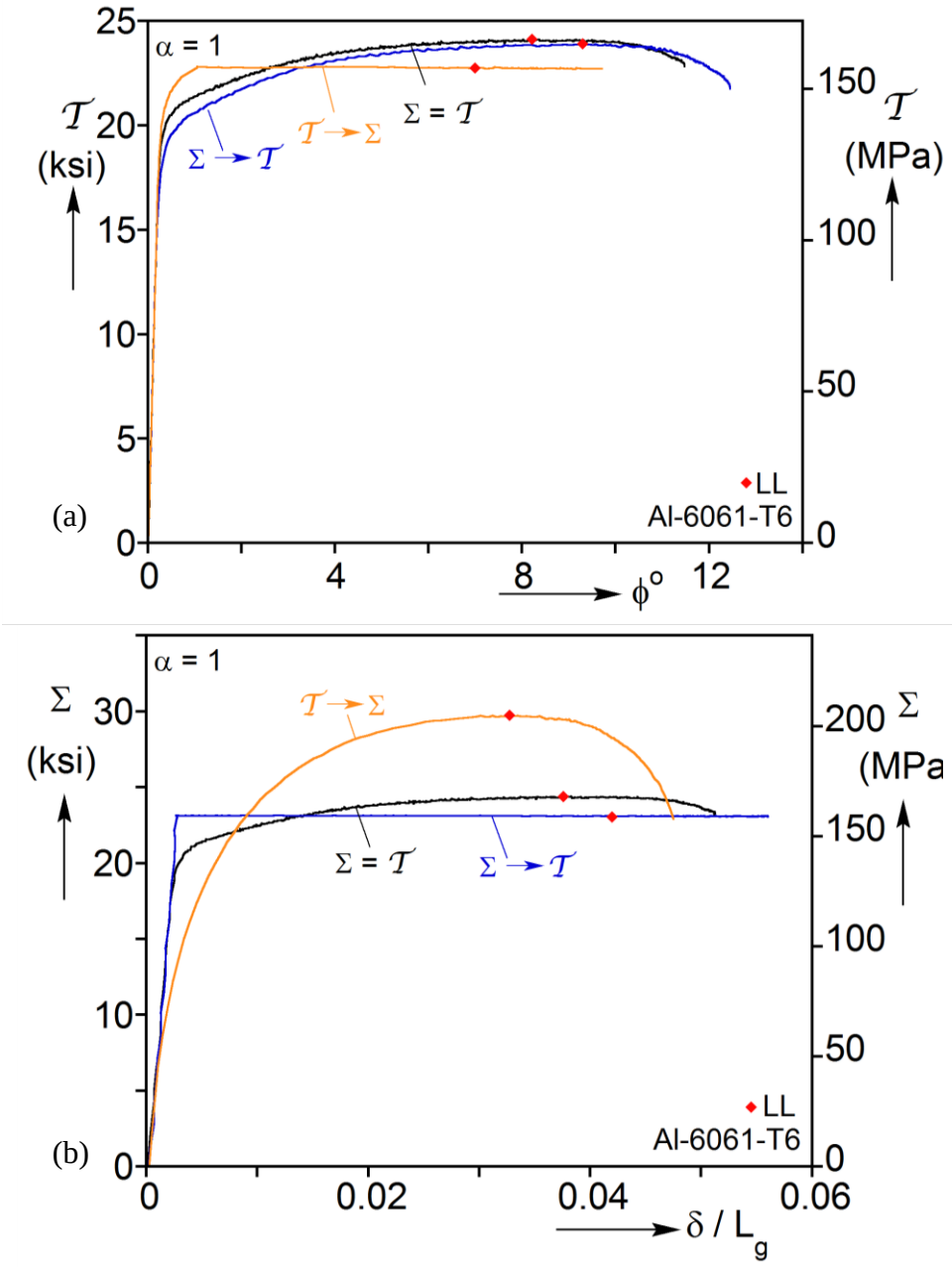

Fig. 4.7: (a) Nominal shear stress-rotation responses for corner- and radial-path experiments for $\alpha = 1$. (b) Corresponding axial stress-normalized elongation responses.

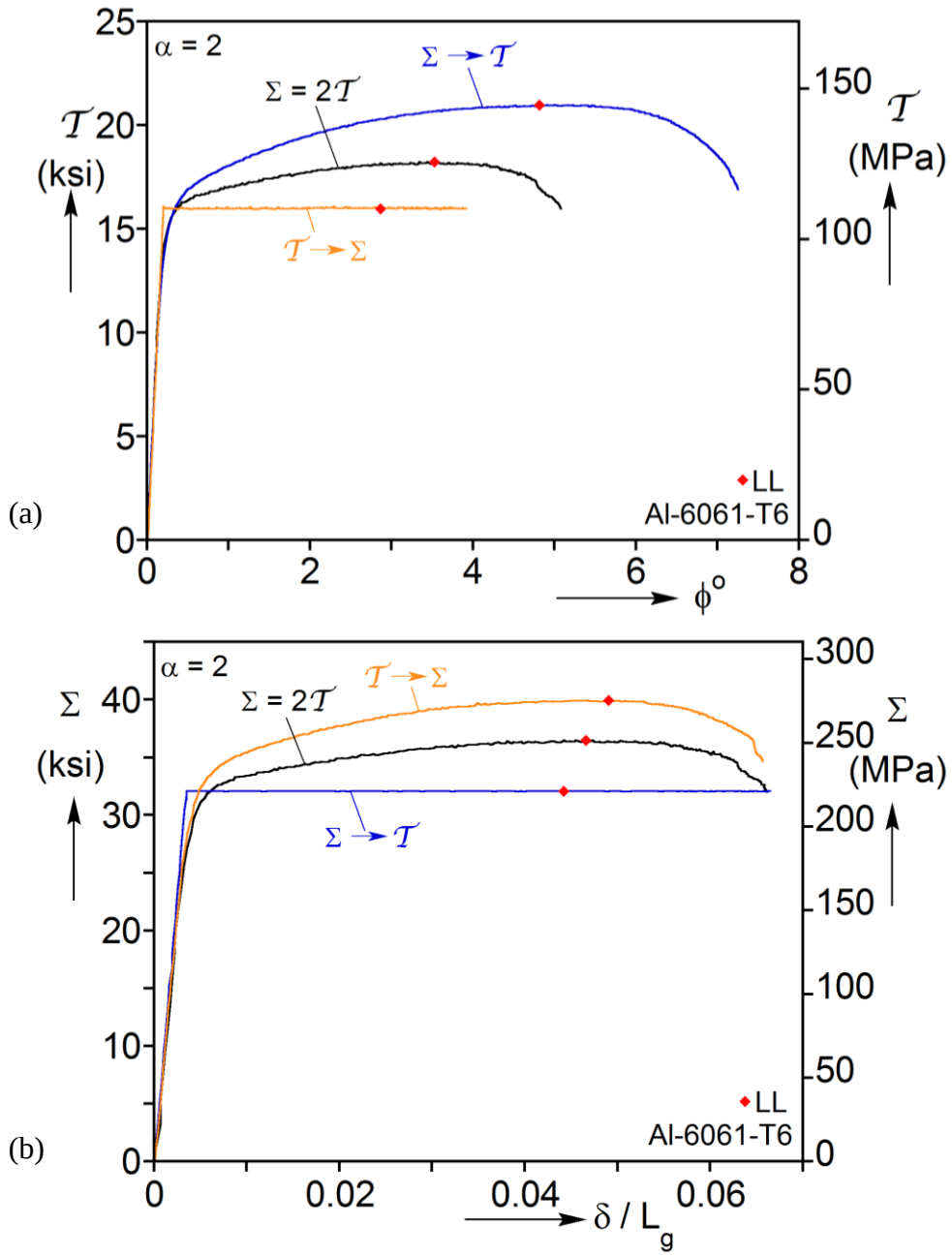

Fig. 4.8: (a) Nominal shear stress-rotation responses for corner- and radial-path experiments for $\alpha = 2$. (b) Corresponding axial stress-normalized elongation responses.

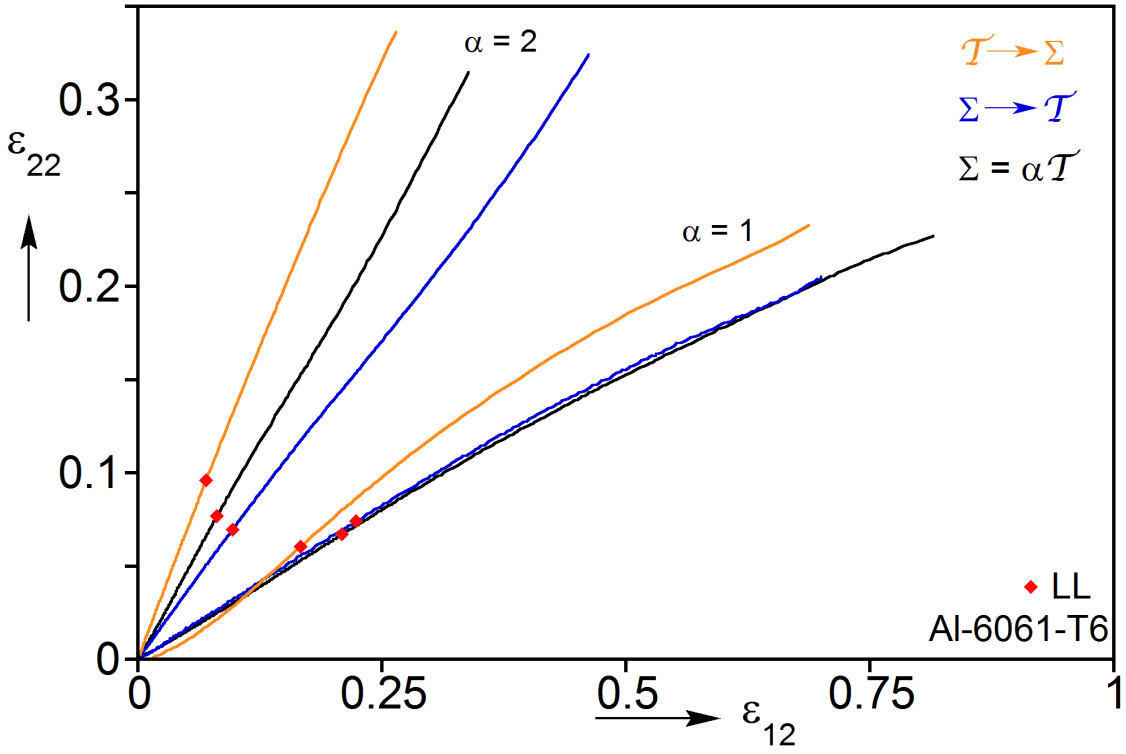

Fig. 4.9: *Mean* axial-shear strain histories for the two sets of corner- and radial-path experiments.

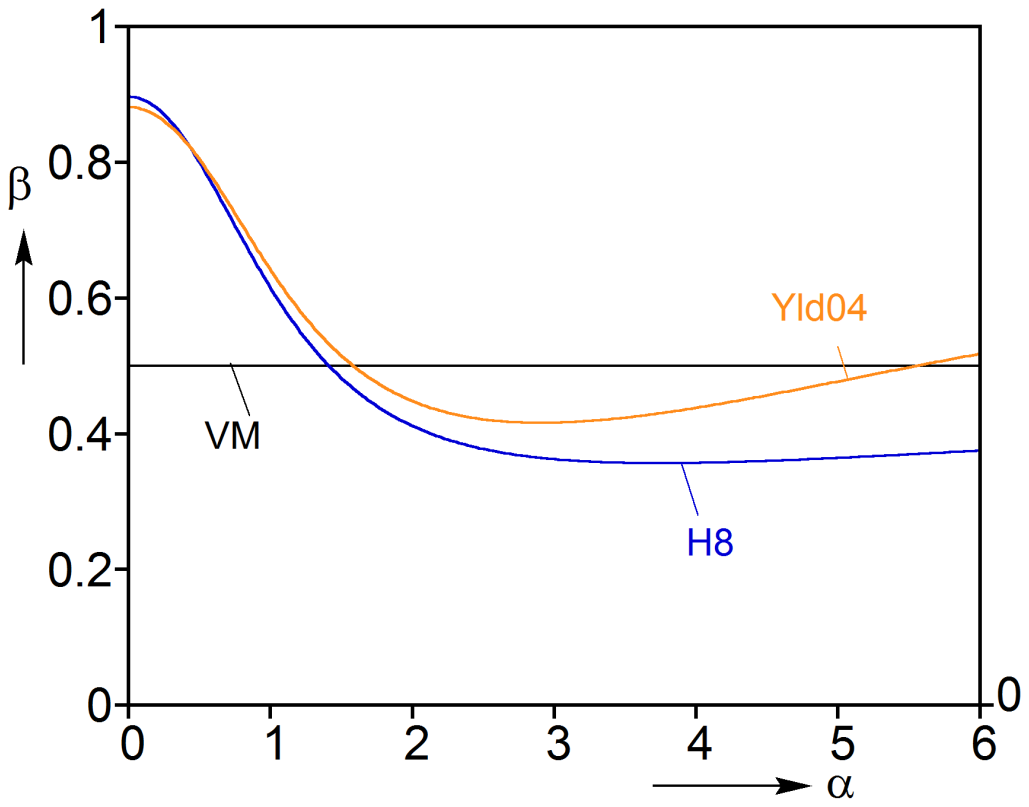

Fig. 4.10: Variation of β, the hoop-to-axial stress ratio, with α, the axial-to-shear stress ratio, for three constitutive models. β is calculated through the flow rule by assuming zero hoop strain.

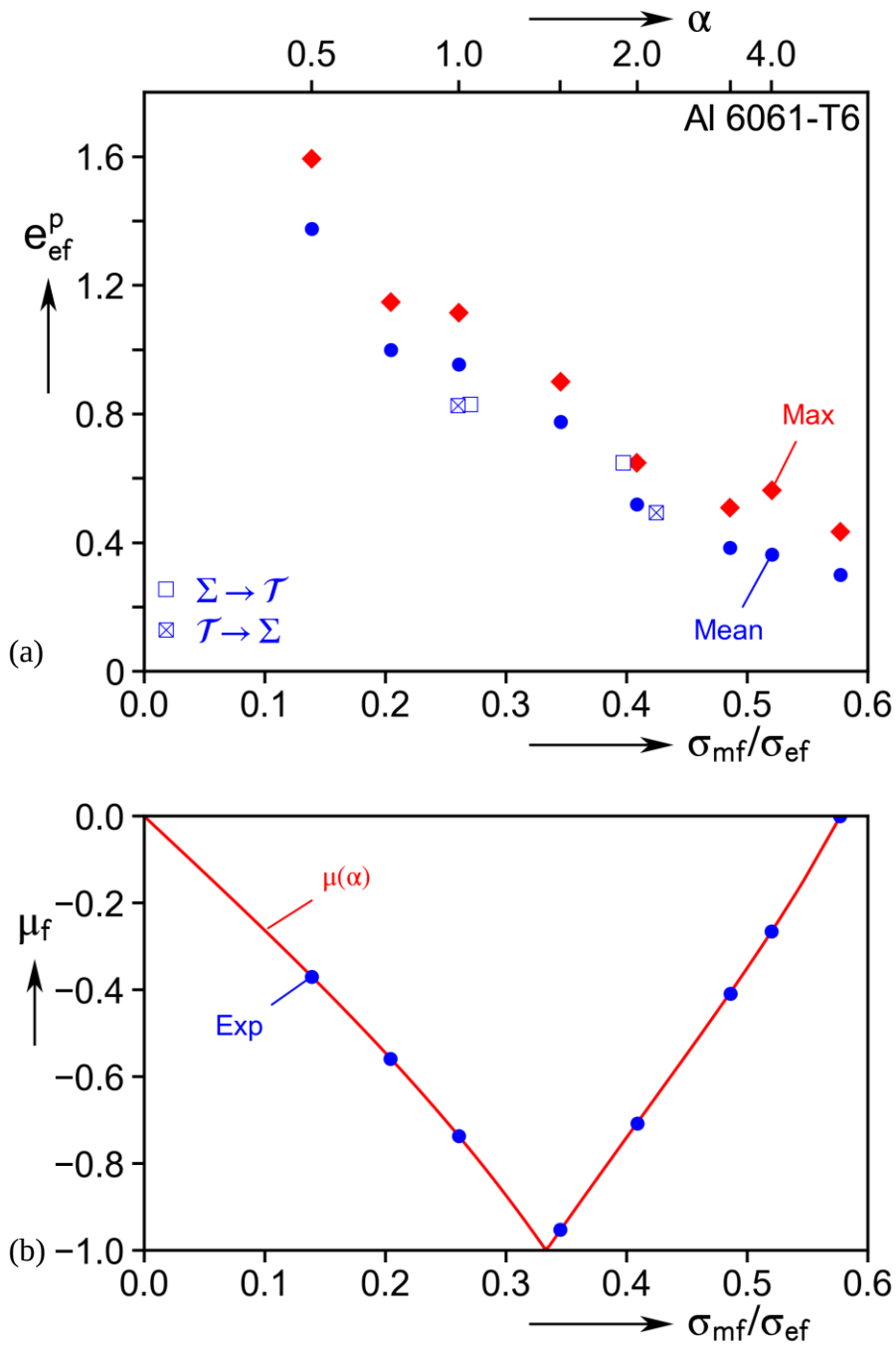

Fig. 4.11: (a) Measured *Mean* and *Max* equivalent strains at failure vs. triaxiality, assuming a von Mises constitutive model. (b) Lode parameter vs. α.

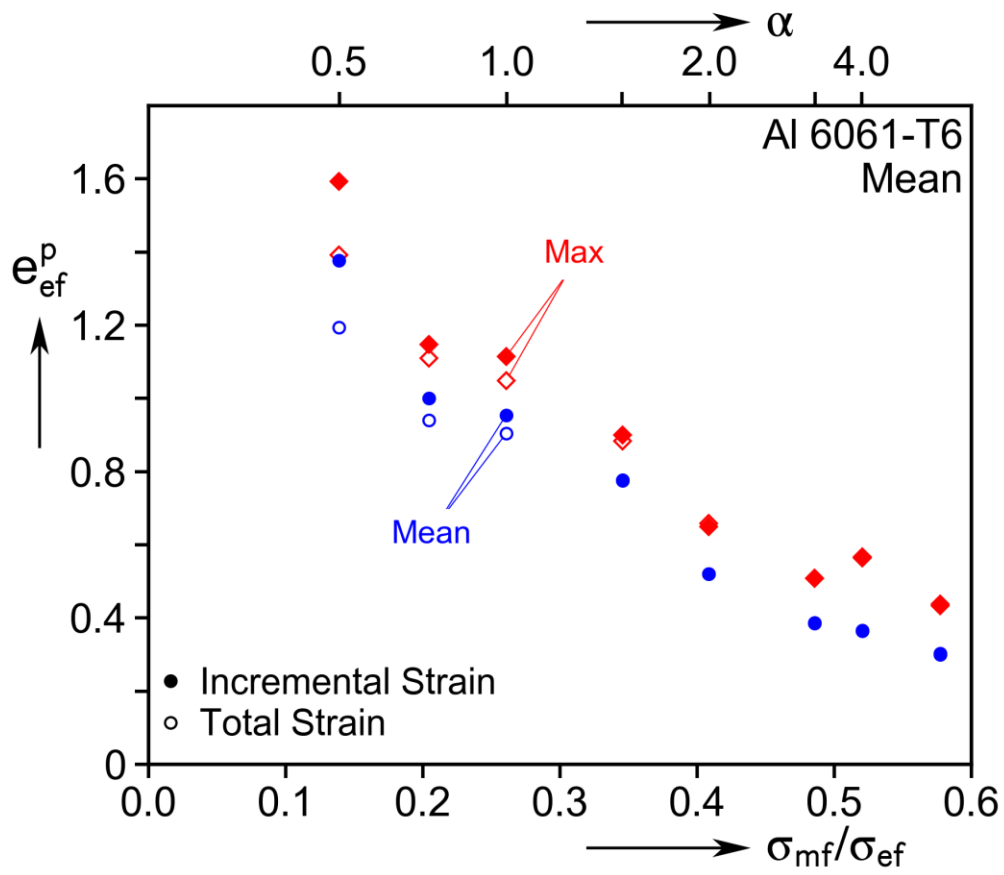

Fig. 4.12: *Incremental* and *Total* equivalent plastic strains in the radial-path experiments plotted against triaxiality at failure. *Max* and *Mean* measures are shown.

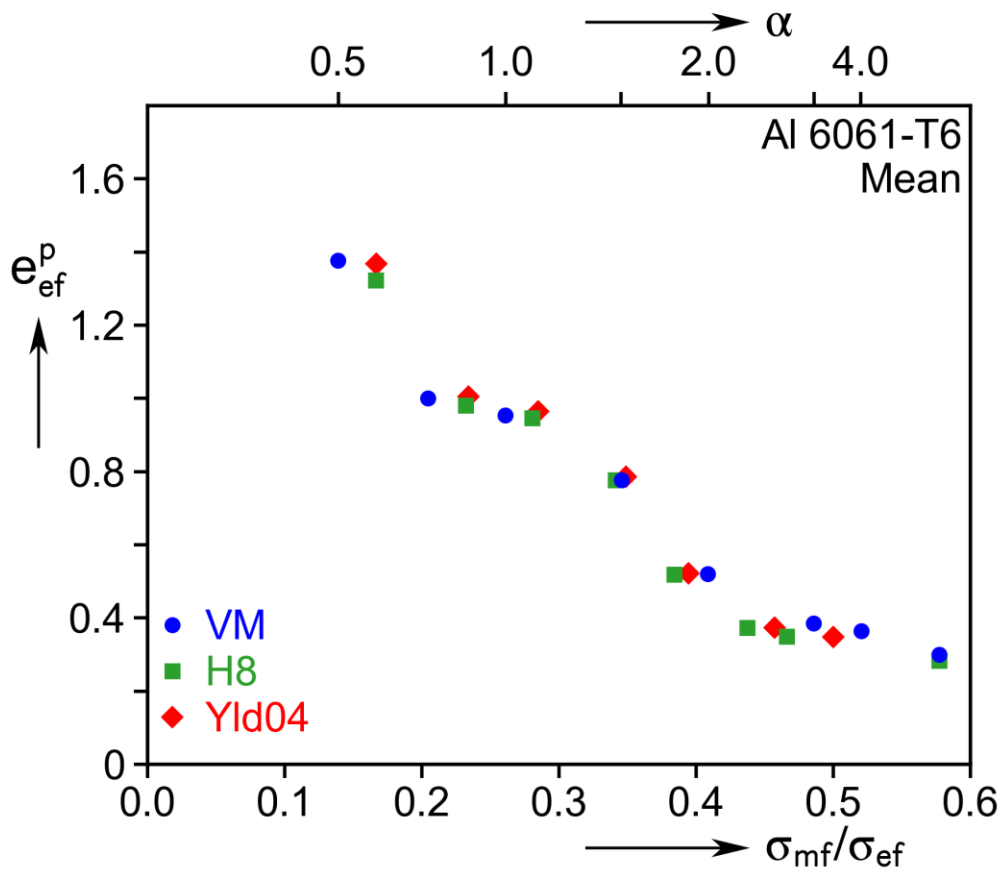

Fig. 4.13: *Mean* failure strains vs. triaxiality calculated incrementally with three different constitutive models: von Mises (VM), Hosford with exponent 8 (H8), and Barlat (Yld04).

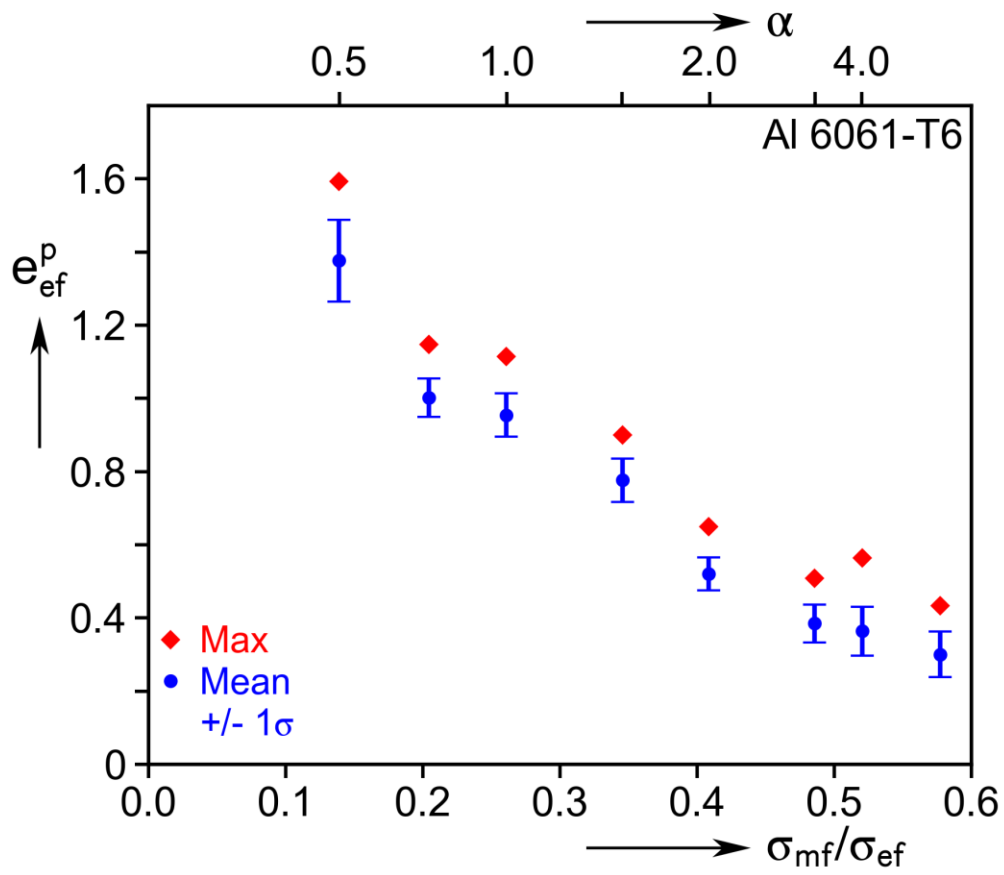

Fig. 4.14: Measured *Max* and *Mean* failure strains vs. triaxiality, with errorbars around the *Mean* showing one standard deviation (σ) of the distribution of column maxima.

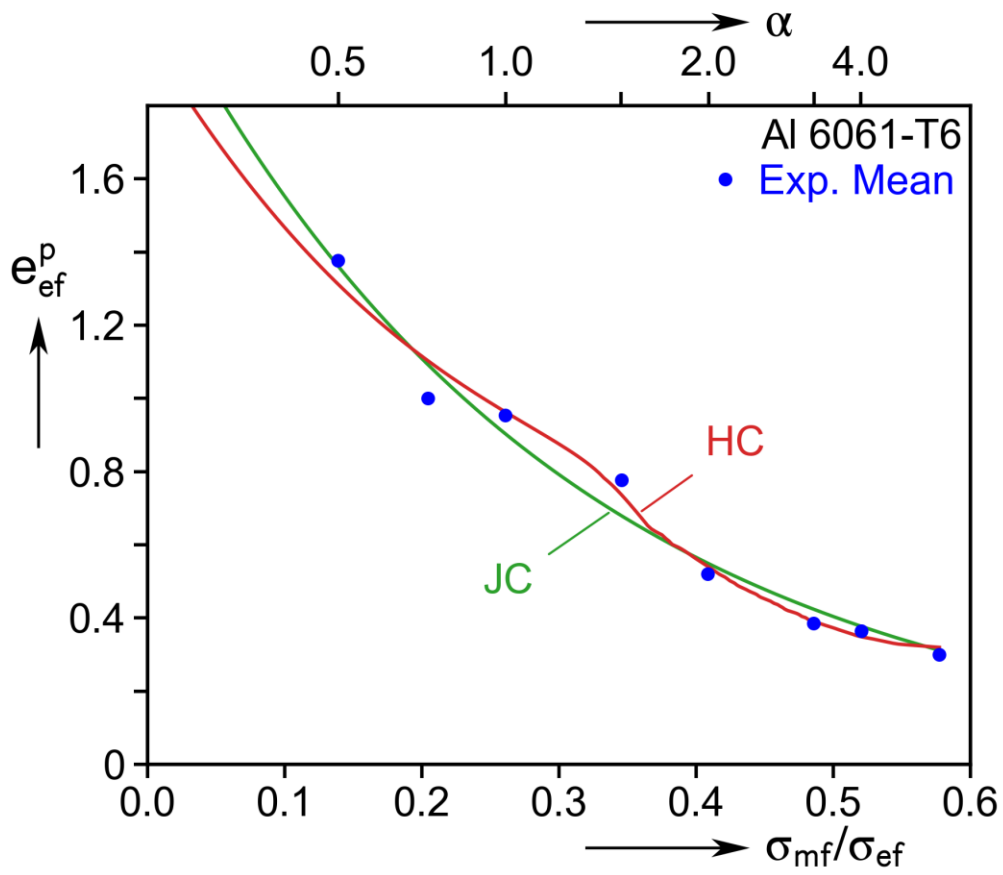

Fig. 4.15: The Johnson-Cook (JC) and Hosford-Coulomb (HC) failure criteria fit to the measured *Mean* failure strains (calculated using von Mises constitutive model).

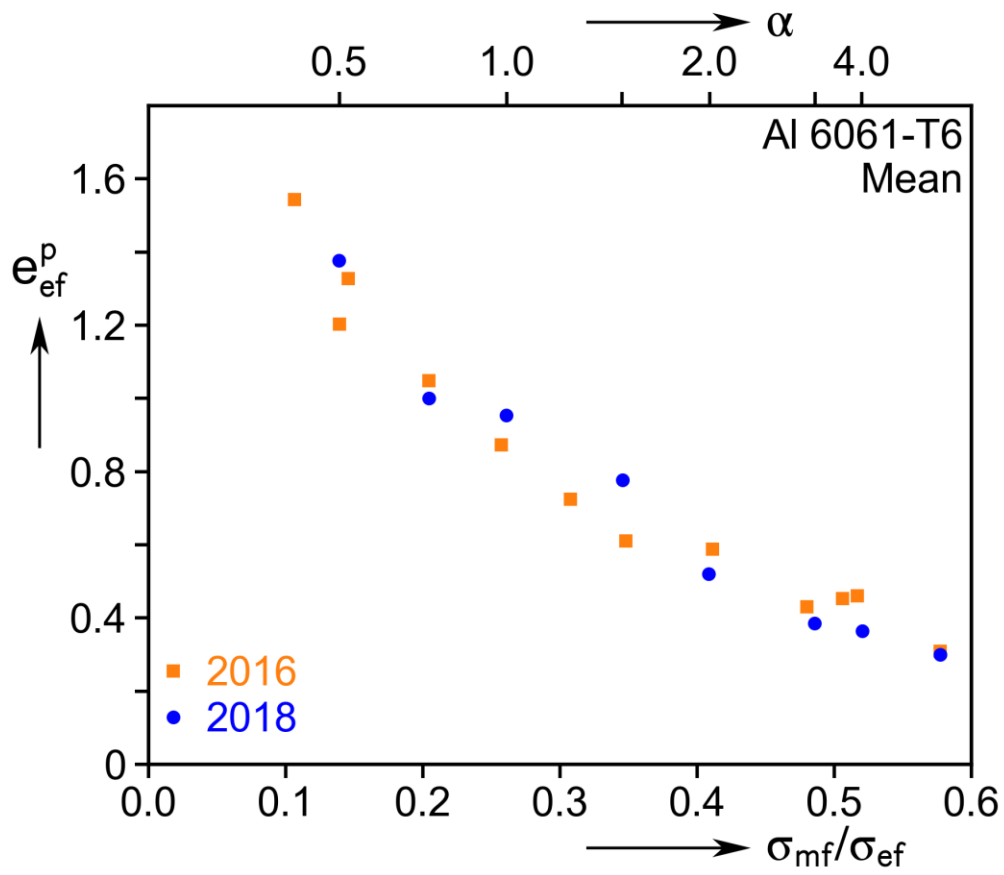

Fig. 4.16: *Mean* failure strains from experiments of Chapter 3 (2016) and the measurements from the new set of TT experiments (2018), both calculated incrementally using the von Mises constitutive model.

Chapter 5: Combined Internal Pressure and Tension

As described in Chapter 4, an effort to numerically simulate the tension-torsion experiments using an anisotropic constitutive model is currently underway. The calibration incorporated data from the tension-torsion experiments themselves, but it was determined that this dataset alone was insufficient. Therefore, a separate series of combined tension and internal pressure experiments was designed and conducted on the same stock tubing. These experiments were briefly presented in Scales et al. [2019].

The primary purpose of these pressure-tension (PT) experiments was to supplement the material database, yet the behavior that the material exhibits in this program also contributes to our experimental efforts to better understand ductile failure. Furthermore, the PT experiments are sufficient on their own for constitutive modeling and analysis for loadings that involve predominantly axial and hoop stress (Kuwabara et al. [2005], Korkolis et al. [2008a], Korkolis et al. [2010], Giagmouris et al. [2010]). This chapter presents these experiments in full.

Following the experiments, the 3D anisotropic constitutive model of Barlat et al. [2005] was calibrated using the measurements. The calibrated model was used in the extraction of the material stress-strain curve by tracking the post-limit load response of a uniaxial tension test. Finite element (FE) simulations that incorporated the constitutive model and the extracted stress-strain curve were subsequently conducted. The FE model's ability to reproduce the observed responses and deformation near failure was assessed, and compared to the performance of a FE model using isotropic plasticity. This chapter also presents the development and results of this numerical effort.

5.1 EXPERIMENTAL SETUP

The setup for these PT experiments involves draw inspiration from those reported in Korkolis et al. [2008b] and Korkolis et al. [2010], but the test hardware and specimen geometry are customized for the current effort.

The experiments involved tubular specimens that originated from the same stock tubing as the tension-torsion specimens reported in Chapter 4. They have a nominal outer-diameter (OD) and wall thickness of 2 inches and 0.187 inches (51 mm, 4.75 mm). The PT specimens are 12 inches long (305 mm) and feature a 4-inch long (101 mm) uniform test section that ends in 0.125-inch radii (3.18 mm) (see Fig. 5.1(a)). The nominal wall thickness in the test section is 0.05 inches (1.27 mm), which was chosen to minimize variation along the length while maintaining a thin wall relative to the OD in the test section. The ID along the test section was not machined, but the inside-diameter (ID) of the thicker end sections were bored slightly to 1.637 inches (41.55 mm). Plugs as shown in Fig. 5.1 (b) were inserted into the ends of the tube which seal the test section cavity with O-rings.

The tests were carried out in a 50 kip (222 kN) servo-hydraulic test frame that operates in conjunction with a separate 10,000 psi pressure booster (690 bar). The test setup is illustrated in Fig. 5.2. The tubes are loaded in radial paths in the nominal axial-hoop stress space, i.e., $\Sigma_x = \eta\Sigma_\theta$ with η constant. The nominal stresses are calculated directly from the internal pressure and axial force via the standard assumptions for a thin-walled cylindrical pressure vessel:

$$\Sigma_\theta = \frac{PR_o}{t_o}, \ \Sigma_x = \frac{F}{2\pi R_o t_o} + \frac{PR_o}{2t_o}, \tag{5.1}$$

where P and F are the applied pressure and axial force, and R_o and t_o are the initial mean radius and thickness. The desired radial path is achieved by operating the pressurizing system in volume control, and using the pressure as a command signal for the axial force.

Deformations were established through the use of 3D digital image correlation (DIC). Our system employs two 5 MP digital cameras equipped with 50 mm lenses. For these experiments the cameras were oriented vertically to accommodate the long, cylindrical test section. The cameras were positioned approximately 34 inches (87 cm) from the specimen surface, and 13 inches apart (33 cm). Correlation and deformations were computed using GOM ARAMIS v 6.3. For obtaining data for the calibration of the constitutive model, a relatively-large facet size and spacing of 30/10 pixels, corresponding to roughly $1.2t_o/0.4t_o$, was used. For analysis of the localized deformations, a finer facet size and spacing of 15/5 pixels ($0.6t_o/0.2t_o$) was used to enable a higher-resolution measurement. DIC gives the full-field displacement and strain history on one side of the specimen, and the strains reported herein are the average strains within a region in the central 1" of the test section that spans 90^o circumferentially. See Chapter 2 for further details on DIC.

5.1.1: Calculation of Cauchy Stresses and Plastic Strains

Establishing the Cauchy stresses and plastic strains is important, among other reasons, for accurately calculating the plastic work and ultimately calibrating an anisotropic yield function. The method of calculating these quantities up to the load maximum in a uniaxial tension test is of course well established. For the PT experiments, an iterative scheme was employed. In a given stage, the total logarithmic surface strains ε_x and ε_θ are obtained directly from the DIC data, and incompressibility is assumed to estimate the current wall thickness:

$$t = t_o \exp(-\varepsilon_x - \varepsilon_\theta)\,. \tag{5.2}$$

This estimate of the current thickness is used in the equilibrium equations to estimate the true stresses σ_x and σ_θ, which are then used in calculating the true plastic strains via:

$$\varepsilon_x^p = \varepsilon_x - \frac{1}{E}(\sigma_x - \nu\sigma_\theta) \text{ and } \varepsilon_\theta^p = \varepsilon_\theta - \frac{1}{E}(\sigma_\theta - \nu\sigma_x) \tag{5.3}$$

The through-thickness plastic strain $\varepsilon_r^p = -(\varepsilon_x^p + \varepsilon_\theta^p)$, which with the stresses are used to calculate the total through thickness strain. Finally, with this quantity, the estimated current thickness is updated using Eq. 5.2. This procedure is repeated until the calculated thickness converges. In all experiments analyzed this procedure converged rapidly without numerical difficulties.

5.2: Experimental Results

5.2.1: Summary Results

Seven radial-path PT experiments with η = {0, 0.25, 0.5, 0.75, 0.9, 1.0, 1.2} were conducted. This experimental series is largely limited to the hoop stress-dominant stress states because the axial loads reached in experiments with η > 1.2 exceeded the limits of our gripping setup and resulted in slipping. In fact, the wall thickness of the specimen used for η = 1.2 was reduced to 0.04 inches to mitigate the risk of slipping during the test.

The measured specimen geometries and key results are summarized in Table 5.1. The nominal stress and strain histories are shown in Fig. 5.3 (a) and (b). The results from a uniaxial test are also included. Each of these experiments achieves a pressure maximum (indicated by ▲), beyond which the deformation localizes. However, failure in all cases occurred without a significant drop in pressure beyond the maximum. The energy stored in the pressurizing fluid led to rapid growth in deformation after the initiation of the

localized band. As a result, failure was quite sudden and catastrophic, and the growth in *average* strain beyond the maximum is limited in most cases. The responses exhibit the expected trends, with the strain history showing increasing axial strain with increasing η. Interestingly, the two uniaxial cases ("Uniax." and $\eta = 0$) and the equibiaxial case ($\eta = 1.0$) exhibit significantly more deformation than the other biaxial tests.

As seen in Fig. 5.4, the maximum nominal hoop stresses (and accordingly the maximum pressure) reached in these experiments did not differ very much with η, with the exception of $\eta = 1.2$. For all experiments with $\eta \leq 1.0$, the maximum hoop stresses fell within the narrow range of 44.2 to 46.4 ksi (305 to 320 MPa), and no clear pattern is evident between η and the maximum hoop stresses. The same is true for the strains at the pressure maximum, which in these experiments vary between 4.44% and 5.89% with no apparent trend in their order. The corresponding maximum axial stresses and strains, in contrast, follow the expected trend of increasing axial stresses achieved increase with increasing η. This behavior suggests that the development of the instability that precedes failure is governed predominantly by the hoop stress (pressure); the axial stress does not begin to influence its development until the stress state is dominated by axial stress.

In all experiments with $\eta \leq 1.0$, the localization took the form of a narrow, axial band with width the order of the wall thickness and length the order of the tube radius. In most cases the band developed in the mid-span of the test section. In Expt. PT-10 with $\eta = 1.2$, the localization formed along a circumferential band somewhat closer to one end of the test section. Contours of the measured equivalent strains in the last stage prior to failure are shown for experiments with $\eta = \{0, 0.25, 0.5, 1.0\}$ in Fig. 5.5 (a). Below in Fig. 5.5 (b) is a photograph of the same burst specimens. It is evident that the failure follows the localization just described. Bulging in the test section is evident for $\eta = 0$ and

η = 1.0. It is also worth observing that the tubes appear longer with increasing η, which is indicative of the greater axial strain that develops with increasing η.

Despite the rapid growth in strain and sudden failure following the pressure maximum, the DIC system acquired images at a rate of 1/sec and was able to capture to some degree the evolution of the localized deformation prior to rupture. The nominal hoop stress-strain response for Expt. PT-12 with η = 0.25 is shown in Figure 5.6 (a). Five stages along the response are identified: stage 1 is quite early in the response though well past the onset of yielding, stage 2 is the pressure maximum, and the remaining are equally spaced up to failure. Figure 5.6 (b) plots the equivalent strain along a circumferential profile that crosses the localization zone at these five stages. Early on in stage 1, the strain profile is essentially flat. At the pressure maximum at stage 2, a modest "bulge" of higher strain exists over the central four wall thicknesses (-2t_o to 2t_o) with a maximum strain of 0.14 and average value of 0.1. Beyond this time, the strain increases only within roughly the central 2t_o, reaching a maximum equivalent strain of 0.24 in stage 5, the last one prior to failure. This compares to an average equivalent strain of 0.065 in the entire area over which strains were averaged for Figs. 5.3 and 5.4, which is essentially the same level as the profile away from the central peak. Table 5.1 reports the area-averaged strain components as well as the maximum local strains measured. The magnitude and rate of growth of strain seen here is not as dramatic as the profiles reported for the axial-shear experiments presented in Chapters 2 and 3, but the behavior is consistent.

5.2.2 – PT-8 (η = 1.0) Discussion

Experiment PT-8 with η = 1.0 is worthy of some additional discussion because its prescribed stress state is nearly equibiaxial. Deformation and localization of sheet metals under nearly-equibiaxial loading was examined in detail in Chen et al. [2016] and

Chen et al. [2018a] through hydraulic bulge tests. In these studies, the material did not develop localized deformations in the form of a narrow band, but rather more diffuse localized wall-thinning around the apex of the bulge (Brown and Sachs [1948] observed the same long ago). However in the present PT experiments on tubular specimens, and as previously shown in Korkolis et al. [2008b] and Korkolis et al. [2010], the material develops a more traditional band of localization which leads to failure. Furthermore, whereas in the present case the localized wall thinning developed in an axial band, those works reported that these experiments developed a circumferential band. Therefore it is evident that while the prescribed stress state in these different situations is nearly identical, that may only be the case when the deformations are small and the geometry has not changed significantly. Ultimately, the deformation and the exact nature the localization is governed by the specific material, test geometry, and setup.

This experiment's nominal hoop response with five marked stations and corresponding strain profiles across the localization zone are shown for in Fig 5.7. The profiles are similar to those in Fig. 5.6 with one notable exception: the strain outside of the central peak continues increasing after the pressure maximum (stage 2 in Fig. 5.7(a)). At the pressure maximum, the strain away from the center is approximately 0.08, whereas in the last stage prior to failure, this level has increased to 0.11. This observation suggests that the bulging instability characteristic of these structures and equibiaxial loading continues to develop even as the localized band develops.

5.3: MECHANICAL CHARACTERIZATION

5.3.1: Constitutive Modeling

Three different constitutive models and their ability to properly capture the measured material response in the axial-hoop stress space are evaluated. The first is the

traditional isotropic model of von Mises (≡ VM). Second is the non-quadratic, isotropic yield function of Hosford [1972]:

$$|s_1\text{-}s_2|^k+|s_2\text{-}s_3|^k+|s_3\text{-}s_1|^k = 2\sigma_o{}^k \tag{5.4}$$

with k = 8 (≡ H8), which is known to be suitable for aluminum alloys. Finally, it has been shown (e.g., Giagmouris et al. [2010], Tardif et al. [2012]) that extruded materials may exhibit plastic anisotropy which must be incorporated into the constitutive model in the analysis of large deformations. Thus, the 3D, anisotropic, non-quadratic yield function of Barlat et al. [2005] (≡ Yld04) is the third constitutive model we evaluate. This yield function is given by:

$$\begin{aligned}\Phi = [&\left|S_1' - S_1''\right|^k + \left|S_1' - S_2''\right|^k + \left|S_1' - S_3''\right|^k + \left|S_2' - S_1''\right|^k + \\ &\left|S_2' - S_2''\right|^k + \left|S_2' - S_3''\right|^k + \left|S_3' - S_1''\right|^k + \left|S_3' - S_2''\right|^k + \left|S_3' - S_3''\right|^k]^{1/k}\end{aligned} \tag{5.5}$$

The tensors $\boldsymbol{S'}$ and $\boldsymbol{S''}$ are formed through linear transformation of the Cauchy stress as follows:

$$\boldsymbol{S' = C's = C'T\sigma = L'\sigma} \text{ and } \boldsymbol{S'' = C''s = C''T\sigma = L''\sigma} \tag{5.6}$$

in which $\boldsymbol{C'}$, $\boldsymbol{C''}$, $\boldsymbol{T}$, $\boldsymbol{L'}$, $\boldsymbol{L''}$ are transformation tensors. $\boldsymbol{T}$ transforms $\boldsymbol{\sigma}$ to $\boldsymbol{s}$ and $\boldsymbol{C'}$, $\boldsymbol{C''}$ contain the 18 anisotropy parameters which are established through the following calibration procedure. For each of the $\Sigma_x - \Sigma_\theta$ radial paths performed, let $(\varepsilon_x^w, \varepsilon_\theta^w)$ be the strains corresponding to

$$W^P = \int_0^{\varepsilon_x^w} \sigma_x d\varepsilon_x^p + \int_0^{\varepsilon_\theta^w} \sigma_\theta d\varepsilon_\theta^p = 1000 \text{ psi}, \tag{5.7}$$

and $(\sigma_x^w, \sigma_\theta^w)$ be the corresponding Cauchy stresses. This biaxial stress state is introduced in the current yield function's definition to form the equivalent stress $\sigma_e = \Phi(\sigma_x^w, \sigma_\theta^w)$, and the error function

$$\mathcal{E}_\sigma = \left(\frac{\sigma_e}{\sigma_{xo}^w} - 1 \right)^2 \tag{5.8}$$

is developed. σ_{xo}^{w} is the measured uniaxial flow stress at the same level of plastic work.

The measured strains are also used in the calibration as follows. The in-plane strain ratio $d\varepsilon_x^p / d\varepsilon_\theta^p$ can be calculated directly from experimental measurements and used to form the quantity

$$R_{\text{exp}} = d\varepsilon_\theta^p / d\varepsilon_r^p = -1/(1+d\varepsilon_x^p / d\varepsilon_\theta^p)\,. \tag{5.9}$$

Note that this corresponds to the traditional Lankford parameter for the case of uniaxial tension. The flow rule is used to calculate the in-plane strain ratio predicted by the constitutive model for a given stress state:

$$R_{\Phi,x/\theta} = \left.\frac{\partial\Phi/\partial\sigma_x}{\partial\Phi/\partial\sigma_\theta}\right|_{\sigma_x^w,\sigma_\theta^w} \tag{5.10}$$

From this quantity, the through-thickness *R*-value predicted by the constitutive model, R_Φ, is calculated in the same manner as Eq. 5.9. Finally, a strain-ratio error function is formed:

$$\mathcal{E}_R = \left(\frac{R_\Phi}{R_{\text{exp}}} - 1\right)^2 \tag{5.11}$$

This through-thickness strain ratio was used in the error function rather than a simple in-plane strain ratio as it led to a better-conditioned optimization problem and ultimately better results. The flow stress and *R*-value from uniaxial tension is incorporated in exactly the same manner, but of course $\sigma_\theta = 0$. The above error functions for each experiment are summed to form a global error function, each individual term with its own weight parameter:

$$\mathcal{E} = \sum_{i=1}^{8} \omega_{\sigma i}\mathcal{E}_{\sigma i} + \omega_{Ri}\mathcal{E}_{Ri} \tag{5.12}$$

This global error function was then numerically minimized using the basinhopping algorithm of the *Scipy* python package (Jones et al. [2001]). Following the guidance in Barlat et al. [2005], $\omega_{\sigma i}$ was assigned the value of 1, and $\omega_{Ri} = 0.1$. However, in this work,

the flow stress and strain-ratio error functions for both uniaxial tension and $\eta = 0$ were over-weighted by 10-times the normal factor, and the strain-ratio for $\eta = 1.0$ was similarly over-weighted. These over-weights ensured that the corresponding experimental data was well-captured by the calibrated constitutive model.

Note that because the stress states used in the calibration are strictly in the σ_x-σ_θ space, six of the constitutive model's 18 anisotropy parameters play no role in the equivalent stress. As a result, it is impossible to include these six parameters in the optimization process, and they are assigned the value of 1. The calculated anisotropy coefficients are shown below in Table 5.2.

A work contour of the calibrated constitutive model is shown in the axial-hoop stress space (normalized by the uniaxial tension flow stress) in Fig. 5.8. Also included in this figure are work contours of the H8 and VM, as well as the experimental stresses (marked with ●). The VM contour is clearly unsuitable for this material. By contrast, the calibrated anisotropic model captures the experimental data points quite well. Its flexibility is especially evident in that it captures the flow stress for $\eta = 1.0$, whereas H8 falls short in this neighborhood. The anisotropic model slightly overshoots the $\eta = 1.2$ data point, however this is likely due to the relative absence of data on the axial-stress side of the yield surface.

Another visualization of the calibrated constitutive model is shown in Fig. 5.9, which plots the constitutive models' and experimentally-measured *R*-values (as defined in Eq. 5.9) versus the loading-angle relative to uniaxial tension. The calibrated anisotropic model is clearly superior to the two isotropic models in reproducing the experimental strain ratios across the full set of experiments. While the H8 model is reasonably close for $30° < \tan^{-1}(1/\eta) < 75°$, it differs significantly from the two experimental measurements at

0° (uniaxial tension) and 90° (PT $\eta = 0$, pure hoop stress). The VM model, on the other hand, essentially fails to properly predict any of the measured strain ratios.

5.3.2: Extraction of the Large-Strain Hardening Response

Simulations involving large deformations require the material stress-strain curve to strains comparable to the levels reached in the analysis. The need for an accurate hardening response is especially critical in problems involving instabilities. The Al 6061-T6 alloy in this study begins to neck at roughly 7% nominal strain in uniaxial tension, but the strains within the localization zones that develop in the PT experiments exceed 0.2. A number of methods for obtaining an extended uniaxial response exist.

Perhaps the most common is an extrapolation using the fits of Voce [1948] and Swift [1952]. These extrapolations however have been shown (see Suttner and Merkelein [2015] and Chen et al. [2018a], for example) to be error prone when used for the analysis of instabilities. In this work we follow the inverse method in Tardif et al. [2012], which has the advantage of assuming no functional form for the hardening law. Others have since employed various closed-form hardening laws whose parameters are identified by minimizing the difference between an experimental and numerical response (Papasidero et al. [2015], Brünig et al. [2016], Ha et al. [2018]), or through even more complex optimizations (Gross and Ravi-Chandar [2015], Defaisse et al. [2018]). The process we follow involves matching the nominal response of a FE model to that of a uniaxial tension test, but does so by adjusting the stress-strain curve incrementally. The details of this method are as follows.

(a) Experiment and FE Model

The uniaxial tension experiment employs a specially-designed dogbone specimen whose 3-inch long (76 mm) gage section ($2L$) is made slightly narrower in the center (w_o = 0.365 in/9.27 mm) than at the ends (w = 0.375 in/9.53 mm). The tapered gage ensures necking develops in the center, and is introduced by machining into the sides a very large-radius (radius ~100x greater than the gage length). The resulting gradient in width is so slight that the stress and deformation remain approximately uniaxial. Figure 5.10 (a) shows a schematic of the specimen. It should also be stated that the 0.188-inch wall thickness of the stock tubes enabled a flat uniaxial specimen to be milled out of the curved tube wall. The resulting specimen was nominally 0.1 inch thick (2.54 mm).

The tensile test was carried out in the usual manner, with the electromechanical test frame operating in displacement control. The displacement rate was chosen to achieve a strain rate of approximately 10^{-4}/sec. Full-field displacements and strains were measured via the same 3D DIC system that was used in the PT experiments. The nominal strain (or normalized elongation) is computed from a gage length of $2L_g$ = 2 inches (51 mm) in the center of the test section.

A finite element model of the tensile specimen was developed in ABAQUS using 3D linear solid elements (C3D8R). The symmetry of the specimen geometry allowed just one-eighth of the specimen to be modeled, and the filleted ends and wider gripping region of the specimen were excluded from the model. An illustration of the mesh is shown in Fig. 5.10 (b). The mesh is highly-refined near the axial symmetry plane: it contains nine elements through the half-thickness, and the elements are nearly cubic in aspect, resulting in 33 elements along the half-width. The fine mesh transitions to a coarser isotropic mesh at a distance of $0.6w_o$ up from the axial symmetry plane. This coarser mesh contains three elements through the half-thickness and 11 elements along half-width. The nodes at the top

of the model are kinematically constrained to a single reference node. Loading is accomplished by prescribing an axial displacement to this node.

The maximum displacement increment of the top reference node was limited to 6.3×10^{-4} inches such that the maximum nominal strain increment did not exceed 0.06%. A minimum increment was not specified, however, and the nominal strain increment beyond the limit load was at times automatically reduced by the solver to around 0.03% nominal strain and decreased even further near the end of the analysis.

The initial true stress-plastic strain curve for the FE model is taken directly from the pre-limit load experimental response and linearly extrapolated to larger strains. A first simulation is run using this initial true stress-plastic strain curve. The resulting nominal response is compared to the experiment, and the increment of the simulation in which the two nominal responses deviate is identified. The average equivalent plastic strain in the elements on the axial symmetry plane in this increment are exported from the results file. The input flow stress at this value of plastic strain is adjusted up or down depending on whether the simulation's nominal stress-strain response over- or under-predicted the experimental response. The evaluated tangent modulus is now linearly extrapolated. This process is repeated until the simulation's nominal stress-strain curve matches the entirety of the experiment's (or until the tangent modulus reaches zero).

A constitutive model of course must be adopted for the FE model, and in fact the choice of constitutive model plays a significant role in the performance of the model and resulting extracted stress-strain curve. The same three constitutive models addressed above were considered here. The nominal response and extracted stress-strain curve of each model are shown in Fig. 5.11 (a) and (b), and the experimental response is included in (a). The three simulation results match the experimental response perfectly until well past the limit load. The VM model, however, is unable to track the experiment near the end of the

response when the stress is decreasing the fastest, while the H8 and Yld04 models track the entire response.

The resulting difference in extracted stress-strain curves, shown for the three constitutive models in Fig. 5.11 (b), is apparent. Note that the dashed portion is a linear extrapolation of the tangent modulus reached at the end of the extraction process. The VM curve softens rapidly and plateaus at an equivalent stress of 51.0 ksi (351 MPa) and plastic strain of about 0.24. The extracted curve for the H8 model hardens to a greater extent than VM, but also finishes with a tangent modulus of essentially zero at a stress of 51.7 ksi (356 MPa) and strain of 0.32. Finally, the extraction using the calibrated anisotropic constitutive model hardens significantly more than the other two, and in fact hardens throughout the entirety of the simulation, ending with a positive tangent modulus at a stress and strain of 54.0 ksi (372 MPa) and 0.37. We speculate that had the specimen in the experiment elongated further prior to failing, the extracted Yld04 stress-strain curve would have continued to soften and eventually plateaued like the others.

5.4: SIMULATION OF THE PT EXPERIMENTS

5.4.1: Finite Element Model

A finite element model of the PT experiments was developed in ABAQUS/standard. Symmetries enabled modeling one-fourth of the structure. Note that an axisymmetric model is not appropriate due the nature of the localized deformations. The tube is modeled with 3D solid, linear elements (C3D8R), and the mesh is partitioned into several regions with different levels of refinement. The mesh and model geometry that was used for all cases except $\eta = 1.2$ are shown in Fig. 5.12. For all cases, the model's wall thickness and mean radius matched that which was measured in the corresponding test specimen.

A fine-mesh region with three-elements through the wall thickness extends from the axial symmetry plane (x = 0) up to an x-coordinate of $1.3R_o$ (indicated as L_f in the figure). This region spans 30° in the circumferential direction (θ), corresponding to approximately $9t_o$. The mesh is coarser axially and circumferentially outside of this region, though it is axially refined around the radiused end of the test section before being coarsened once again outside the test section. The end section of the tube model has an OD of 1.9675 inches (50 mm) and is 0.35 inches long (8.9 mm), which corresponds to the typical length of the tube that protruded outside of the grips during an experiment. The mesh for $\eta = 1.2$ is similar, but the fine mesh region spans the entire model circumferentially and only extends $5t_o$ axially.

An imperfection is introduced on the ID of the model to help trigger the onset of localization. The affected region is highlighted in Fig. 5.12. It extends one tube-radius axially (L_d in the figure). Circumferentially, the imperfection follows a cosine shape with a magnitude that is maximum at $\theta = 0$ and decreases to zero at a distance $2t_o$ away from the symmetry plane. The length and width was motivated by the shape of localized deformations that were observed in the experiments.

Nodes on the axial symmetry plane (x = 0) are constrained except in the radial direction, while nodes along the x-θ symmetry plane are constrained only in the circumferential direction. Nodes on the upper surface of the model are kinematically constrained to a reference node. The tube is pressurized through the use of incompressible fluid elements (type F3D3), which ABAQUS generates automatically during preprocessing. The tube's inner surface and symmetry conditions define the fluid cavity boundaries at x = 0 and along the x-θ plane, while surface elements (type SFM3D3, not shown) were constructed at the top opening of the tube to close the cavity. Loading in the simulations mimics the volume-control and feedback used in the experiments: A volume

increase is prescribed, and the corresponding pressure is used as a sensor. A user-amplitude routine (UAMP) takes the pressure and applies an appropriately-scaled force to achieve the same radial-path loading that was prescribed in the experiments (see Eq. 5.1).

5.4.2: Simulation Results

The full set of radial path experiments was simulated numerically using each of the three constitutive models and corresponding extracted stress-strain curve. All simulations employed an imperfection as described above with a maximum wall-thickness reduction of 3% (see Appendix B for a presentation of imperfection sensitivity). The resulting axial-hoop strain paths (dashed lines, limit load = △) are shown along with the experimental paths (solid lines, limit load = ▲) in Fig. 5.13 (a-c). The numerical strains presented here are calculated by averaging the strains in all elements located in the same region over which strains were averaged in the experiment. The responses shown are truncated at the point when maximum equivalent strain within the localizing zone reaches the maximum local strain measured in the experiment, though the analyses continued to run past this time.

The VM predictions (Fig. 5.13 (a)) do not follow any of the experimental paths with the exception of $\eta = 0.5$. The H8 predictions (Fig. 5.13 (b)) improve significantly, with $\eta = \{0.25, 0.5, 0.75, 1.2\}$ all reproducing the experimental paths reasonably well. The strains at the pressure maximum also improve in going from VM to H8. However the H8 predictions still differ for stress states closest to equibiaxial ($\eta = \{0.9, 1.0\}$) and uniaxial loading ($\eta = 0$). Finally, the predicted paths using the calibrated Yld04 model shown in (c) match the experimental ones exceedingly well in all cases. With the exception of $\eta = 1.0$, the strains at the pressure maximum align with the experiment also. The vast difference in the predicted strain paths by these three constitutive models falls in line with what was shown in Fig. 5.9, where only Yld04 captured all the experimental R-values, H8 captured

some (but notably failed to capture $\eta = 0$), and VM captured only $\eta = 0.5$. These trends are similar to those reported in Korkolis et al. [2010] for the same alloy.

Figure 5.14 presents the full set of axial and hoop stress-strain responses predicted using the Yld04 constitutive model. The results compare quite favorably to those shown for the experiments in Fig. 5.4, and reproduce all of the key features seen in the experimental responses, including the similarity in maximum hoop stresses and corresponding strains for $\eta \leq 1.0$ (Fig. 5.14 (a)), and the trend of increasing axial stress and strains with increasing η in Fig. 5.14 (b).

(a) $\eta = 0.25$

As mentioned in Section 5.2.1, these experiments failed rapidly following the pressure maximum, and as a result, the growth in strain we were able to record was limited even inside the localization zones. The analysis therefore offers the opportunity to further study the evolution of deformation in these zones. The nominal hoop responses for the $\eta = 0.25$ experiment and Yld04 analysis is shown in Fig. 5.15 (a). The same five stations marked in Fig. 6 (a) are marked on the experimental response here, and nine stations are identified in the response of the analysis. Station 4 of the analysis essentially coincides with station 5 of the experiment (the last stage prior to failure). The maximum strain of 0.22 predicted by the analysis here compares quite well with the maximum experimental strain of 0.26. From this stage onwards, the predicted strains continue to grow only within the central $2t_o$, and in station 9 (the last increment of the analysis), the maximum strain reaches 0.47. This large, local value compares to the average nominal strain of 0.07 seen in Fig. 5.15 (a). Notice also that the strain level seen in the profiles outside of the localizing zone remains constant following the pressure maximum, which is exactly what was observed in the experiment. Therefore it is evident that in this hoop-stress dominant stress state, the

localized deformation that leads to failure is the dominant instability; the bulging instability that precedes the localization in these structures plays a minor role.

An image of the deformed mesh at the increment corresponding to station 9 is shown in Fig. 5.15 (c) (contour color represents equivalent strain). Note that the model has been mirrored across a symmetry plane for visualization purposes. The deformation at this stage has concentrated in the center-most elements and rapidly declines circumferentially, echoing of the large gradient seen in Fig. 5.15 (b). An axial gradient exists as well. A reduction in thickness in these elements is also evident, clearly demonstrating that this structure fails by localized wall-thinning.

(b) η = 1.0

The performance of the three constitutive models is examined in greater detail for a single case with η = 1.0. The nominal hoop and axial stress-strain responses for the three models and the experiment are shown in Fig. 5.16. In both figures, the stress-level reached by the VM and H8 models are lower than the experiment by about 2 ksi (14 MPa). They also reached significantly greater strains before localizing. In fact, despite the introduction of a 3% imperfection, the VM model never localized for this prescribed stress. In contrast, the responses predicted by the Yld04 model follow the experiment much more closely, essentially matching the stress-level exactly. The strain at the pressure maximum is about 1% less than in the experiment, but the stresses are nearly identical. Furthermore, the average strains reached agree nearly perfectly with the measured deformations prior to burst.

The mild difference in stress levels reached by the three predictions and how they compare to the experiment can be attributed to how well these constitutive models accurately capture the stress state corresponding to η = 1.0 in Fig. 5.8. But the large

difference in average strain achieved is driven by the numerical model's propensity to localize, as the responses shown are terminated when the maximum equivalent strain in the localizing zone matches the value measured in the experiment at failure. Figure 5.17 shows this final equivalent strain profile from the experiment and the corresponding profiles predicted using the Yld04 and H8 models. The anisotropic model reproduces the experimental profile very well, tracing a comparable level of about 0.11 outside of the central zone before increasing within the central 1-1.5 t_o and localizing within this narrow zone. In stark contrast, the H8 model reaches a strain of about 0.15 outside of the localizing zone, which exceeds the experimental level. Furthermore, its localization profile is much broader than the experiment and Yld04 prediction. The VM model, as mentioned above, never localized and is not included in the figure (its profile is essentially a flat line). This figure is a strong reminder of the fact that the adopted constitutive model is of paramount importance in the prediction and analysis of localized deformations and instabilities.

Figure 5.18 (a) shows the experimental and Yld04-predicted nominal hoop response, with the same experimental stations identified as in Fig. 5.7. Seven predicted profiles are shown in Fig. 5.18 (b): 1-5 have the same value of average hoop strain as the experiment stations. Station 6 goes slightly beyond the experiment and is the last increment of the analysis. The analysis pressure maximum is also plotted (dashed line). As you can see, the profiles follow the same behavior that was seen in the experiment in Fig. 5.7: the deformation continues to grow *outside* the localizing zone following the pressure maximum (LL). From the LL to profile 6, the strain at the edges essentially doubles. This growth occurs simultaneously with further localization within the central t_o, with the maximum strain there growing from about 0.1 to over 0.4 in the same period. Interestingly, though, this localization does not appear to take over until profile 2 or 3. Thus, the analysis confirms that in this nearly-equibiaxial stress state, two different instabilities evolve at the

same time: the bulging instability which dominates the onset of the pressure maximum, and the localized wall-thinning instability that becomes the dominant driver of failure.

5.5: SUMMARY AND CONCLUSIONS

In support of a separate effort to numerically reproduce the tension-torsion experiments described in Chapters 2-4, a series of combined tension and internal pressure experiments on the same stock tubing were conducted. Test specimens were custom machined and featured a uniform test section 4 inches long and 0.05 inches thick. The tubes were loaded in radial paths in the nominal axial-hoop stress space, and the deformation was monitored via 3D DIC.

Seven experiments with η = {0, 0.25, 0.5, 0.75, 0.9, 1.0, 1.2} were conducted ($\Sigma_x = \eta\Sigma_\theta$). In six of the experiments, a pressure maximum was achieved. Shortly after the limit loads, localized deformations developed within an axial band with width the order of the wall thickness. In the axial-stress dominant η = 1.2 experiment, the specimen with a circumferential band instead. Deformation grew rapidly in the localized bands, and leading to sudden failure. Because of the abrupt burst, the measured maximum local strains prior to failure are not representative of the actual strain at failure.

Although the failure strains are underestimated, the responses recorded are useful for establishing material anisotropy when only the axial-hoop stress space is of interest. The 3D anisotropic constitutive model of Barlat et al. [2005] was calibrated using the pressure tension data and data from a uniaxial tension test. The calibrated constitutive model, as well as two isotropic models, were included in finite element simulations of the pressure-tension tube. Also included in the FE model was a material stress-strain curve that was iteratively extracted in the manner established in Tardif et al. [2012] for the VM, H8, and Yld04 constitutive models.

The FE model that included the calibrated Yld04 constitutive model and corresponding stress-strain reproduced all aspects of all experiments very well, including the nominal stress responses, strain histories, and the localization that preceded failure. The

two isotropic models did not fare as well. These results demonstrate that a constitutive model that accurately represents the material is essential for simulations involving large deformations and localization.

Table 5.1: Key measurements for seven radial path PT experiments.

Exp.	η	R_o in (mm)	t_o in (mm)	Σ_{xL} ksi (MPa)	$\Sigma_{\theta L}$ ksi (MPa)	ε_{xL} (%)	$\varepsilon_{\theta L}$ (%)	Σ_{xf} ksi (MPa)	$\Sigma_{\theta f}$ ksi (MPa)	ε_{xf} (%)	$\varepsilon_{\theta f}$ (%)
11	0	0.839 (21.3)	0.0498 (1.26)	0.9 (6)	44.2 (305)	-1.45	5.89	0.9 (6)	43.8 (302)	-1.33	24.59
12	0.25	0.839 (21.3)	0.0497 (1.26)	12.1 (83)	45.5 (314)	-0.36	5.12	12.0 (83)	45.4 (313)	-0.37	23.06
4	0.5	0.839 (21.3)	0.0498 (1.26)	23.4 (162)	46.4 (320)	0.10	4.92	23.4 (161)	46.2 (319)	0.22	21.14
2	0.75	0.839 (21.3)	0.0498 (1.26)	34.9 (241)	46.4 (320)	0.54	5.06	34.9 (241)	46.4 (320)	1.47	17.40
3	0.9	0.839 (21.3)	0.0501 (1.27)	41.2 (284)	45.8 (316)	1.22	4.44	41.2 (284)	45.7 (315)	1.78	20.38
8	1	0.839 (21.3)	0.0496 (1.26)	45.3 (312)	45.3 (312)	3.63	5.32	45.0 (311)	45.0 (311)	4.88	21.30
10	1.2	0.834 (21.2)	0.0399 (1.01)	47.3 (326)	39.5 (272)	4.77	1.21	47.1 (325)	39.4 (272)	24.81	2.19

Table 5.2 – Anisotropy Parameters

c'_{12}	c'_{13}	c'_{21}	c'_{23}	c'_{31}	c'_{32}	$c'_{44,55,66}$
-0.2846	0.4221	0.7066	0.6257	-2.0404	-1.3176	1.0
c''_{12}	c''_{13}	c''_{21}	c''_{23}	c''_{31}	c''_{32}	$c''_{44,55,66}$
-0.0378	0.2290	0.1698	0.0841	-0.9810	-2.4454	1.0

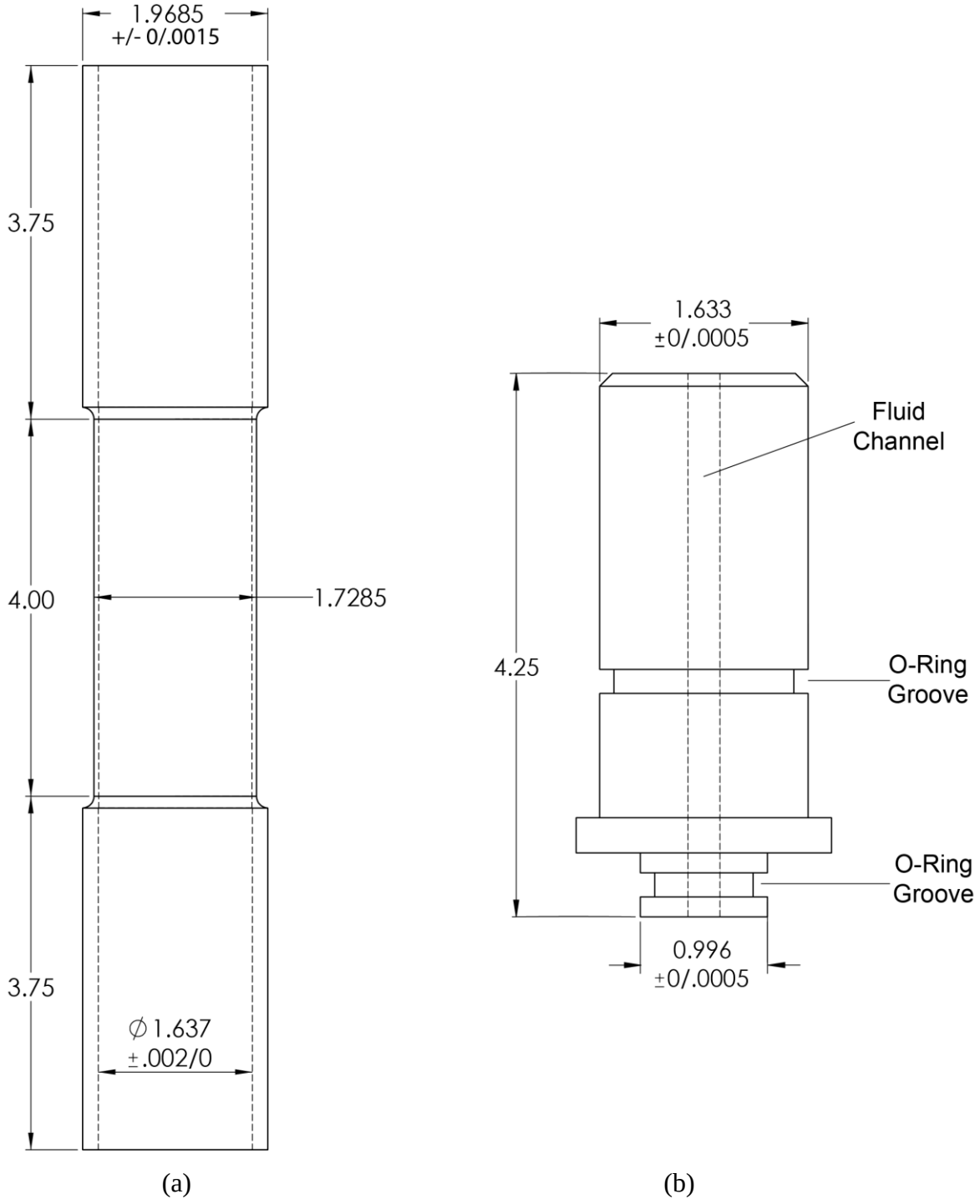

(a) (b)

Fig. 5.1: (a) Pressure-tension tube drawing. (b) Plug drawing.

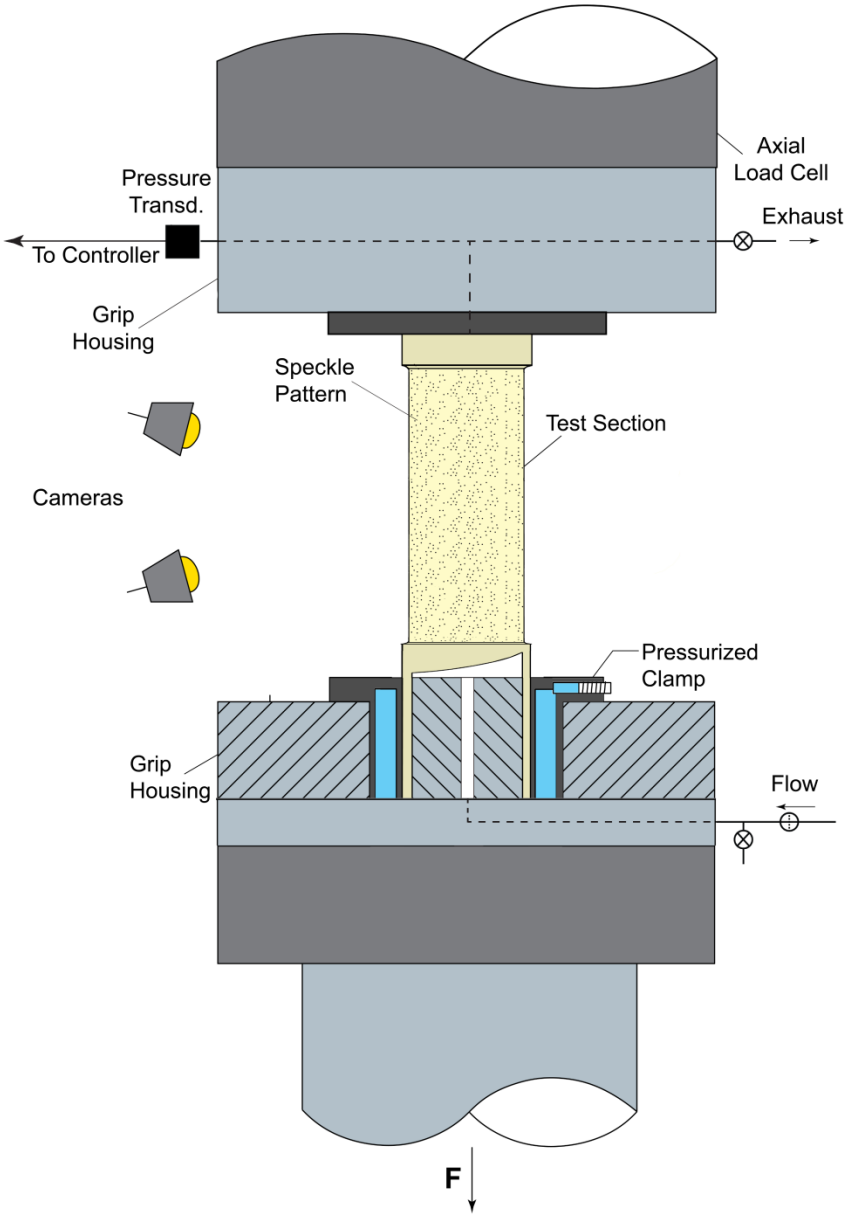

Fig. 5.2: Schematic of the pressure-tension experimental setup.

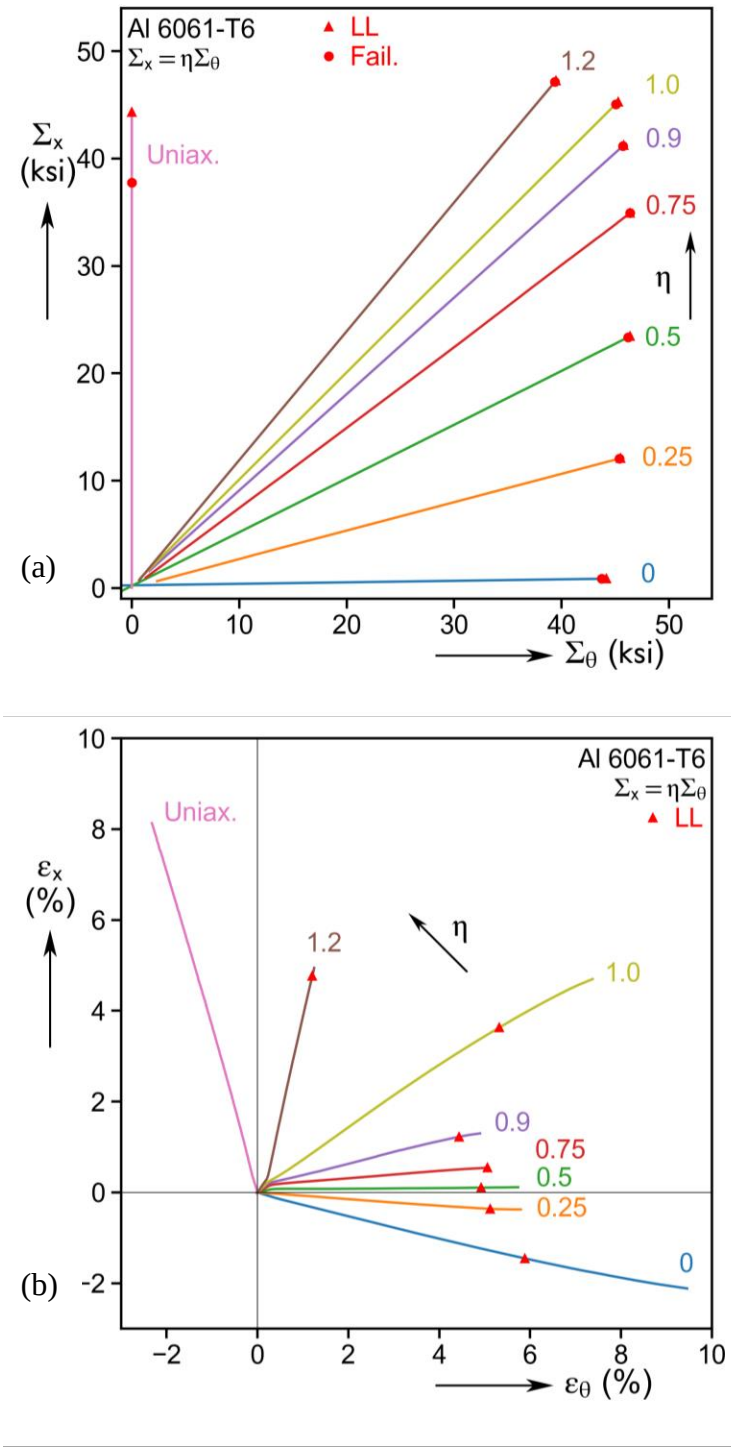

Figure 5.3: (a) Prescribed nominal stress histories of the seven PT tests, and one uniaxial tension test. (b) Corresponding strain histories.

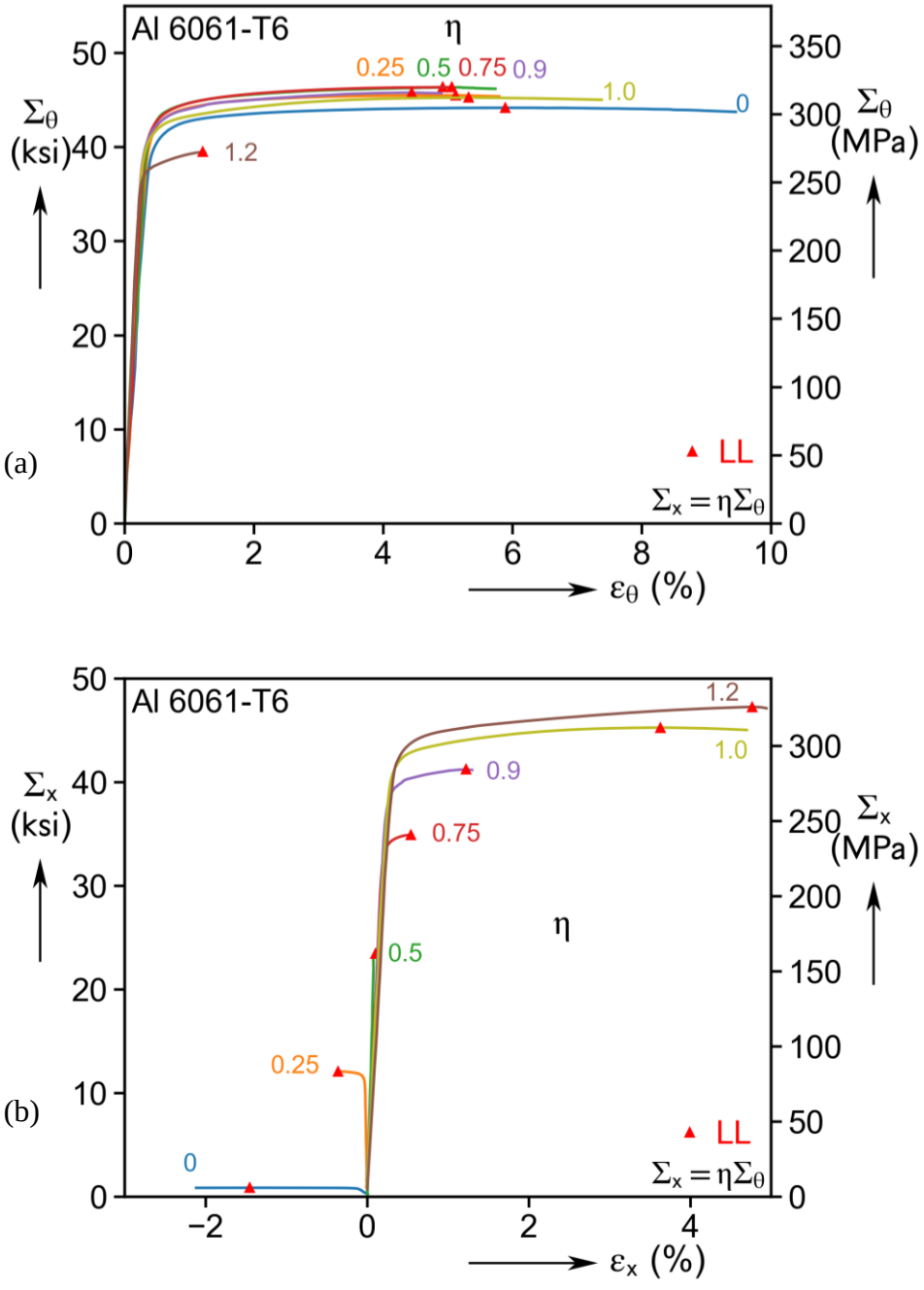

Figure 5.4: (a) Nominal hoop stress and strain responses of the seven PT experiments. (b) Axial stress-strain responses.

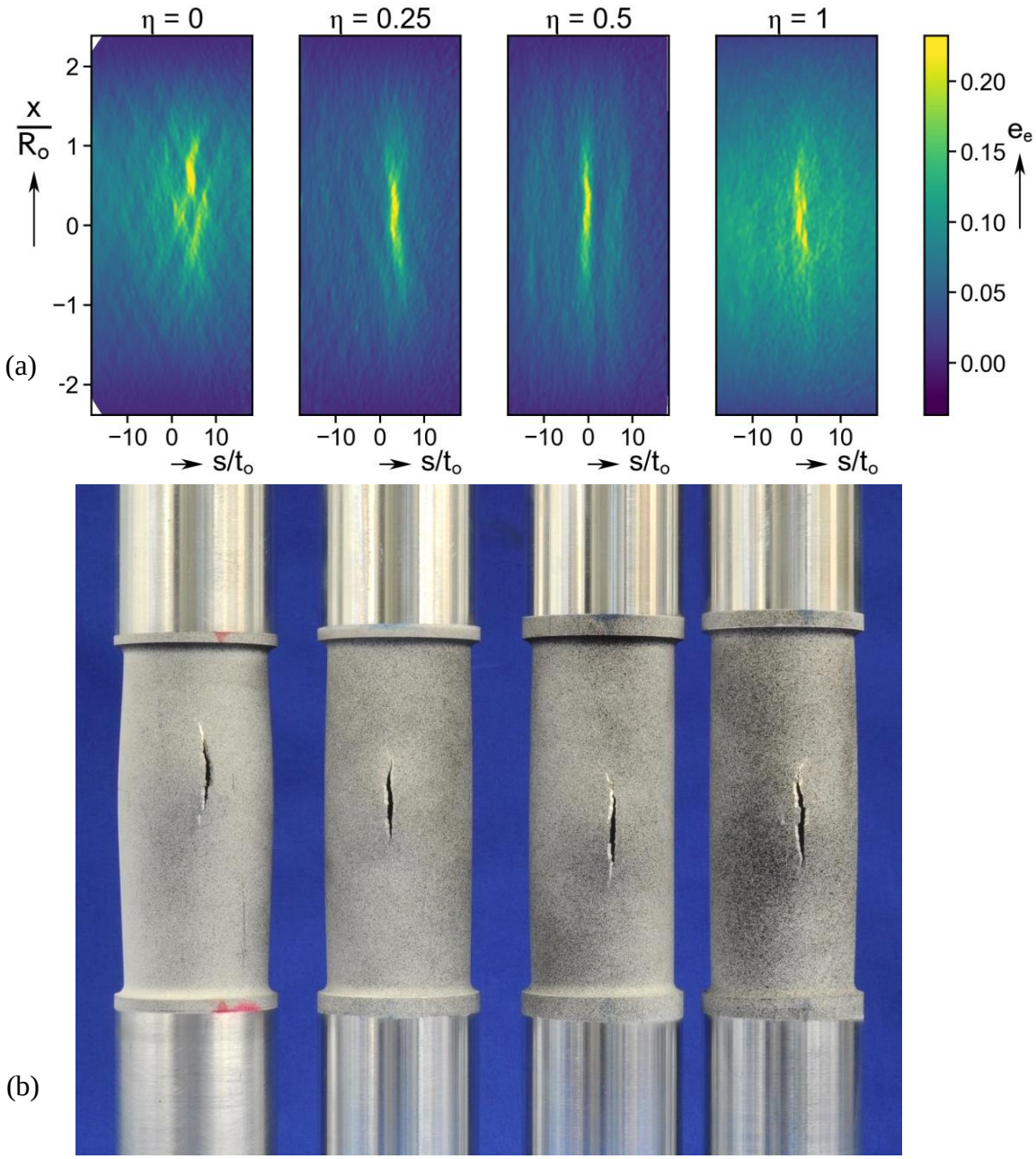

Figure 5.5: (a) Equivalent strain contours in the last stage prior to failure for experiments with $\eta = \{0, 0.25, 0.5, 1.0\}$. (b) Photographs of the same specimens after rupture.

(a)

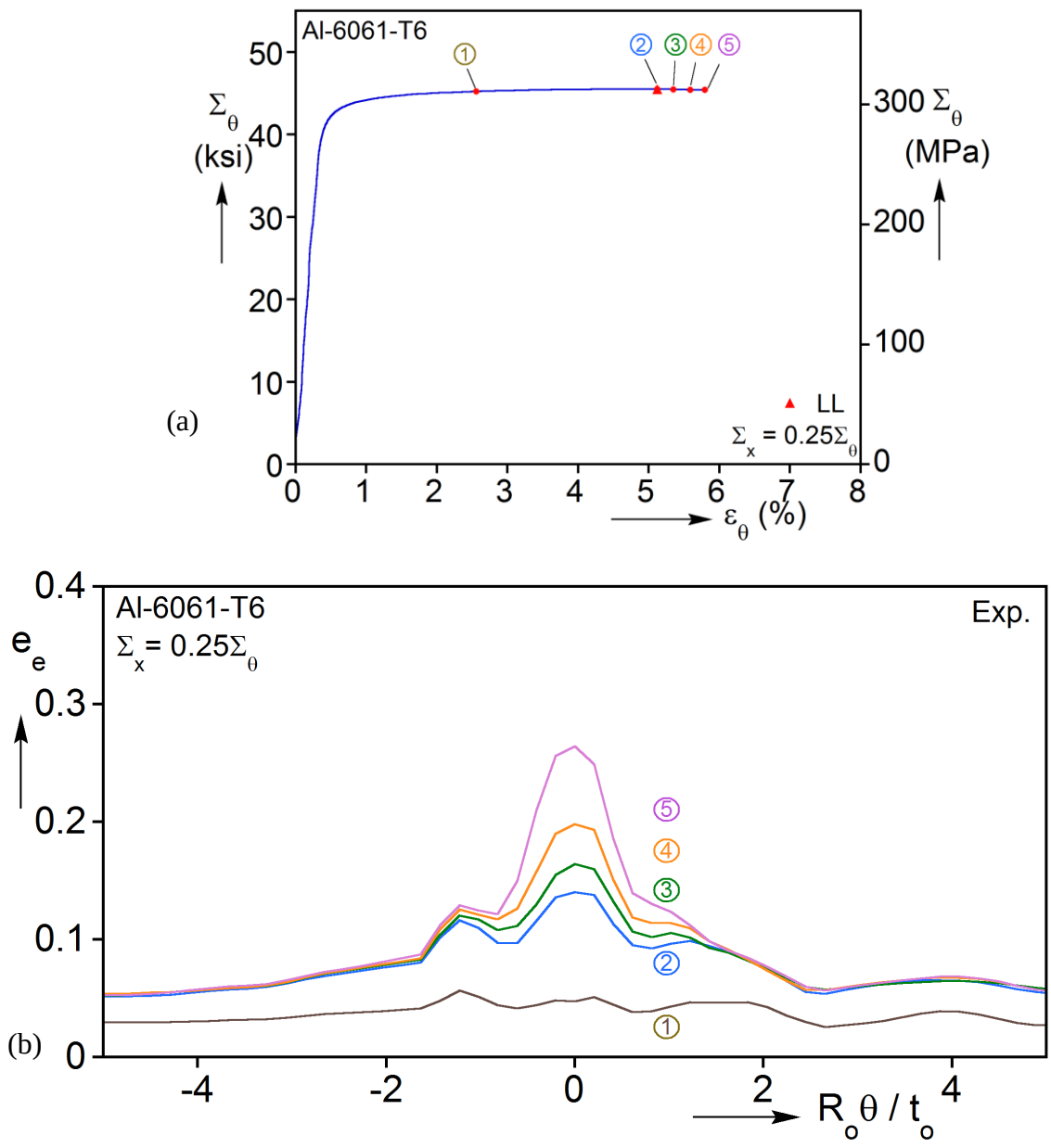

Fig. 5.6: (a)Nominal hoop stress-strain response for Expt. PT-12 with $\eta = 0.25$. Station ② is the limit load.(b) Strain profiles across the localization zone at the five stations marked in (a).

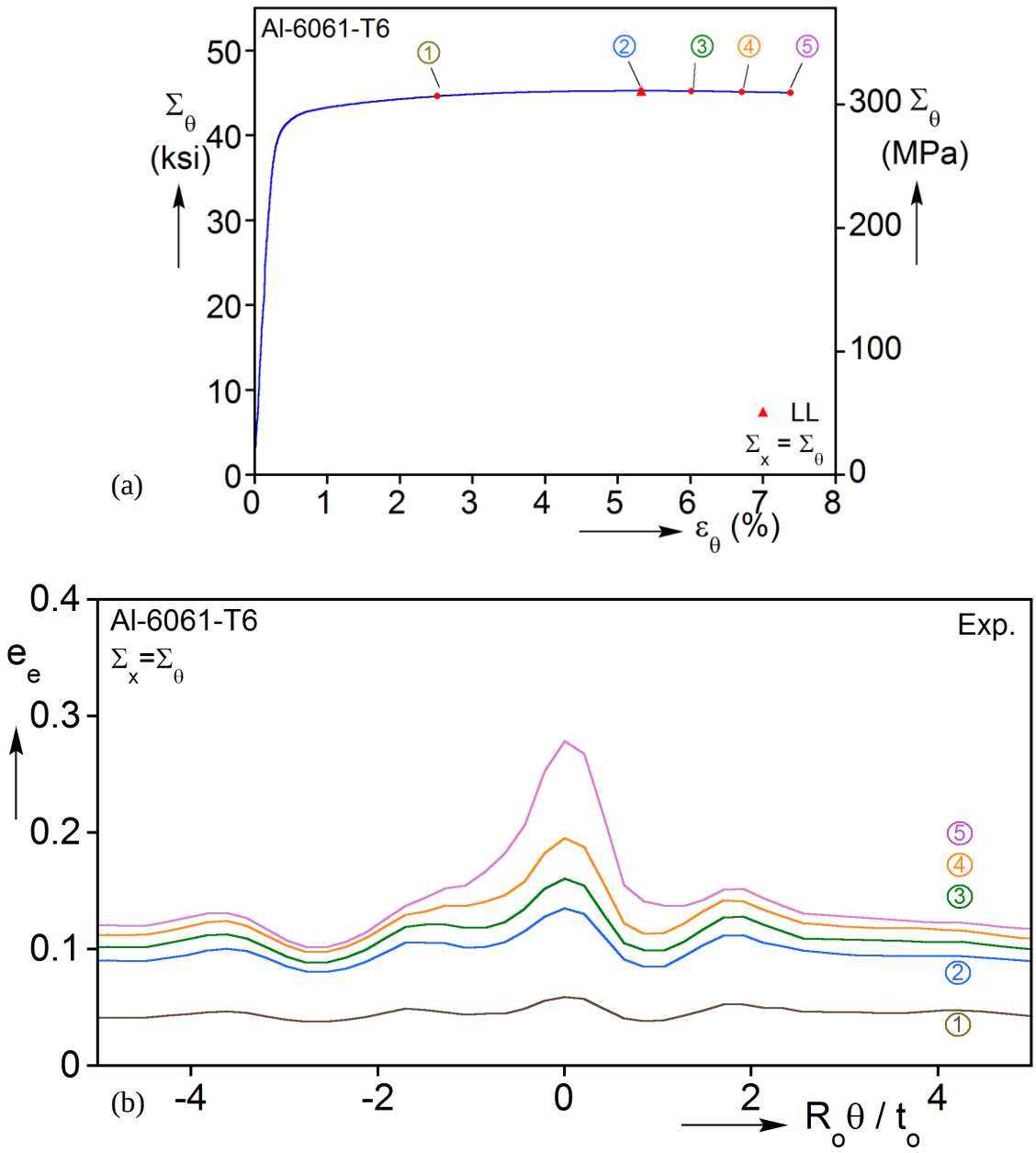

Fig. 5.7: (a)Nominal hoop stress-strain response for Expt. PT-8 with η = 1.0. Station ② is the limit load. (b) Strain profiles across the localization at the five stations marked in (a).

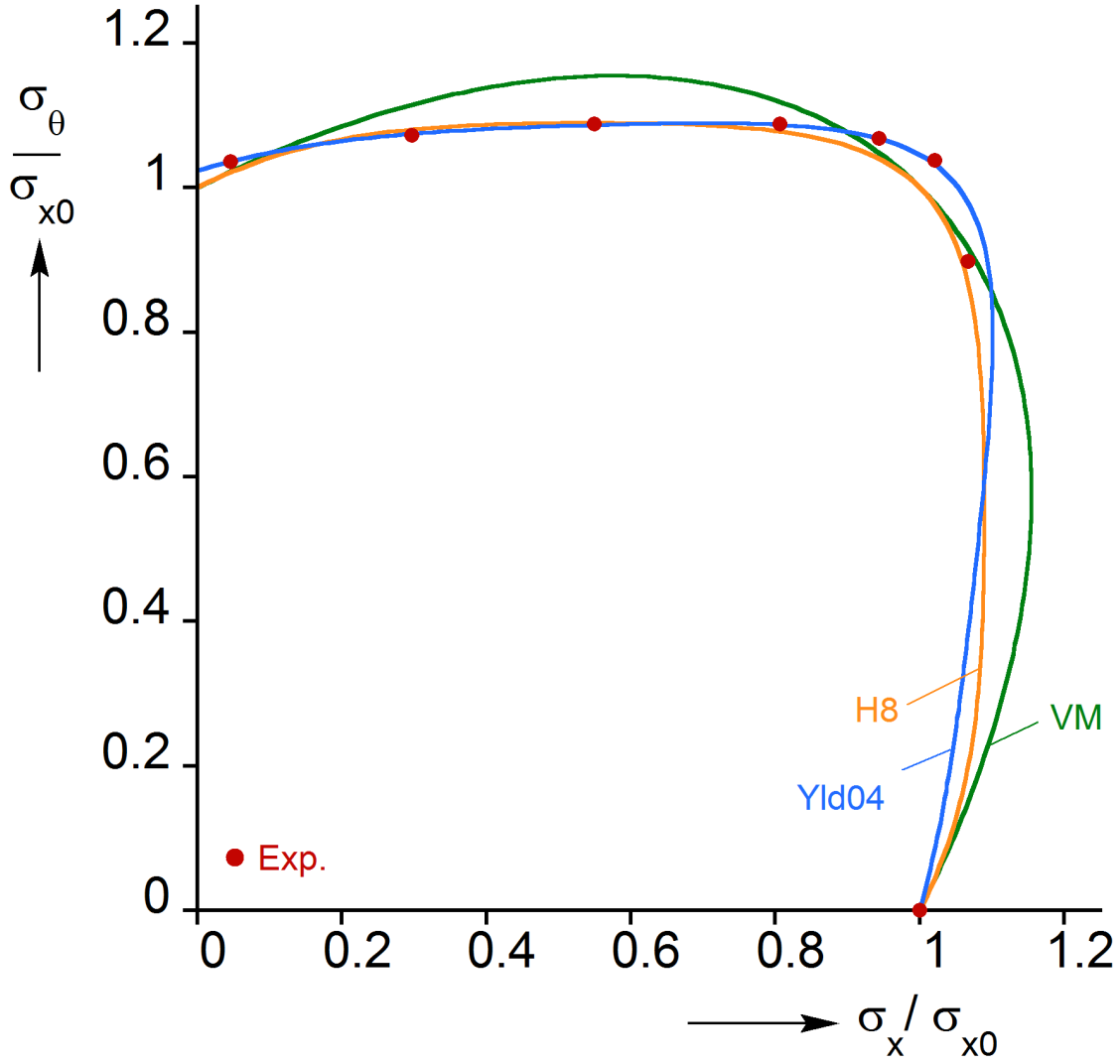

Figure 5.8: Work contours of the Von Mises, Hosford (8), and calibrated Yld04-3D constitutive models in the axial-hoop stress space. Experimental data points also included.

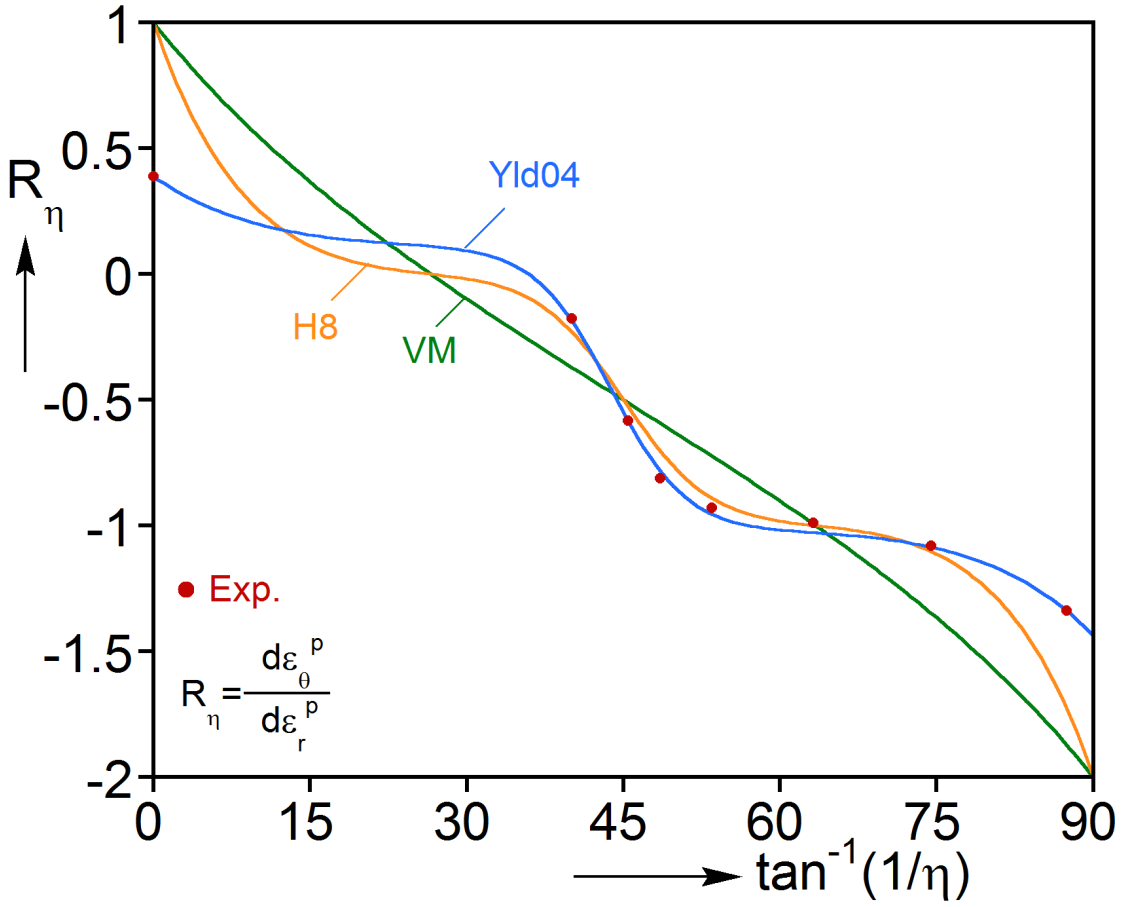

Figure 5.9: Work contours of the Von Mises, Hosford (8), and calibrated Yld04-3D constitutive models in the axial-hoop stress space. Experimental data points also included.

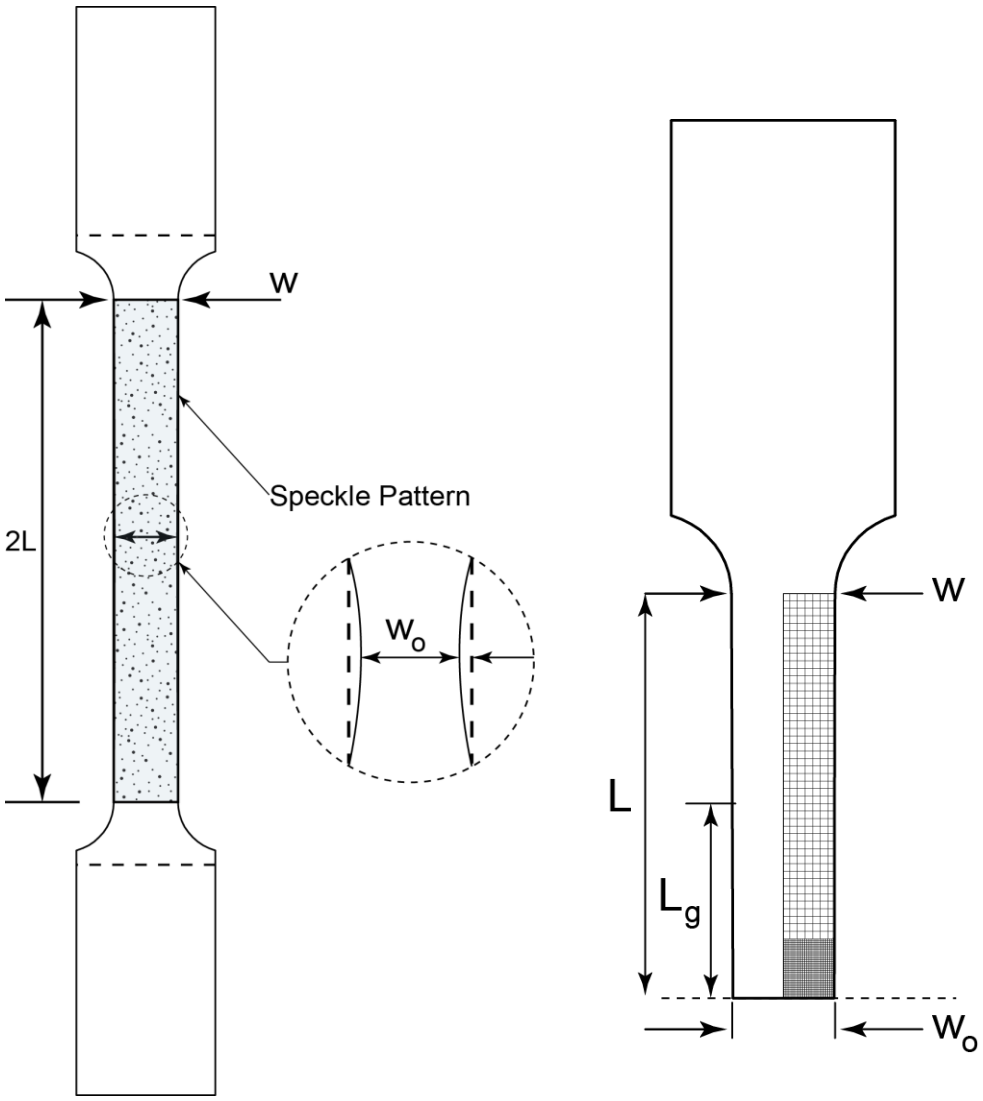

(a) (b)

Figure 5.10: (a) Scematic of the uniaxial tension specimen extracted from the tubes used in PT experiments. (b) Illustration of the mesh adopted for the finite element model used in the extraction of the stress-strain curve. (Note: L = 1.5 inches, L_g = 1 inch, w_o = 0.365 inches)

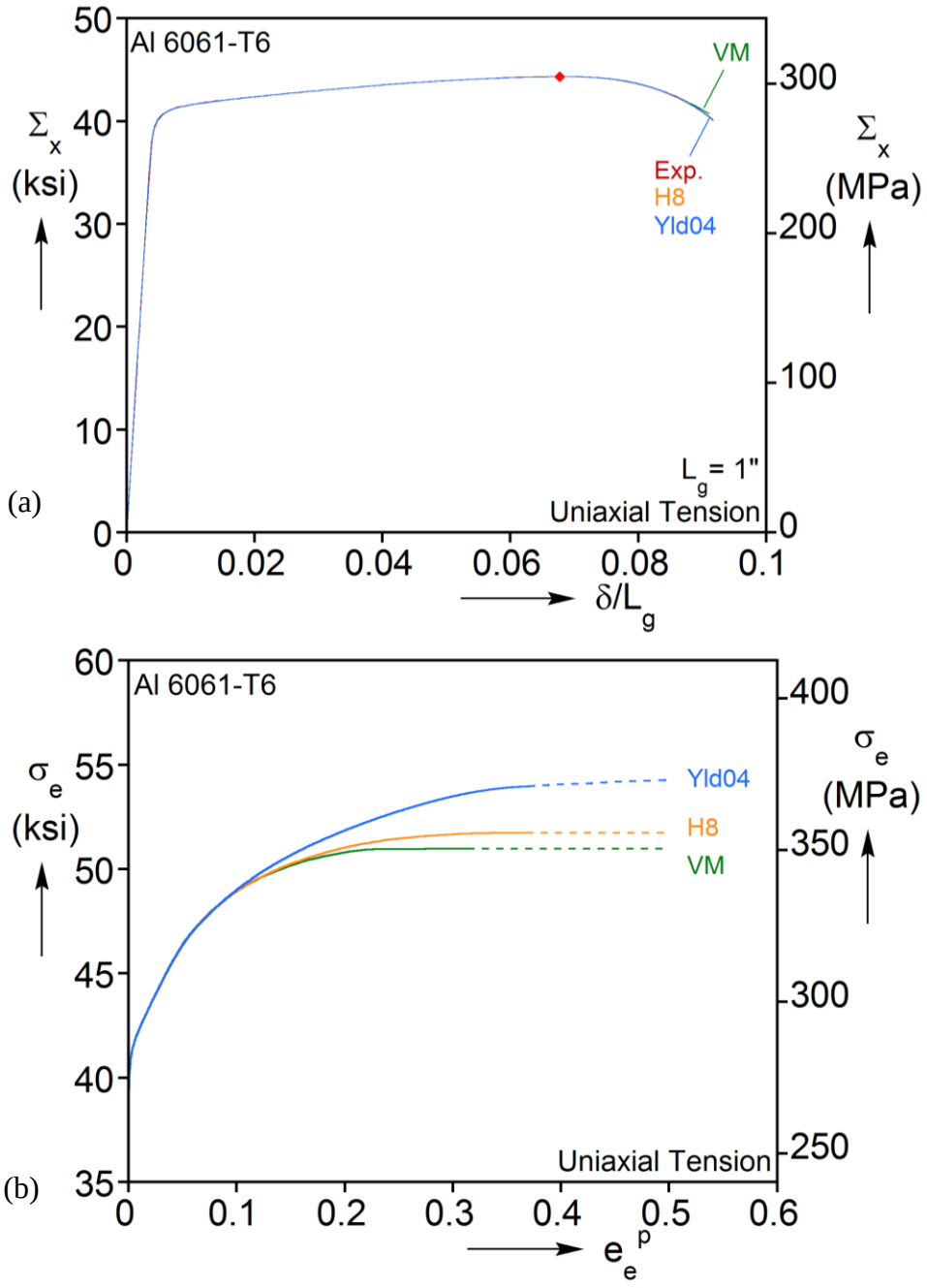

Fig. 5.11: (a) Nominal stress-strain responses measured in the experiment and reproduced by the three constitutive models. (b) Extracted true stress-plastic strain curves for the three constitutive models.

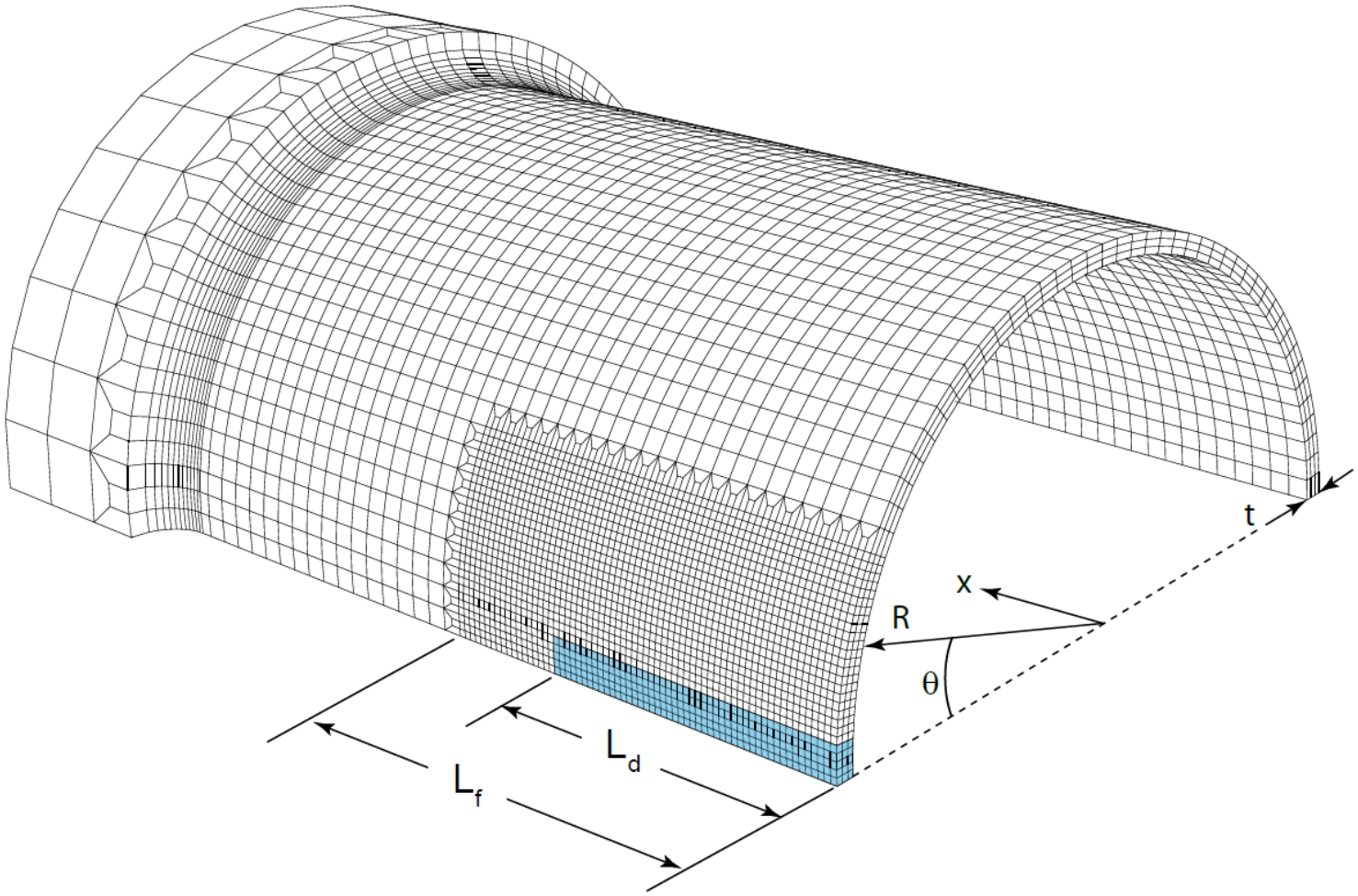

Fig. 5. 12: Finite element mesh adopted for simulation of PT experiments.

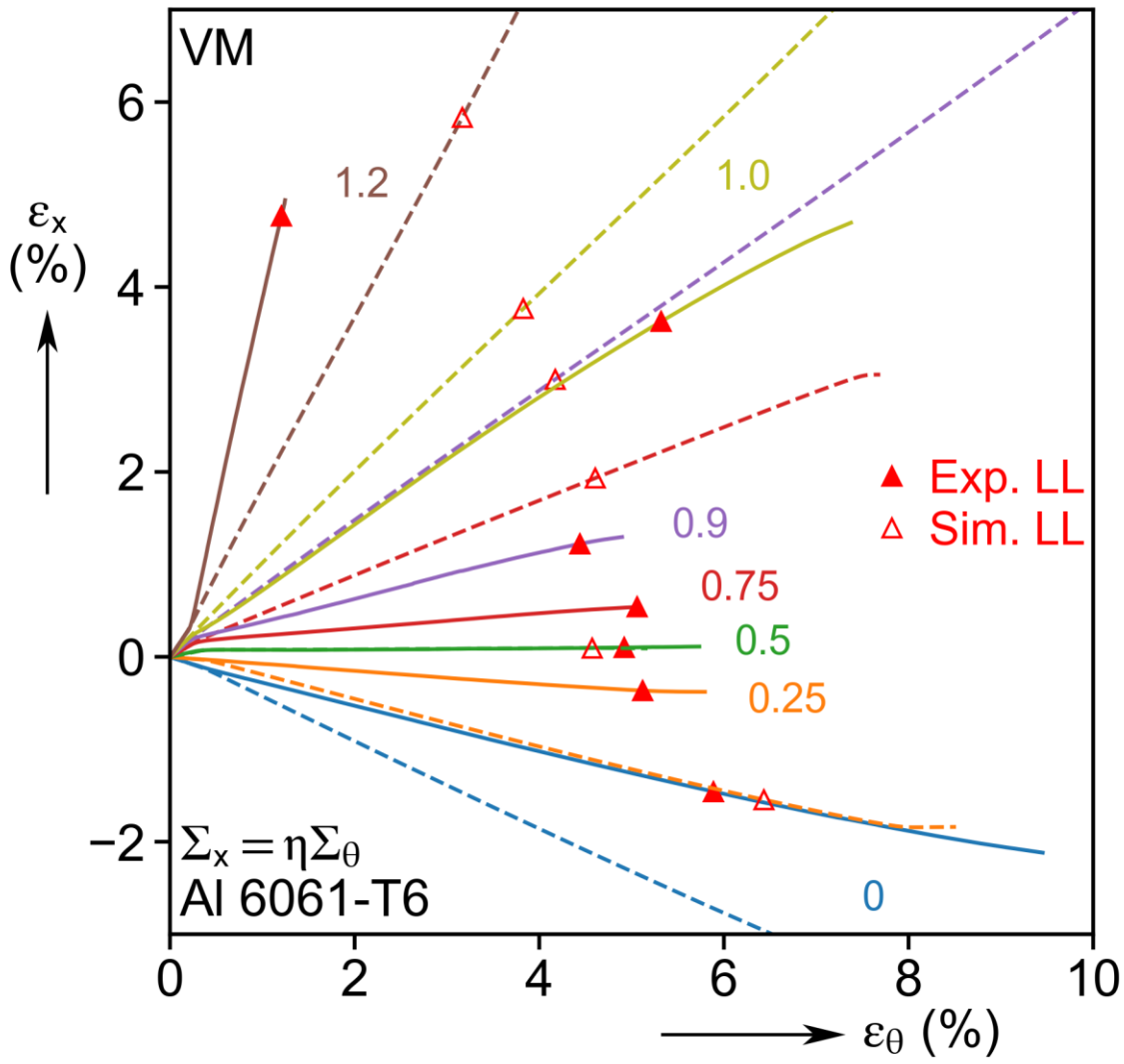

Fig. 5. 13: (a) Average strain histories for the set of PT experiments and simulations using the VM constitutive model. Experiments are plotted in solid lines, simulations in dashed lines.

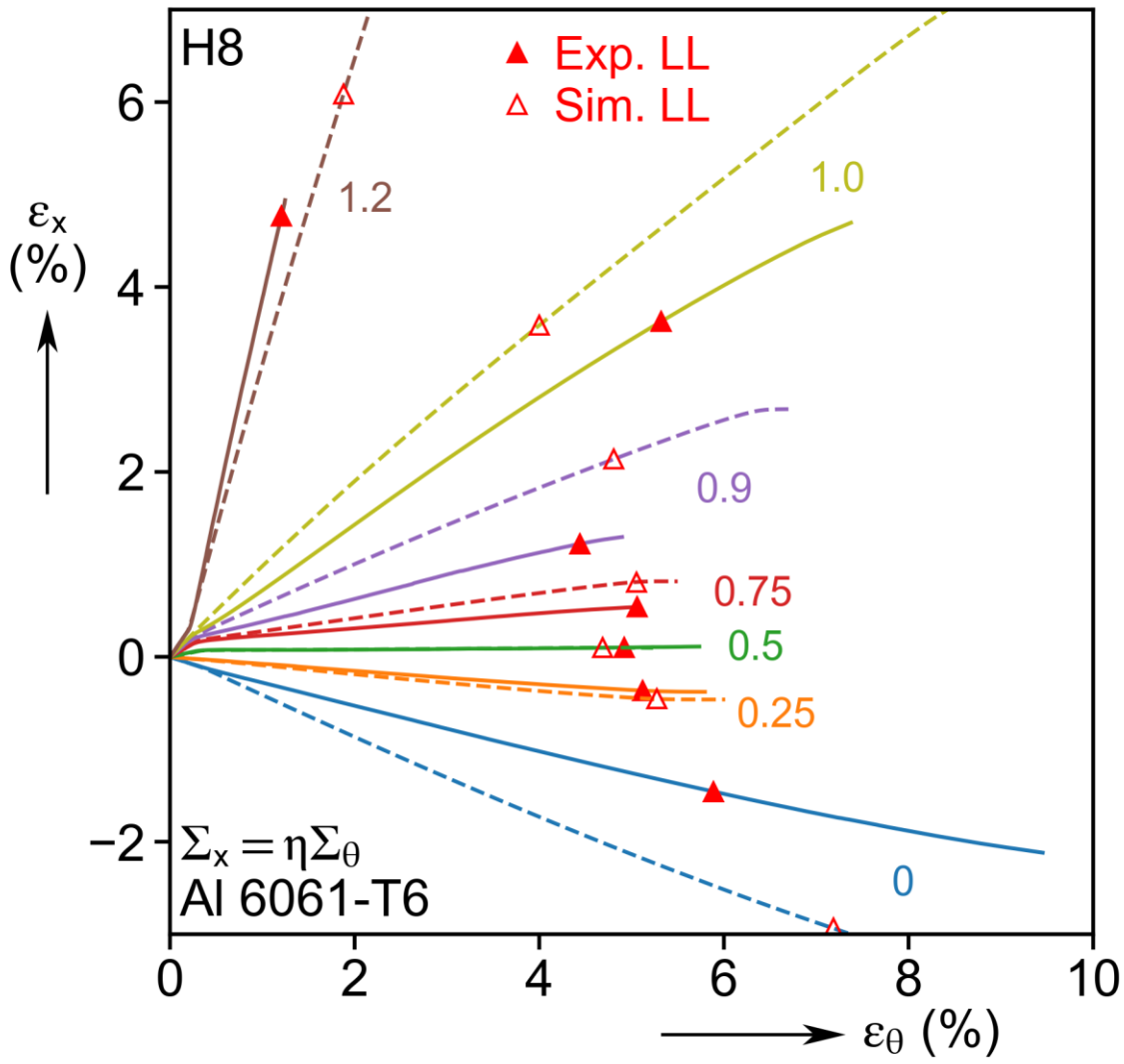

Fig. 5. 13: (b) Average strain histories for the set of PT experiments and simulations using the H8 constitutive model. Experiments are plotted in solid lines, simulations in dashed lines.

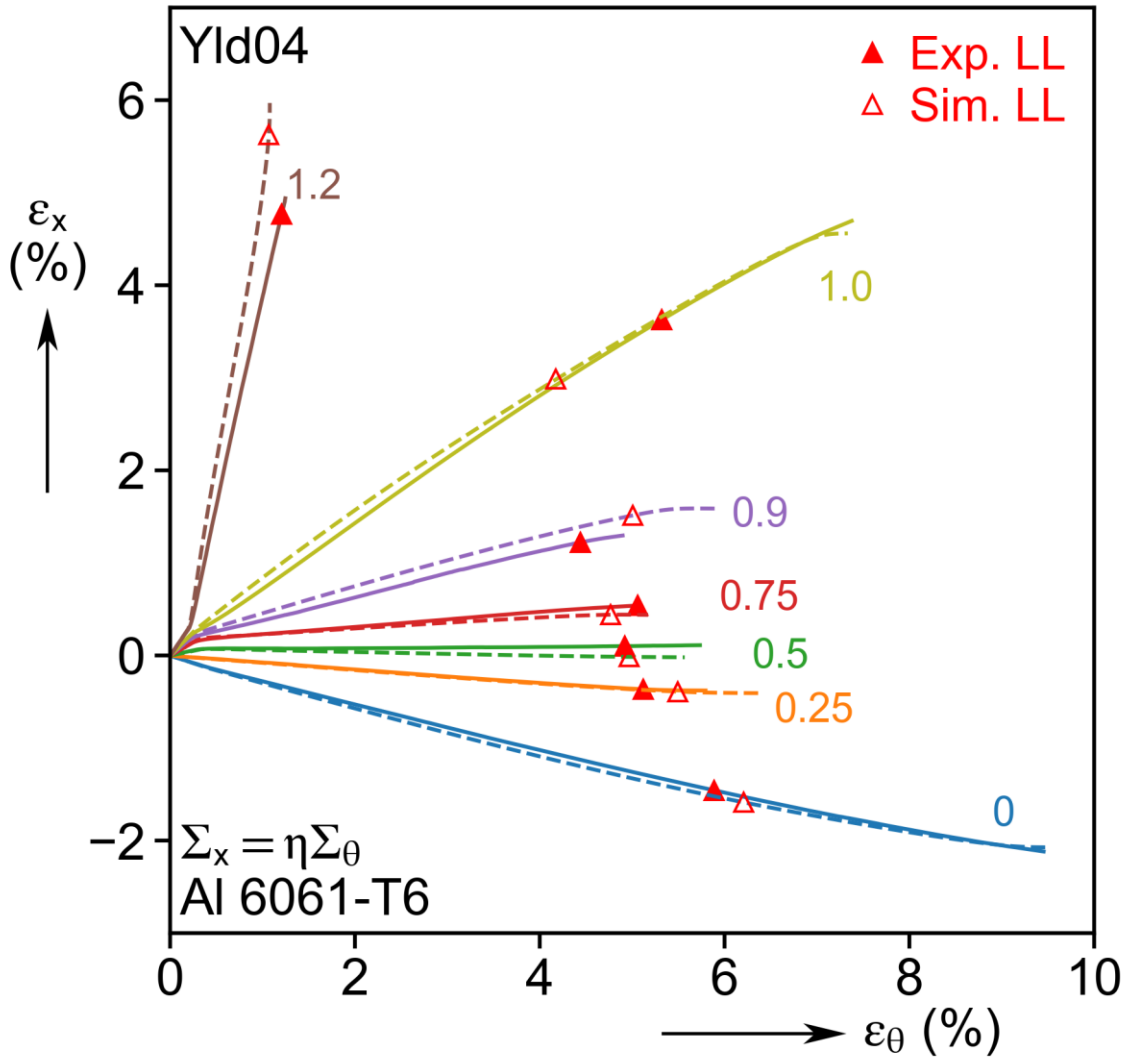

Fig. 5. 13: (c) Average strain histories for the set of PT experiments and simulations using the Yld04 constitutive model. Experiments are plotted in solid lines, simulations in dashed lines.

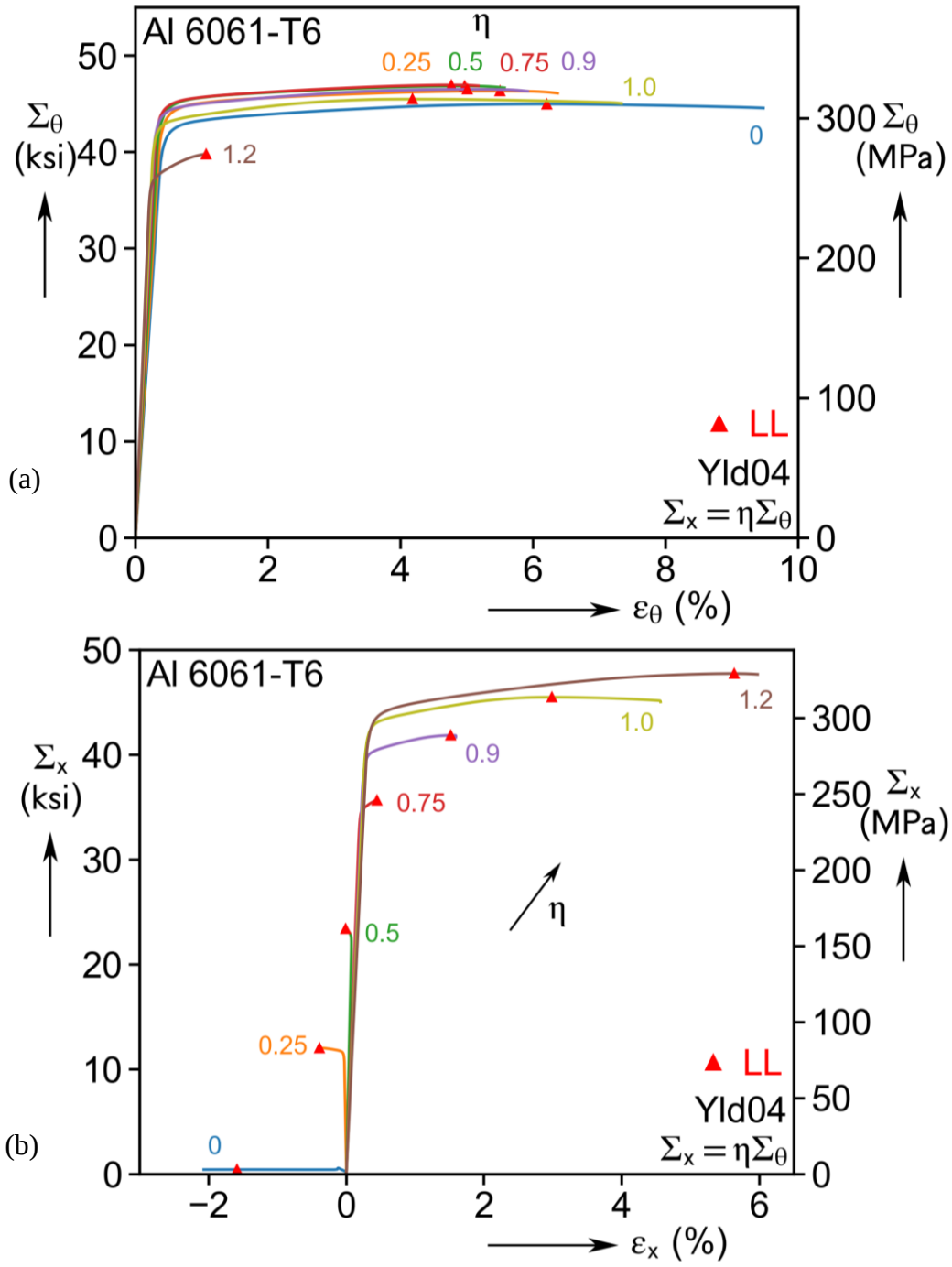

Fig. 5.14: (a) Hoop stress-strain responses predicted using the Yld04-3D constitutive model. (b) Corresponding axial stress-strain responses.

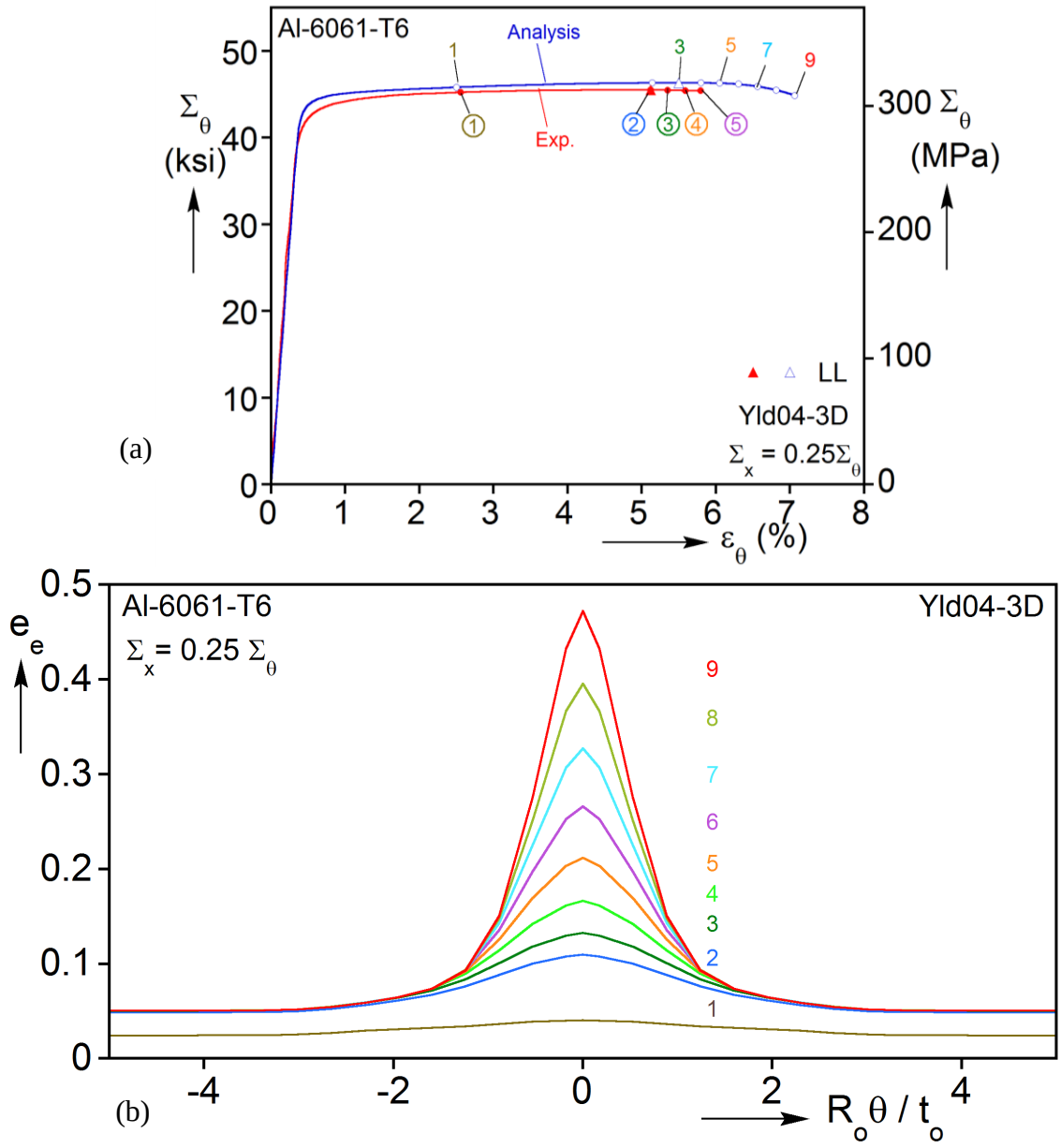

Fig. 5.15: (a) Nominal hoop response for $\eta = 0.25$ experiment and Yld04 analysis. (b) Localization profiles predicted by the Yld04 model at the nine stations marked in (a). Note that station ③ corresponds to the limit load in the analysis.

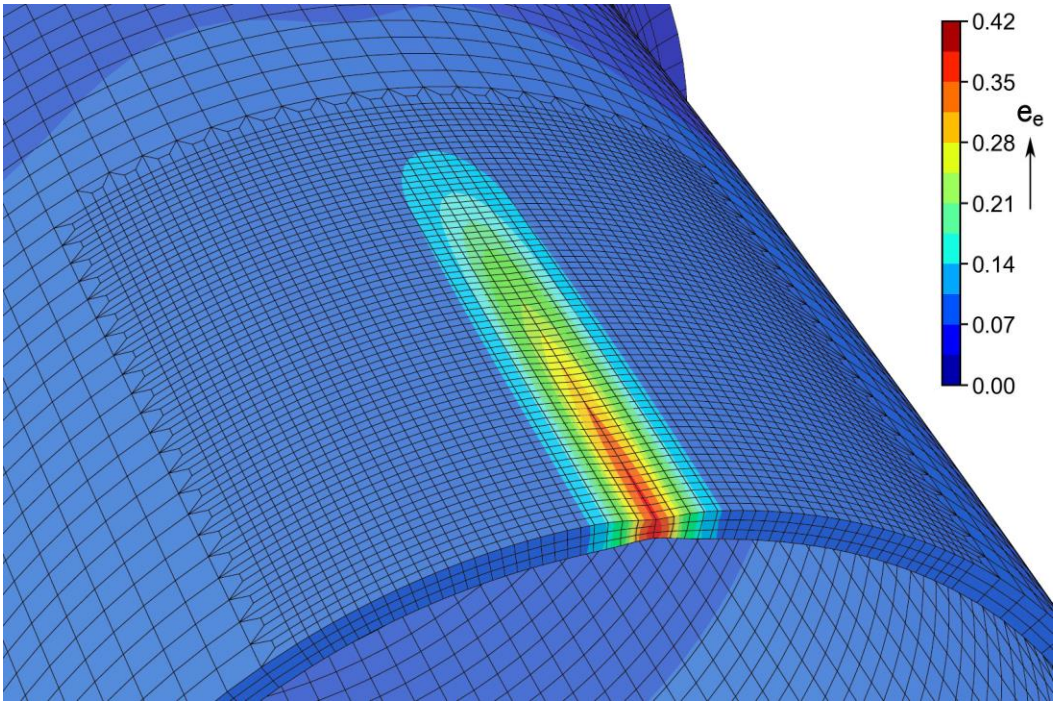

Fig. 5.15: (c) Close-in view of the localization in the Yld04 FE model for η = 0.25 at station ⑨ marked in 5.15(a).

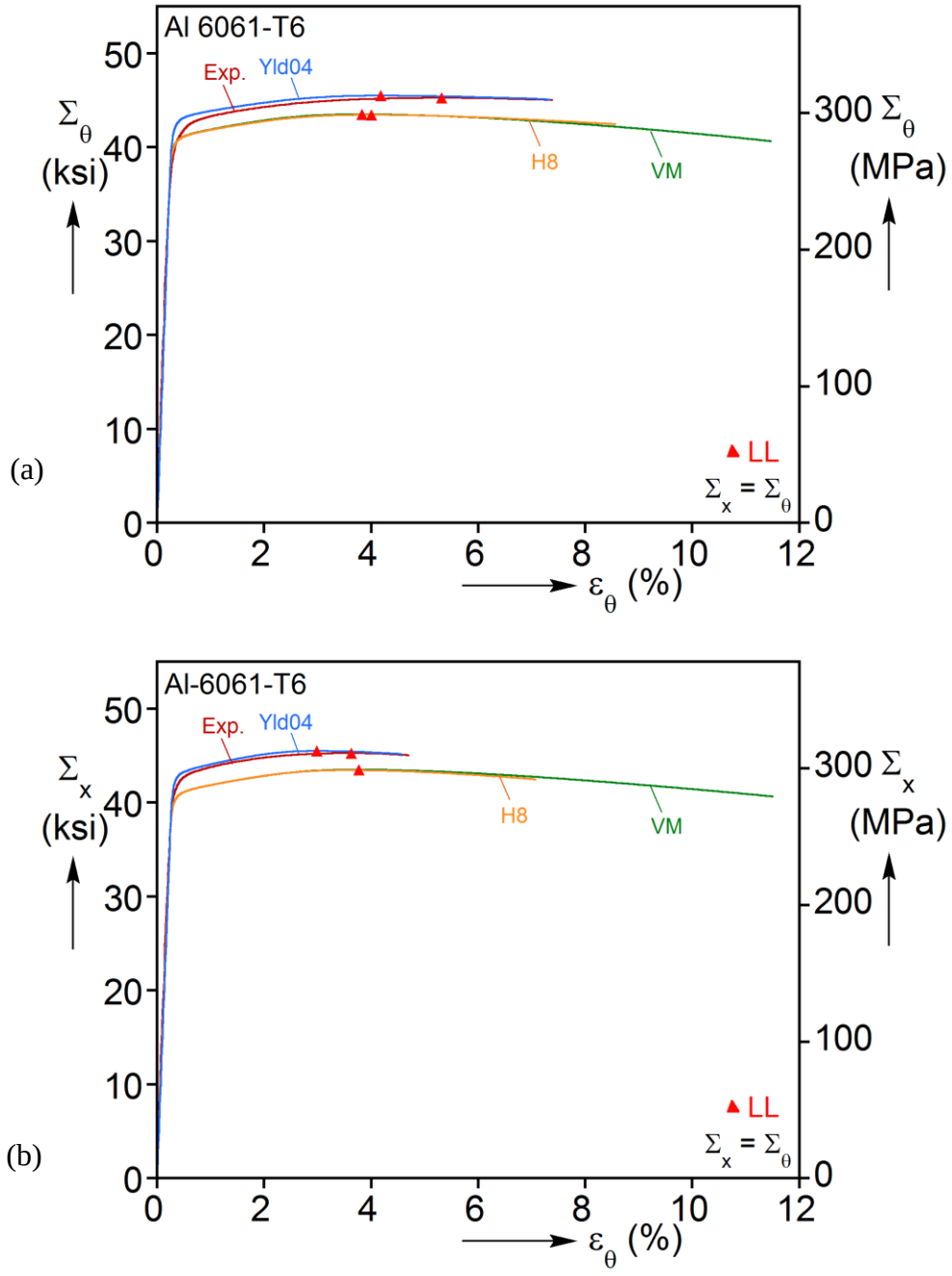

Fig. 5.16: (a) Measured (Exp.) and predicted (Yld04, H8, VM) hoop stress-strain response for $\eta = 1.0$. (b) Corresponding axial stress-strain responses.

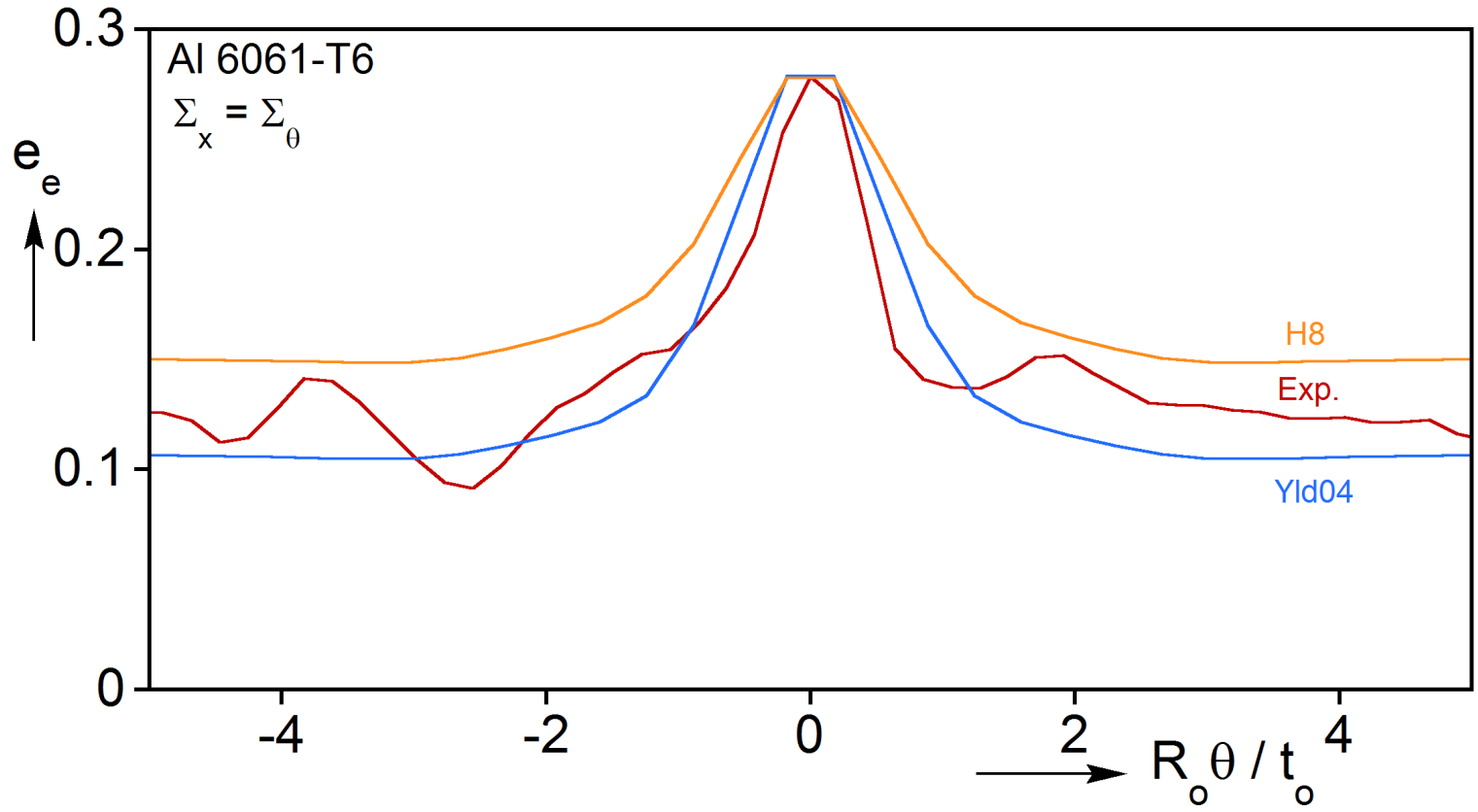

Fig. 5.17: Equivalent strain profile across the localizing zone as measured in the experiment, and reproduced numerically by the H8 and Yld04 models.

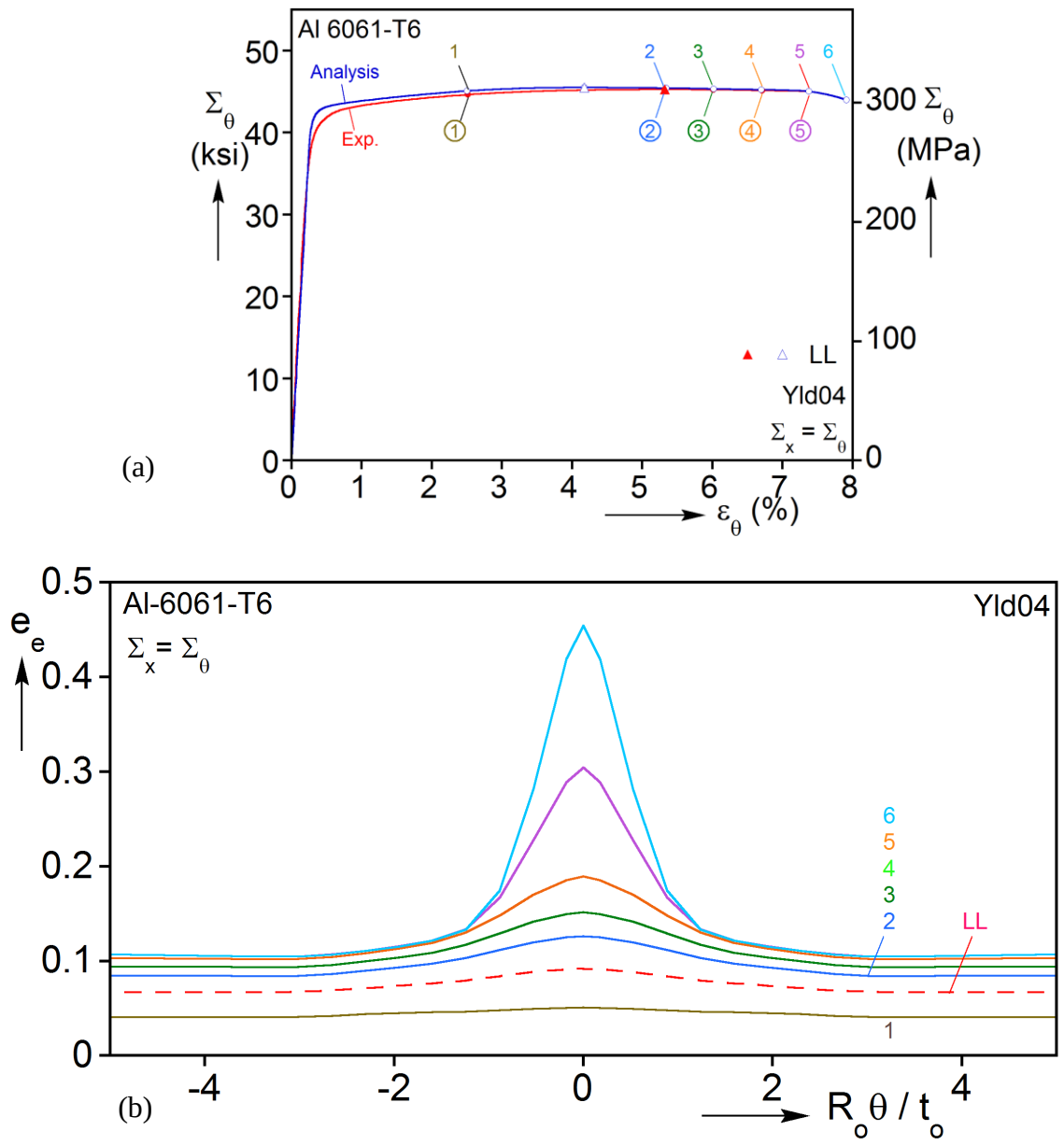

Fig. 5.18: (a) Nominal hoop response for $\eta = 1.0$ experiment and Yld04 analysis. (b) Localization profiles predicted by the Yld04 model at the nine stations marked in (a). The profile corresponding to the pressure maximum is plotted as a dashed line.

Chapter 6: Conclusions and Future Work

6.1: TENSION-TORSION

Progress towards a better understanding ductile failure in metals has been made in the past 15 years since Bao and Wierzbicki [2004] reported a non-monotonic trend in failure with triaxiality, which led to a renewed interest in the subject. Yet there remains significant discord in the research community. The confusion stems, in our judgement, from a lack of reliable experimental data on which failure models are based. Most current experimental work involves hybrid analysis in which either the stress and/or strain are extracted from numerical simulation. For these simulations, practitioners adopt a constitutive model and material stress-strain curve that have profound effects on the results of their predictions. The mere fact that the nominal structural response matches the experiment does not prove that their predicted local stresses and strains are accurate.

With this in mind, the primary objective of this work was to develop robust experimental methods through which a material's ductile failure characteristics can be established. The experiments were developed with the following objectives:

- Stresses and strains, or accurate estimates thereof, should be established directly from experimental measurements, without resorting to numerical simulation.
- The material should be sufficiently free of constraints such that it can undergo localization prior to failure.
- The localized deformations must be directly observable.

These criteria were satisfied through the combined tension and torsion (TT) experiments whose setup was detailed in Chapter 2, and results detailed in Chapters 3 and 4. The key to this experimental series is the specimen design, which features a thin-walled test section that is ten-times longer than it is thick, and a radius-to-

thickness ratio of about 22. This test section geometry allows the nominal stresses to be established directly from the applied force and torque.

The use of high-resolution of 3D digital image correlation (DIC) system enabled tracking the development of narrow bands of localized deformation that developed prior to failure in the experiments. We measured failure strains for Al 6061-T6 that were significantly greater than what had been previously reported for the same alloy, with values approaching 1.5 at low triaxiality. More importantly, our measured failure strains decreased monotonically with increasing triaxiality in the range $0.072 \leq \sigma_{mf}/\sigma_{ef} \leq 0.577$, which unequivocally refutes one of the key findings of Bao and Wierzbicki [2004] and for the same alloy in Beese et al. [2010].

In our first series of experiments, the equivalent strains at failure were calculated according to the total von Mises equivalent strain through the principal stretches. The motivation behind this method was to present as clear a result as possible, without introducing the complication of constitutive models. In a second series of experiments conducted in support of a separate numerical effort, the equivalent strain was more accurately computed by integrating the work-compatible equivalent plastic strain increments. The difference in the calculated failure strain between the two methods was insignificant at moderate and higher triaxialities, but the incremental strains were of order 10% greater than the total strains at the lowest triaxialities studied.

This incremental method required introduction of an equivalent stress and corresponding constitutive model. Three constitutive models were evaluated: von Mises, non-quadratic Hosford with exponent $k = 8$, and the anisotropic, non-quadratic constitutive model of Barlat et al. [2005]. The difference in failure strains based on the three constitutive models was minor across the whole range of triaxiality. The adopted constitutive model, however, also resulted in modest changes in triaxiality through a

different hoop stress and equivalent stress. These minor differences did not however affect the monotonic trend between failure strain and triaxiality. Thus it can be said that for the purposes of evaluating the experimental data alone, the choice of constitutive model is not significant for this alloy.

Our results should be considered while keeping in mind that the material undergoes this significant deformation without any observable void growth or accumulation of damage. X-ray tomography of material that had been extracted from near the failure zone in one of our test specimens revealed only a slight increase in porosity, and micrographs previously analyzed in Haltom et al. [2013] showed no damage in the vicinity of the cracks. These findings for Al 6061-T6 were consistent with those of Ghahremaninezhad and Ravi-Chandar [2013] and Gross and Ravi-Chandar [2016]. Therefore, we conclude that the reduction in stiffness and localization that we find in our experiments is primarily the result of plasticity and structural instability. For this material, suitably-calibrated incremental plasticity alone ought to be sufficient for numerically reproducing these large deformations up to near failure (see Chen et al. [2019]). Damage-induced softening that is incorporated into constitutive models should therefore be applied with caution.

We make two primary assumptions in the analysis of the TT experiments to enable calculation of the stress state: (1) That there is zero circumferential strain, and (2) that the through thickness stress is negligible. The fact that we measure a small amount of radial contraction and that a 3D neck develops indicates that neither of these assumptions is exactly correct. The existence of a 3D neck also suggests that the stress and strain may not be uniform through the wall thickness. The aforementioned numerical simulations of these experiments will be able to shed more light on the validity of these assumptions.

6.2: PRESSURE-TENSION

Due to the long, uniform, thin-walled test section of the TT specimens, the biaxial stresses and strains developed facilitate the calibration of material anisotropy. Calibration of suitable anisotropic constitutive models for numerical simulation of the TT experiments required a broader set of stress states, however. Thus the calibration data were enriched with a set of axial-hoop stress states through a series of combined tension and internal pressure experiments.

The use of 3D DIC in these experiments enabled monitoring of localized instabilities that developed following the pressure maximum. The measured strains inside these zones are not representative of the true failure strains due to the sudden failure by burst. Nevertheless, the results demonstrate once again that with an appropriate specimen design and suitable diagnostic technique, ductile materials will undergo localization prior to failure, and any estimate of failure strain that does not take this fact into account is likely inaccurate.

The seven radial-path PT tests and one uniaxial tension test on a dogbone specimen machined from the same tubes were used to calibrate Barlat's Yld04-3D anisotropic constitutive model. A finite element (FE) model of the PT experiment was developed that included the calibrated anisotropy. The model also includes the material hardening response that was inversely extracted from the post-necking regime of a uniaxial tension test. Each radial-path PT experiment was simulated numerically. The FE model that includes the anisotropy reproduced the nominal responses and strain histories exceedingly well, while FE models using Hosford-8 and von Mises failed to accurately predict the strain histories and pressure maxima. The anisotropic model also accurately reproduced the post-pressure maximum localization in all cases, while the two isotropic models did not perform as well. The results highlight the supreme importance of properly establishing material

anisotropy and hardening in analyses that involve large, localized deformations. The success of the numerical PT analyses is consistent with our contention that these same components (calibrated plasticity, an accurate hardening response, and a suitable FE mesh) are sufficient for numerically reproducing large deformations observed in the TT experiments.

6.3: FUTURE WORK

This work is a first step towards developing reliable experimental methods for characterizing ductility. As such, our TT program covered a relatively-narrow range of triaxiality. The PT experiments extended to a slightly higher triaxiality of 0.67 (equibiaxial tension), though these experiment did not offer a reliable measure of the strain at failure. New experimental programs are needed to expand the stress-state that can be explored through experiment. The development of such programs is complicated by the fact that triaxialities greater than 0.67 involve 3D stress states, making direct measurement of these quantities quite challenging.

3D digital volume correlation (DVC) has been used recently (Morgeneyer et al [2014], Buljac et al. [2016]) to assess the evolution of damage and measure the 3D strain field, and is a promising technological step forward. Its use, however, is constrained by the practical aspects of performing in-situ experiments in the presence of radiation. With continued development DVC could become a useful experimental tool.

In the absence of diagnostic techniques that can establish the full 3D stress and strain state, researchers will have to continue to turn towards numerical modeling. Micro-mechanical models that attempt to capture void growth and coalescence are still relatively young and are far from finding use outside of academic settings. Therefore, well-calibrated plasticity likely remains the most reliable approach for modeling large deformations and

localization. While in this work an experimentally-intensive approach was taken to establish material anisotropy and hardening, techniques such as the virtual fields method (see, for example, Rossi et al. [2016]) are emerging which may provide this information at considerably less effort.

Appendices

APPENDIX A: MICROSTRUCTURE

Aluminum 6061-T6 is a precipitation-hardened alloy with primary alloying agents Silicon and Magnesium. The material produced by Kaiser Aluminum, which was used in the tension-torsion experiments of Chapter 4 and pressure-tension experiments of Chapter 5, has the following composition:

Table A.1: Al 6061-T6 chemical composition

Si	Fe	Cu	Mn	Mg	Cr	Zn	Ti
0.59	0.26	0.23	0.05	0.99	0.10	0.05	0.02

The undeformed grain morphology of these was assessed via Electron Back Scattering Diffraction (EBSD) analysis. Both of the scans discussed below were conducted on material extracted from a tube that had been machined but never loaded. Results from a scan in the θ-x plane over an area of approximately 4 mm x 4 mm are presented in Fig. A.1 (a). The images were processed in ImageJ and ellipses were fit to 540 grains. Distributions of the fitted major and minor ellipse diameters ($2a$ and $2b$) and angle of orientation (θ) relative to the axial direction are presented in Figs. A.1 (b) and (c). The mean major and minor diameters are 148 and 88 μm and have standard deviations of 80 and 51 μm respectively.

A through-thickness scan (r-x plane) of a specimen is presented in Fig. A.2 (a). The scan is roughly 7 mm in length and covers the entire wall-thickness. Note however that due to edge effects some of the material along the OD and ID was unscannable, and therefore the image shown is only about $0.8t_o$ wide. A statistical analysis like the one described above for the entire through-thickness scan shows a mean major and minor diameter of are

178 and 60 μm (Fig. A.2 (b) and (c)). Thus these grains, on average, are longer and narrower through-thickness than they are in the θ-x plane.

It is readily apparent from visual inspection of this scan that two distinct grain-size regimes exist: the grains along the ID are significantly larger than those along the OD. Recall that the ID surface of the test specimens *are not* machined and are therefore the original extrusion surface. Such texture gradients are known to exist in extruded aluminum alloy products (e.g., Khadyko et al. [2016]), but their effect on the mechanical behavior of the material remains unclear.

It is also worth noting that these grains are larger than what was found in the materials tested in Haltom et al. [2013] and Scales et al. [2016], which had average major and minor diameters of 33 μm and 20 μm (see Fig. 16 of Haltom et al. [2013]). Despite this difference, the yield stress, hardening, and failure strains for these two sets of Al 6061-T6 were similar. This indicates that that precipitates play a larger role than the grain size distribution in these mechanical properties.

(a)

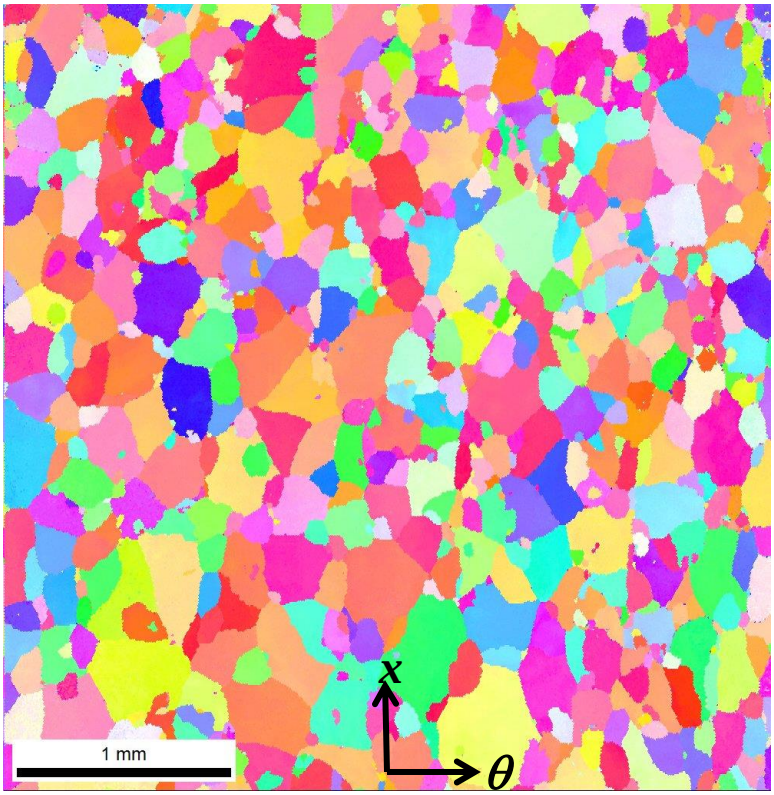

Fig. A.1: (a) EBSD scan of undeformed material extracted from a machined but untested specimen (*q*-*x* plane).

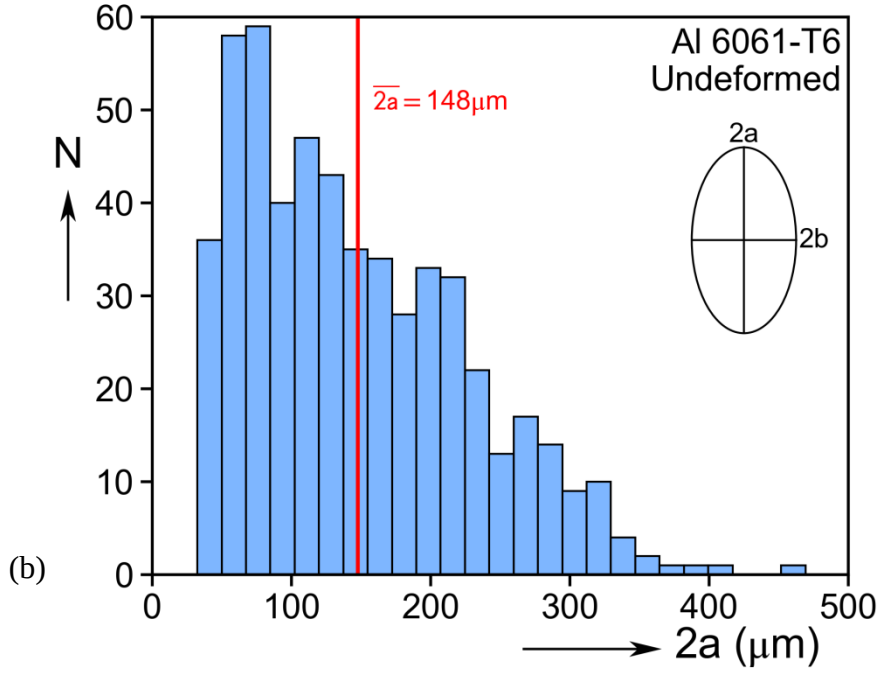

(b)

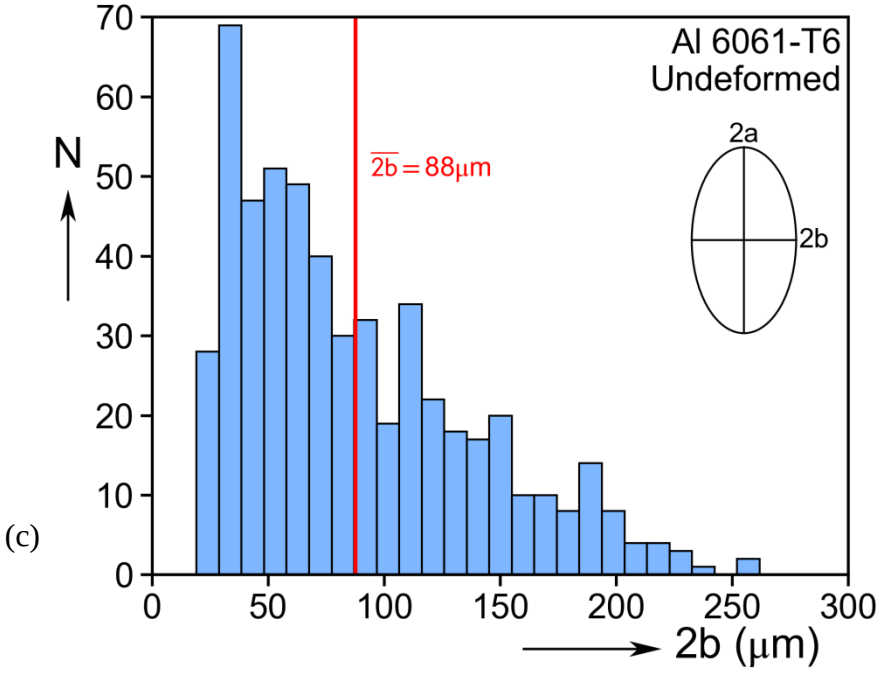

(c)

Fig. A.1: (b) Distribution of major axes of ellipses fit to the grains in (a).
(c) Distribution of minor axes.

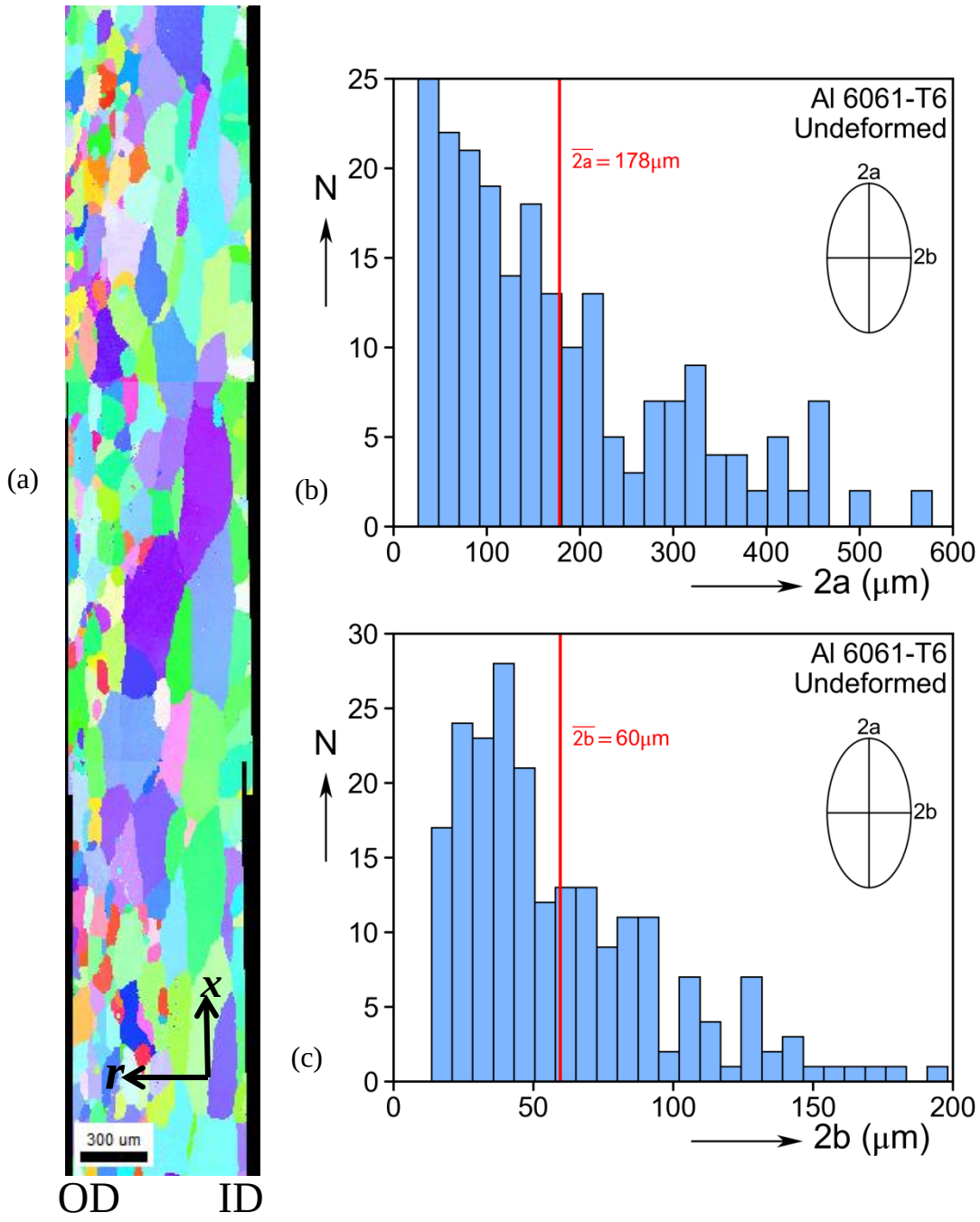

Fig. A.2: (a) EBSD scan through the test section wall thickness (*r*-*x* plane). (b) Distribution of major axes of fitted ellipses. (c) Minor axes.

APPENDIX B: IMPERFECTION SENSITIVITY OF PRESSURE-TENSION FINITE ELEMENT MODEL

Results presented in Chapter 5 employed a 3% wall thickness imperfection ($\Delta t/t_o$) in the finite element model. This value was chosen for the presentation of the results as it agreed well with experimental observations. This value is also well within some of the variability in wall thickness measured in the test specimens. Recall that the inner-diameter of the tubes along the test section were not machined.

Figure B.1 presents the nominal hoop and axial stress-strain responses for experiment PT-8 with η = 1.0. Included also are the results of three numerical simulations, all of which employ the Yld04 anisotropic constitutive model, but have imperfection magnitudes of 1%, 2%, and 3%. The results demonstrate that the effect of the imperfection on the strain at the limit load is not very significant. These strains are reported in Table B.1 below. In contrast, however, the onset of localization is apparently quite sensitive, with the strain components at the onset of failure (associated with the downturn in the response) increasing substantially with each decrease in the imperfection magnitude. Thus this result reinforces the fact that localization and failure are highly sensitive to the local imperfections and geometry.

Table B.1: Strains at the pressure maximum for η = 1.0

	ε_{xL} (%)	$\varepsilon_{\theta L}$ (%)
Exp.	3.63	5.32
1%	2.96	4.02
2%	2.97	4.07
3%	2.99	4.18

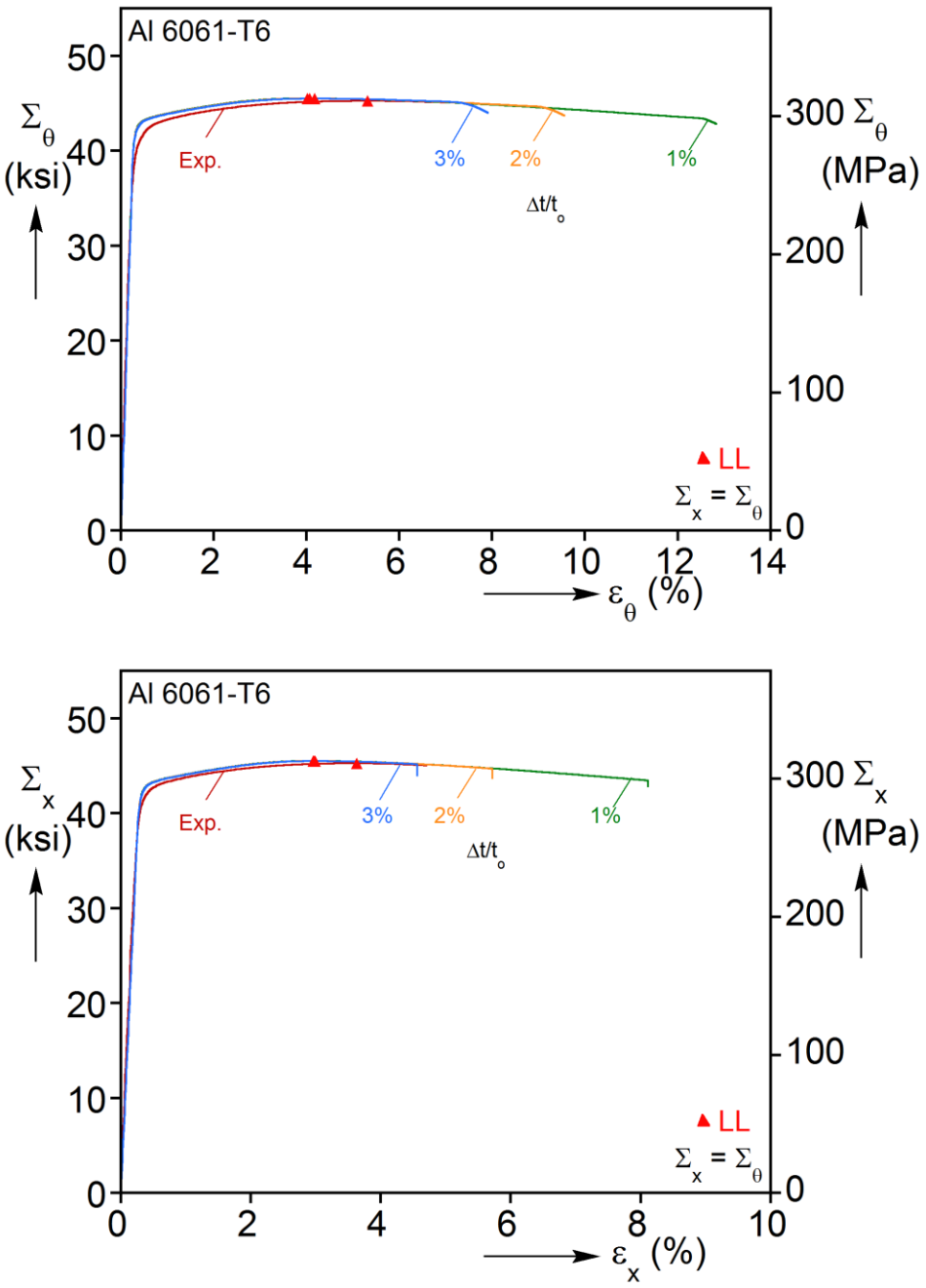

Figure B.1: (a) Nominal hoop stress-strain response of experiment with $\eta = 1.0$ and corresponding simulations using the Yld04 constitutive model, each with a difference imperfection magnitude. (b) Corresponding axial responses.

References

ABAQUS (2016), ABAQUS Theory Guide. Dassault Systems Simulia Corp., Providence, RI.

ARAMIS User Manual-Software. GOM Optical Measuring Techniques, 23 May 2011. PDF

Bai, Y.L. and Wierzbicki, T. (2008). A new model of metal plasticity and fracture with pressure and Lode dependence. *Int'l J. Plast.* **24**, 1071-1096.

Bai, Y.L. and Wierzbicki, T. (2010). Application of extended Mohr-Coulomb criterion to ductile fracture. *Int'l J. Fracture* **161**, 1-20

Bao, Y.-B. and Wierzbicki, T. (2004). On fracture locus in the equivalent strain and stress triaxiality space. *Int'l J. Mech. Science* **46**, 81-98.

Barlat, F., Aretz, H., Yoon, J.W., Karabin, M.E., Brem, J.C., Dick, R.E. (2005). Linear transformation-based anisotropic yield functions. *Int'l J. Plasticity* **21**, 1009-1039.

Barsoum, I., Faleskog, J. (2007a). Rupture mechanisms in combined tension and shear–Micromechanics. *Int'l J. Solids Struct.* **44**, 5481-5498.

Barsoum, I., Faleskog, J. (2007b). Rupture mechanisms in combined tension and shear–Experiments. *Int'l J. Solids Struct.* **44**, 1768-1786.

Beese, A.,M., Luo, M., Li, Y., Bai, Y., Wierzbicki, T. (2010). Partially coupled anisotropic fracture model for aluminum sheets. *Eng. Fract. Mech.* **77**, 1128-1152.

Bridgman, PW (1944). The stress distribution at the neck of a tension specimen. *Trans. Am. Soc. Met.*, **32**, 553-574..

Brown, W.F. and Sachs, G. (1948). Strength and failure characteristics of thin circular membranes. *Transactions of the ASME* **70**, 241-251.

Brünig, M., Brenner, D., Gerke, S., (2015). Stress state dependence of ductile damage and fracture behavior: Experiments and numerical simulations. *Eng. Fract. Mech.* **141**, 152-169.

Brünig, M.,Gerke, S.,Schmidt, M., (2016). Biaxial experiments and phenomenological modeling of stress-state-dependent ductile damage and fracture. *Int'l. J. Fract.* **200**, 3–76.

Buffiere, J.-Y , Maire, E. , Ardien, J. , Masse, J.-P. , Boller, E. , (2010). In situ experiments with X ray tomography: An attractive tool for experimental mechanics. *Exp. Mech*. **50**, 289–305 .

Buljac, A., Taillandier-Thomas, T., Morgeneyer, T., Helfen, L., Roux, S., Hild, F. (2016). Slant strained band development during flat to slant crack transition in AA 2198 T8 sheet: in situ 3D measurements. *Int'l J. Fract.* (in press DOI 10.1007/s10704-015-0052-z)

Chen, K., Scales, M., Kyriakides, S., Corona, E. (2016). Effects of anisotropy on material hardening and burst in the bulge test. *Int'l J. Solids Struct.* **82**, 7-84.

Chen, K., Scales, M., Kyriakides, S., (2018a). Material hardening of a high ductility aluminum alloy from a bulge test. *Int'l J. Mech. Sci.* **138-139**, 476-488.

Chen, K., Scales, M., Kyriakides, S., (2019). Material response, localization, and failure of an aluminum alloy under combined shear and tension: Part II Analysis. *Int'l J. Plast.* [in press]

Chu, C.C. , Needleman, A. , (1980). Void nucleation effects in biaxially stretched sheets. *J. Eng. Mater. Technol. ASME* **102**, 249–256 .

Defaisse, C., Mazière, M., Marcin, L., Besson, J., (2018). Ductile fracture of an ultra-high strength steel under low to moderate stress triaxiality. *Eng. Frac. Mech*. **194**, 301-318.

Driemeier, L., Brünig, M., Micheli, G., Alves, M., (2010). Experiments on stress-triaxiality dependence of material behavior of aluminum alloys. *Mech. Mat.* **42**, 207-127.

Dunand, M., Mohr, D. (2010). Hybrid experimental-numerical analysis of basic ductile fracture experiments for sheet metals. *Int'l J. Solids Struct.* **47**, 1130-1143.

Dunand, M., Mohr, D. (2011). Optimized butterfly specimen for the fracture testing of sheet materials under combined normal and shear loading. *Eng. Fract. Mech.* **78**, 2919-2934.

Faleskog, J., Barsoum, I. (2013). Tension-torsion fracture experiments-Part I: Experiments and a procedure to evaluate the equivalent plastic strain. *Int'l J. Solids Struct.* **50**, 4241-4257.

Gao, X., Zhang, T., Zhou, J., Graham, S., Hayden, M., Roe, C., (2011). On stress-state dependent plasticity modeling: Significance of the hydrostatic stress, the third invariant of stress deviator and the non-associated flow rule. *Int'l J. Plast.* **27**, 217-231.

Ghahremaninezhad, A. and Ravi-Chandar, K. (2012). Ductile failure behavior of polycrystalline Al 6061-T6. *Int'l J. Fracture* **174**, 177-202.

Ghahremaninezhad, A. and Ravi-Chandar, K. (2013). Ductile behavior in polycrystalline aluminum alloy Al 6061-T6 under shear dominant loading. *Int'l J. Fract.* **180**, 23-39.

Giagmouris, T. , Kyriakides, S. , Korkolis, Y.P. , Lee, L.-H. , (2010). On the localization and failure in aluminum shells due to crushing induced bending and tension. *Int. J. Solids Struct*. **47**, 2680–2692.

Graham, S., Zhang, T., Gao, X., Hayden, M. (2012). Development of a combined tension–torsion experiment for calibration of ductile fracture models under conditions of low triaxiality. *Int'l J. Mech. Sci.* **54**, 172-181.

Gross, A., Ravi-Chandar, K. (2015). On the extraction of elastic-plastic constitutive properties from three-dimensional deformation measurements. *ASME J. Applied Mechanics.* **82(7)**, 071013.

Gross, A., Ravi-Chandar, K. (2016). On the deformation and failure of Al-6061-T6 at low triaxiality evaluated through in-situ microscopy. *Int'l J. Fract.* **200**, 185-208.

Gurson, A.L. (1977). Continuum theory of ductile rupture by void nucleation and growth: Part I– Yield criteria and flow rules for porous ductile media. *J. Eng. Mat. Tech.* **99**, 2–15.

Ha, J., Baral, M., Korkolis, Y. (2018). Plastic anisotropy and ductile fracture of bake-hardened AA6013 aluminum sheet. Int'l J. Solids Struct. [in press]

Haltom, S.S., Kyriakides, S., Ravi-Chandar, K. (2013). Ductile failure under combined shear and tension. *Int'l J. Solids & Structures* **50,** 1507-1522, 2013.

Hancock, J.W., McKenzie, A.C., (1976). On the mechanisms of ductile failure in high-strength steels subjected to multi-axial stress-states. *J. Mech. Phys. Solids.* **24**, 147-169.

Hill, R., (1990). Constitutive modeling of orthotropic plasticity in sheet metals. J. *Mech. Phys. Solids* **38**, 405–417.

Hosford, W.F. (1972). A generalized isotropic yield criterion. *ASME J. Applied Mechanics* **39**, 607-609.

Johnson, G.R. and Cook, W.H. (1985). Fracture characteristics of three metals subjected to various strains, strain rates, temperatures and pressures. *Eng. Fracture Mech.* **21**, 31-48.

Jones, E., Oliphant, E., Peterson P., *et al.* (2001). **SciPy: Open Source Scientific Tools for Python**. http://www.scipy.org/

Karafillis, A.P., Boyce, M.C., (1993). A general anisotropic yield criterion using bounds and a transformation weighting tensor. *J. Mech. Phys. Solids* **41**, 1859–1886.

Khadyko, M., Dumoulin, S., Hooperstad, O.S., (2016). Texture gradients and strain localization in extruded aluminum profile. *Int'l J. Solid Struct.* **97-98**, 239-255.

Korkolis, Y.P. and Kyriakides, S. (2008a). Inflation and burst of aluminum tubes part II: An advanced yield function including deformation-induced anisotropy. *Int'l J. Plasticity* **24**, 1625-1637.

Korkolis, Y.P. and Kyriakides, S. (2008b). Inflation and burst of anisotropic tubes for hydroforming applications. *Int'l J. Plasticity* **24**, 509-543.

Korkolis, Y.P., Kyriakides, S., Giagmouris, T., Lee, L.-H. (2010). Constitutive modeling and rupture predictions of Al-6061-T6 tubes under biaxial loading paths. *ASME J. Applied Mechanics* **77**:5, 064501, 1-5.

Kuwabara, T., Yoshida, K., Narihara, K., Takahashi, S. (2005). Anisotropic plastic deformation of extruded aluminum alloy tube under axial forces and internal pressure. *Int'l J. Plasticity* **21**, 101-117

Lesuer D.R., Kay, G.J., LeBlanc, M.M. (2001). Modeling large-strain, high-rate deformation in metals. UCRL-JC-134118, Lawrence Livermore National Laboratory.

Logan, R.W., Hosford, W.F., (1980). Upper-bound anisotropic yield locus calculations assuming <111>-pencil glide. *Int. J. Mech. Sci*. **22**, 419–430.

Maire, E. , Bouaziz, O. , Di Michiel, M. , Verdu, C. , (2008). Initiation and growth of damage in a dual-phase steel observed by X-ray microtomography. *Acta Mate* **56**, 4954–4964 .

McClintock, F.A., (1968). A criterion for ductile fracture by the growth of holes. *ASME J. Applied Mechanics.* **35(2)**, 363-371.

Mohr, D., Henn, S. (2007). Calibration of stress-triaxiality dependent crack formation criteria: a new hybrid experimental–numerical method. *Exp. Mech.* **47**, 805-820.

Mohr, D., Marcadet, S. (2015). Micromechanically-motivated phenomenological Hosford-Coulomb model for predicting ductile fracture initiation at low stress triaxialities. *Int'l J. Solids Struct*. **67-68**, 40-55.

Morgeneyer, T.F., Taillandier-Thomas, T., Helfen, L., Baumbach, T., Sinclair, I., Roux, S., Hild, F. (2014). In situ 3-D observation of early strain localization during failure of thin Al alloy (2198) sheet. *Acta Mat.* **69**, 78-91.

Nahshon, K. and Hutchinson, J.W. (2008). Modification of the Gurson model for shear failure. *Eur. J. Mech. A/Solids* **27**, 1-17.

Papasidero, J., Doquet, V., Mohr, D. (2014). Determination of the effect of stress state on the onset of ductile fracture through tension-torsion experiments. *Exp. Mechanics* **54,** 137-151.

Papasidero, J., Doquet, V., Mohr, D. (2015). Ductile fracture of aluminum 2014-T351 under proportional and non-proportional multi-axial loading: Bao-Wierzbicki results revisited. *Int'l J. Solids Struct.* **69-70**, 459-474.

Puttick, K.E., (1959). Ductile Fracture in Metals. *Philosophical Magazine, Series S* **4**, 964-969.

Rice, J.R. and Tracey, D.M. (1969). On the ductile enlargement of voids in triaxial stress fields. *J. Mech. Phys. Solids* **17**, 201-217.

Rossi, M., Pierron, F., Štamborská, M., (2016). Application of the virtual fields method to large strain anisotropic plasticity. *Int'l J. Solids Struct.* **15**, 322-335.

Saito et al., (2001). Development of aluminum bodies for fuel efficient vehicles. *Materials Today* **4**, 30-34.

Scales, M., Tardif, N., Kyriakides, S., (2016). Ductile failure of aluminum alloy tubes under combined torsion and tension. *Int. J. Solids Struct*. **97–98**, 116–128.

Scales, M., Chen, K., Kyriakides, S., (2019). Material response, localization, and failure of an aluminum alloy under combined shear and tension: Part I Experiments. *Int'l J. Plast.* [in press]

Shen, Y., Morgeneyer, T., Garnier, J., Allais, L., Helfen, L., Crepin, J., (2013). Three-dimensional quantitative in situ study of crack initiation and propagation in AA6061 aluminum alloy sheets via synchrotron laminography and finite-element simulations. *Acta Mat.* **61**, 2571-2582.

Suttner, S., Merkelein, M. (2016). Experimental and numerical investigation of a strain rate controlled hydraulic bulge test of sheet metal. *J. Mater. Proc. Tech.* **235**, 121-133.

Swift, H. W. (1952). Plastic instability under plane stress. *J. Mech. Phys. Solids* **1**, 1-18.

Tardif, N., Kyriakides, S. (2012). Determination of anisotropy and material hardening for aluminum sheet metal. *Int'l J. Solids Struct.* **49**, 3496-3506.

Tipper, C.F., (1949). The Fracture of Metals. *Metallurgica: The British J. of Metals* **39**, 133-137.

Tvergaard, V., Needleman, A., (1984). Analysis of the cup-cone fracture in a round tensile bar. *Acta Metall.* **32**, 157–169.

Tvergaard, V., (1990). Material failure by void growth to coalescence. *Adv. Appl. Mech.* **27**, 83-151.

US Environmental Protection Agency (2012). *Fed. Reg.* **77(199)**, 62624-63200.

Voce, E., (1948). The relationship between stress and strain for homogeneous deformation. *J. Inst. Met.* **74**, 537–562.

Vita

Martin Scales graduated from The University of Texas at Austin in December 2008 with a B.S. with Highest Honors in Civil Engineering. He subsequently entered the US Navy as an officer and served on active duty for three years, leaving the service with a rank of LTJG. Upon return to civilian life, he entered the Graduate School at The University of Texas at Austin to pursue a PhD in Engineering Mechanics. In the process, he presented at several national and international conferences, and coauthored the following publications:

Chen, K., Scales, M., Kyriakides, S., Corona, E. (2016). Effects of anisotropy on material hardening and burst in the bulge test. *Int'l J. Solids Struct.* **82**, 7-84.

Scales, M., Tardif, N., Kyriakides, S., (2016). Ductile failure of aluminum alloy tubes under combined torsion and tension. *Int. J. Solids Struct*. **97–98**, 116–128.

Chen, K., Scales, M., Kyriakides, S., (2018). Material hardening of a high ductility aluminum alloy from a bulge test. *Int'l J. Mech. Sci.* **138-139**, 476-488.

Chen, K., Kyriakides, S., Scales, M., (2018). Effect of material frame rotation on the hardening of an anisotropic material in simple shear tests. *ASME J. Applied Mech.* **85**, 124501; 1-5

Scales, M., Chen, K., Kyriakides, S., (2019). Anisotropy, Localization, and Failure in Aluminum Alloy Tubes: Part I Experiments. *Int'l J. Plast.* [in press]

Chen, K., Scales, M., Kyriakides, S., (2019). Anisotropy, Localization, and Failure in Aluminum Alloy Tubes: Part II Analysis. *Int'l J. Plast.* [in press]

Permanent email: mfscales@gmail.com

This dissertation was typed by the author.